Miniaturization and Integration of Optoelectronics for Contact Lens Embedded Display and Wireless Communication

Ramin Mirjalili

A dissertation

submitted in partial fulfillment of the

requirements for the degree of

Doctor of Philosophy

University of Washington

2013

Reading Committee:

Karl F. Böhringer, Chair

Babak Amirparviz

Brian P. Otis

Program Authorized to Offer Degree:

Electrical Engineering

University of Washington

Abstract

Miniaturization and Integration of Optoelectronics for Contact Lens Embedded Display and Wireless Communication

Ramin Mirjalili

Chair of the Supervisory Committee:

Professor Karl F. Bohringer

Department of Electrical Engineering

This dissertation presents the progress to miniaturize and integrate optics and optoelectronics for two applications. In the first segment, latest progress in wireless powering of several single pixel displays embedded in a contact lens platform would be demonstrated. Then in order to extend display capabilities, design and fabrication of micro LED-Fresnel Zone Plate display components will be described, which pave the way for constructing a contact lens display that is capable of producing in-focus images on the retina surface.

In the second segment, a vision for a universal identification system to include physical objects into the cyberspace will be introduced. The approach includes a wirelessly read-writeable tag that holds a unique ID while a cloud-based service manages the global assignment and storage of codes and object definitions. Fundamental scaling limitation of conventional identification tags is a major motivation to utilize an optical alternative to RF for power and data transmission. As an initial proof of concept, an end-to-end prototyping of the envisioned optical identification system comprising of hardware and software infrastructure design and development would be presented, followed by preliminary packaging process development applicable for encapsulating autonomous optical microsystems.

Acknowledgements

I would like to gratefully thank Dr. Böhringer and Dr. Parviz for their guidance, understanding, and support over the last four years. I would like to express my great gratitude to Dr. Otis for his support and his team at Wireless Sensing Lab. I want to thank my colleagues in the Bionanotechnology Lab for their input, great support and valuable discussion, particularly Dr. Andrew Lingley and Christian Marcheselli.

Finally and most importantly, I would like to thank my family, especially my wife, for their altruistic support and encouragement.

Table of Content

Acknowledgements ..... **iv**

Table of Content ..... **v**

List of Figures ..... **vii**

List of Tables ..... **xi**

Chapter 1 Introduction **2**

Chapter 2 Contact lens embedded display **4**

2.1 Wireless powered active contact lenses **7**

2.2 Contact Lens Fabrication Process Flow **9**

2.2.1 Template fabrication 10

2.2.2 Components Assembly 11

2.2.3 Molding and Packaging 13

2.2.4 Summary of wireless controlled contact lens display 13

2.3 Optical challenge for contact lens embedded display **14**

2.3.1 Evolution of diffractive lenses 15

2.3.1.1 Fresnel Lenses 15

2.3.1.2 Fresnel Zones and the Fresnel Zone Plate 16

2.3.1.3 Monofocal Diffractive Lenses 20

2.3.2 LED-FZP System, Experimental 28

2.3.2.1 Design 28

2.3.2.2 FZP fabrication: 30

2.3.2.3 Blue micro LED fabrication: 32

2.3.2.4 Template Fabrication and assembly 39

2.3.2.5 Testing and Results 39

2.3.3 LED-FZP Discussion and Summary 42

Chapter 3 Universal Basic Identification Tag **45**

3.1 Introduction **45**

3.2 Organic Light Emitting Diodes (OLED) **53**

3.2.1 Brief history 53

3.2.2 Basics 55

3.2.3 Standard Fabrication processes 57

3.2.4 Single layer Polymeric OLED process development 60

3.3 Prototyping UBITag system infrastructure **65**

3.4.1 Hardware 67

3.4.1.1 Tag 67

3.4.1.2 Reader 72

3.4.2 Software 79

3.4.2.1 Protocol 79

3.4.2.2 MCUs Firmware 79

3.4.2.3 Database development 82

3.4.2.4 Mobile Application development 84

3.4.3 Infrastructure Prototype, demonstration result 86

3.4 Encapsulation of miniature components **94**

3.4.1 Sphere Encapsulation 95

3.4.2 Reflective coating deposition 100

3.4.3 Release and Attachment 101

3.4.4 Reflection measurement 106

3.4.5 UBITag Summary 107

Chapter 4 Conclusions and Future Plans **109**

References **114**

Appendix A Tag and Reader MCU codes.....130
Appendix B Database inquiry PHP syntax.....136
Appendix C MSP430FR57xx blocks 138

List of Figures

Figure 2.1 Conceptual drawing of a multi-pixel contact lens display. A contact lens display comprising a multi-pixel light emitting diode chip, power- harvesting/control circuitry, an antenna, and interconnects. These subsystems are encapsulated in a transparent polymer, creating a system to project virtual images perceivable by the eye of the wearer.....6
Figure 2.2 a) Contact lens with red LED assembled and molded. b) The LED can be seen lit in the center of the contact lens, powered with a dipole antenna. 8
Figure 2.3 Wireless activation of a contact lens display on a live rabbit. a) Photograph of a completed contact lens system. b) The contact lens display was placed on the eye of a live rabbit and powered by a dipole antenna, resulting in bright blue emission from the on-lens pixel. The micro-LED indicator was activated periodically and remained *in vivo* for up to 40 minutes. 9
Figure 2.4 a) Optical microscope image of predetermined text, "AALTO UNIVERSITY, UNIVERSITY OF WASHINGTON", fabricated on LED by shaping the electrode pattern, b) Optical microscope image of the LED emitting the predetermined pattern upon application of a bias current, c) the LED chip assembled on contact lens with radio and antenna, and turned on wirelessly 9
Figure 2.5 Process flow of the lens fabrication[11]: a) Start with blank PET wafer, b) Evaporate, lift-off Cr/Ni/Au, c) Spin-on and pattern electrical insulating SU-8 2, d) Electroplate 5 um Au antenna, e) Spin-on and pattern thick SU-8 25 for LED well (center) and chip well (upper left), f) Cut out contacts 11
Figure 2.6 Solder coating process[15]. Boiling water in the outer beaker maintained the solder and overlying ethylene glycol at ~95 °C. a) Solid solder in a 100 mL beaker, placed in a second beaker filled with water. b) Partially melted solder. c) Fully melted solder. d) After removing dirty ethylene glycol. e) After adding 10 mL of fresh ethylene glycol and 60 μL HCl. f) Templates were coated with solder by pipetting molten solder across a template. Here, three out of four large Au pads were coated for easy visibility. 12
Figure 2.7 a) A large lighthouse lens. b) The underlying concept of a Fresnel Lens: The original bulk of the dashed lens is reduced, leaving a thin lens whose surface slope matches the original lens. This example has equal step heights. c) A Fresnel lens with equal zone width. Depicted from [28] 16
Figure 2.8 Front and cross section view of a Zone Plate. The radius for the innermost zone r_1 and outermost radius r_N and zone width dr_n for the n'th zone are shown. 17
Figure 2.9 A diagram indicating the optical path length between the source point *S* and image point *P* via a zone boundary pair at radii r_n and r_{n+2} 18
Figure 2.10 Focusing with a Zone Plate into the first three odd diffraction orders. The focal length for the first order is denoted *f*. Negative diffraction orders originating from virtual foci behind the Zone Plate are also indicated. In the figure, ray paths from the negative orders are only drawn for the outermost part of the Zone Plate for clarity[35].....19
Figure 2.11 Diffractive lens construction: (a) conventional refractive lens, (b) diffractive lens with continuous quadratic blaze profile, (c) phase-reversal (or Wood) lens, (d) four-level approximation to quadratic blaze profile[40]. 21
Figure 2.12 Diffraction efficiency of binary approximation of kinoform lens (continuous blaze profile) [41].....22
Figure 2.13 a) A conventional diffractive lens is highly dispersive and focuses different wavelengths of light to different focal positions, b) A MOD lens brings multiple

wavelengths across the visible spectrum to a common focal point and is thereby capable of forming high-quality images in white light[42]. 23
Figure 2.14 Cross section of a multi-order diffractive (MOD) lens. The phase jump at the edge of the various zones is 2πp, where p is an integer. The zone radii, r_n, are obtained by solving the equation $\Phi(r_n) = 2\pi pn$, where $\Phi(r)$ represents the desired phase function for the lens[43]. 24
Figure 2.15 Diffraction efficiency of the *m*th diffracted order versus wavelength for a MOD lens[40] with $p = 10$. 27
Figure 2.16 a) An FZP implemented as obscurations in ZEMAX; the scale bar is 20 μm. b) Physical Optic Propagation analysis of FZP: 60 μm waist Gaussian beam, illuminated through the designed FZP focuses at the desired 275 μm; the scale bar is 10 μm 29
Figure 2.17 Simulated light intensity maps. a) LED structure modeled in non-sequential ZEMAX with integrated Binary2 surface as FZP gives a focused spot caused by subsidiary f/3 focal point at 250 μm distance from the surface, b) while the LED without integrated Binary2 surface does not have the focusing behavior. The scale bar is 100 μm. 30
Figure 2.18 Different doses can overexpose larger features (innermost rings) and underexpose smaller features (outermost rings). Lift-off result of different exposure doses in uC/cm^2: a) 500, b) 475, c) 425, d) 325, e) 275, f) 150. 32
Figure 2.19 LED and FZP fabrication process, a) Sapphire substrate with epitaxially grown layers of p-GaN/InGaN MQW/n-GaN/GaN buffer, b) Ni deposition as etch mask, c) Chlorine-based ICP RIE etching of top layer (p-GaN/ InGaN MQW) to reach the n-GaN region, then removing the Ni mask, d) p-contact metallization Ni/Ag/Au, e) n-contact and cross shape mark for backside alignment deposition, f) sapphire side lapped and polished down to ~270 mm, g) Aligned to front side cross marks, L-shape alignment marks deposited using Cr, h) FZP opaque rings deposited after Electron Beam Lithography. 37
Figure 2.20 SEM image of a 275um foci Fresnel Zone Plate 38
Figure 2.21 Severe chipping of sapphire resulted from saw dicing due to crystal orientation. 39
Figure 2.22 Far field image of a custom pattern white source diffracted at designated focal distance of an FZP with 325um foci for 475nm (blue) at different distances of its surface image created by f/3 subsidiary focii a)84um and b)103um. Images created by main power of lens at c) 236um, d) 261um, e) 282um, f) 300um, g) 325um, h) 345um. 40
Figure 2.23 a) Optical microscope images of the rectangular test LED chip with pre-determined illumination pattern. The scale bar is 200 μm. b) FZP creates an upside-down image of the LED chip (which is ~5mm away from the FZP) approximately at the focal point. The FZP is visible as shadowed blue circle and the LED chip image is recognizable as the rectangle with a bright illuminated pattern (we flipped the image to make the object and image comparison more convenient). The scale bar is 50 μm. 41
Figure 2.24 Testing of 2 different LEDs with an integrated FZP under an optical microscope: a) 50 μm wide LED pixel #1. b) Real image of LED pixel #2, focused at 230 μm from FZP surface in front of system, created by f/3 subsidiary focal point. c) Upright ghost image of LED pixel #1 created in the back plane of system. d) Ghost image of LED pixel #2 in the back plane of the system. Scale bars are 50 μm. 42
Figure 3.1 UBITag infrastructure: A miniature generic tag attached to a physical object loaded with information such as ID, assigned and readout by a custom Reader, controlled through a use interface on a conventional mobile device. Information about the ID is stored in the cloud. 46
Figure 3.2 The antenna and radian sphere view of an electrically small antenna [60] 47

Figure 3.3 Comparison of classical fundamental limits for Q_a [60] 48
Figure 3.4 Envisioned monolithic UBITag can be fabricated through CMOS and OLED processes[94] 52
Figure 3.5 Progress in various lighting and display source efficiencies over the past few decades. Copyright K. Leo/IAPP. 54
Figure 3.6 Comparison of the luminance efficiencies of several different lighting and display sources. Figure courtesy of C.W. Tang, Kodak, Inc[115]. 55
Figure 3.7 a) An OLED is a special amorphous material sandwiched between two electrodes, b) Band diagram under forward bias illustrating the charge injection, transport, and recombination processes. LUMO and HOMO are analogous to conduction and valence bands of semiconductors. 55
Figure 3.8 a) Energy level diagram of a two-layer OLED. b) Common electron and hole-transport materials and a two-layer OLED [117]. 59
Figure 3.9 An sample energy level / work function diagram for a PLED[116]. The HOMO/LUMO levels for the polymer shown are that of MEH-PPV[125-126]. In this example, no barrier exists for electron injection. 60
Figure 3.10 a) Silicon wafer with pre-grown oxide, b) Al/Mg layer deposited and patterned through lift-off, c) MEH-PPV solution spun and vacuum dried, d) Anode layer deposited through shadow mask. 62
Figure 3.11 IV characteristic of OLED with different anodes: series1) ITO only, series2) 7nm Au only, series3) Evaprated 7nm Au/ Sputtered ITO, series4) Au/ITO sputtered 63
Figure 3.12 Optical Spectrum of MEH-PPV OLED with peak at 580nm. 64
Figure 3.13 a) Fabricated OLED tested with probestation, b) Sample illuminating OLED. 64
Figure 3.14 Block diagram of tag 68
Figure 3.15 Optical data detection circuit schematic with and without logic inversion 68
Figure 3.16 Schematic of tag prototype circuit 71
Figure 3.17 Tag, prototyped PCB board 72
Figure 3.18 Reader block diagram 73
Figure 3.19 a) Spectral sensitivity of harvesting PIN diodes (SFH2701), b) Spectral sensitivity of detecting PIN diodes (TEMD7100) 74
Figure 3.20 Reader optical data detector and driver 76
Figure 3.21 a) Reader PCB design, b) Manufactured board with SMT components 78
Figure 3.22 Reader, packaged in a 3D printed box, with a cap to access optical head 79
Figure 3.23 Tag MCU flow chart 80
Figure 3.24 Reader MCU flow charts 81
Figure 3.25 Message in case of redundant ID selection 83
Figure 3.26 New ID/Information assignment form 83
Figure 3.27 Confirmation message after each database update 83
Figure 3.28 No-entry matched message for ID 84
Figure 3.29 TagID and TagInfo looked up from database 84
Figure 3.30 Android UBITag Application interface. 86
Figure 3.31 Connecting to Reader's Bluetooth 89
Figure 3.32 Error message to redundant entry. 89
Figure 3.33 Entering a non-redundant ID. 90
Figure 3.34 Checking database for redundancy 90
Figure 3.35 PHP form appears on the webview segment. 91
Figure 3.36 Entering tag's description: "Test". 91
Figure 3.37 Update message is displayed once ID and Info are submitted to database. 92
Figure 3.38 New ID assigned optically to Tag, controlled through the app. 92
Figure 3.39 Tag ID can be readout optically, controlled through the app. 93

Figure 3.40 Read-out ID is sent from the Reader, and respective information is looked up and displayed through the app. 93
Figure 3.41 Envisioned packaging: spherical shape with partial reflective coating, which helps to create an optical path between tag chip and Reader....95
Figure 3.42 Saw-diced silicon dummy chips, 950um square, used for packaging development 95
Figure 3.43 Two matching mold halves with hemispheric cavities to create miniature-size spheres....96
Figure 3.44 a) Cavities of various radii were machine milled on b) two-piece and c) matching mold. 97
Figure 3.45 a) One of the mold halves is partially filled with epoxy then cured to create cushioning for Si chips. b) Second layer of fresh epoxy on the first cured one helps to prevent air bubbles trapped under Si chips. c) Protective mesh covers mold's surface and vacuum-gripped chips would align on top of cavities. d) Chips would release by breaking vacuum of gripper. For our experiments chips were manually dropped in cavities. e) Second mold half with fresh epoxy casted on would match and seal the bottom half. f) Resin would solidify through thermal curing at 65º C. 98
Figure 3.46 Protective mesh covers flat surface of mold half. a) Off the mold, b) On the mold 99
Figure 3.47 a) Chips encapsulated in larger spheres (2.4mm, 2mm diamter) have more deviation from center, b) a less frequent problem for smaller spheres (1.8mm diameter) 100
Figure 3.48 a) Mirror layer deposited on epoxy spheres while they are secured on mold, b) sample result of on-mold mirror deposition....101
Figure 3.49 Epoxy drops of 1.75mm diameter, with mirror layers on them, released from the mold 102
Figure 3.50 A minimum obtuseness, *a*, is required in order to create an optical link to the chip inside. Thus the probability would be *(180-2a)/360*, which would be 44% for *a*=10º..103
Figure 3.51 Multiple sphere attachment using a clear adhesive drop containing multiple spheres. This process eventually can be accomplished through a procedure analogous to conventional printing. 104
Figure 3.52 a) After depositing mirror layers, b) an extra molding step to make the packaging shape aspheric and two sided; c, d) release of modified packaging. e) Sample attachment of a single modified packaging through the sequence illustrated in Figure 51 105
Figure 3.53 Modified packaging attaching method resulted in 96% successful result of single package with clear side facing up. This eliminates the need for multiple packagings for a single object, which linearly reduces the final cost per object. 106
Figure 3.54 Reflection was calculated as the ratio of the absolute irradiance reflected from the mirror stack to the total irradiance of the He-Ne laser....107

List of Tables

Table 3.1 Characteristics of various energy sources available in the ambient and harvested power [54].....47

Chapter 1 Introduction

One of the major trends in industry is to miniaturize systems and improve their capabilities. A good example of such a trend is the size shrink of semiconductor integrated circuits that happens every few years, popularly known as Moore's law. But no complex system is solely comprised of compact circuits. There usually are various forms of sensors, transducers, and non-electronic components utilized in the system that need to be miniaturized as well, to achieve the certain goal of a compact system. Optical and optoelectronic devices are of great importance for telecommunications and sensing applications. Components such as Light Emitting Diodes, Photodiodes and Micro-lenses are among the important subsystems juxtaposed to microelectronic circuitry in today's multifunctional products.

Through this manuscript, we will describe our effort toward miniaturization and integration of optoelectronic components for two major applications: contact lens embedded display (Chapter 2) and wireless communication (Chapter 3).

Chapter 2 begins with an overview of work toward creating wirelessly controlled contact lenses embedding a single element display. Then the rest of the chapter covers our effort toward overcoming the optical challenge of contact lens display, which entails creating an in-focus image of the display on the retina. A detailed description of design, fabrication and testing of GaN LED structures integrated with diffractive elements, Fresnel Zone Plates, is the main focus of Chapter 2.

In Chapter 3, we envision utilizing optical paths for power and data transmission to establish a universal identification system based on a miniature tag. The feasibility fabricating a monolithic tag in miniature sizes with available technologies and the basic infrastructure of such a system are covered at the beginning. Then our effort toward prototyping the infrastructure comprising development of proper hardware and software layers is fully

described. In the last section, a novel cost effective packaging process, compatible for encapsulating miniature autonomous optical systems, is developed and presented thoroughly. Finally, in Chapter 4, after a brief review of the accomplishments, future plans to improve the results of each segment are presented.

Chapter 2 Contact lens embedded display

Arguably one of the most important ways of receiving information for us is through vision. The light reflecting or refracting off of various physical objects is collected by the eyes and transmitted to various parts of the brain for specific processing. The first bodily object light encounters is the cornea, an essentially clear layer of cells that is to first approximation spherical in shape, and which provides about two-thirds of the refractive power of the eye. Light then passes through the aqueous humor and the pupil and is refracted dynamically by the crystalline lens. Finally, light passes through the vitreous humor and the bulk of the retina where it is absorbed by photoreceptors and undergoes transduction into an electrical signal. Amplification is performed by about 1.2×10^8 rods and 5×10^6 cones, and the resulting signal is sent to ganglion cells. Then this information passes through the million or so fibers of the optic nerve, into the brainstem, and on to the visual cortex. The human visual system operates over a wide range of light intensity (~12 orders of magnitude) and allows for color vision, judgment of distance and movement, and high-resolution tasks[1,2].

Unfortunately, despite the complexity and adaptability of the visual system, some people cannot see clearly. Often this results from a misshapen cornea that projects a focused image behind or in front of the retina. Thus eyeglasses were invented and were the sole means of vision correction for centuries until the realization of contact lenses, which were initially blown glass structures fitted over the cornea and part of the sclera. Corneal lenses were patented in 1950, and the first soft contact lenses (made from poly- HEMA) were demonstrated in 1961. Rigid gas permeable lenses with high oxygen permeability were invented next, followed by silicone hydrogel soft lenses that are now ubiquitous[3]. Contact lenses are used by tens of millions worldwide in a market estimated at $6.1 billion in 2010 [4].

Although primarily used for vision correction (and occasionally for aesthetics), their location on the corneal surface presents unique opportunities for vision augmentation or biological monitoring[5]. For example, see-through displays could overlay computer-generated visual information on the real world, providing immediate, hands-free access to information[6].

Wearable computing and augmented reality will likely provide new ways to manage information and interact with the world. The first step towards always-accessible, superimposed information will most likely be implemented in see-through eyeglass displays, such as those presented by Google's Project Glass or Fraunhofer IPMS head mounted display[7]. However, a much less cumbersome display for augmented reality may take the form of a contact lens. Like their larger counterparts, contact lens displays could communicate with Internet enabled devices to retrieve discrete and real-time emails, text messages, reminders, or navigational information. Pioneering contact lens display development has been accomplished by the Parviz Group at the University of Washington, with the long-term goal of developing systems with pixel arrays, focusing optics, and antennas, as well as circuitry for power harvesting, radio communication, and pixel control (Figure 2.1).

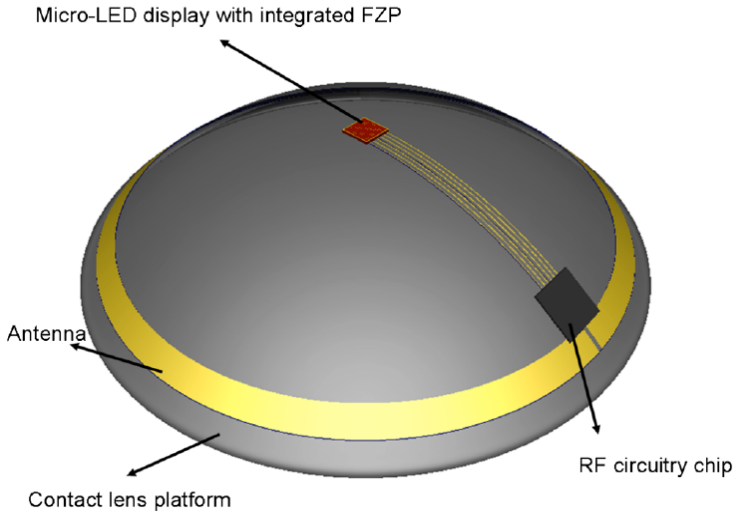

Figure 2.1 Conceptual drawing of a multi-pixel contact lens display. A contact lens display comprising a multi-pixel light emitting diode chip, power- harvesting/control circuitry, an antenna, and interconnects. These subsystems are encapsulated in a transparent polymer, creating a system to project virtual images perceivable by the eye of the wearer.

Integrating displays on contact lenses presents several challenges, which our group has been working on for some time. First, as the display is standalone, power must be provided and stored for system operation without a wired connection. Environmental photovoltaic generation from the sun or fluorescent lighting may be appropriate for sensing, where power requirements are very low. In the other hand, radio frequency power can be a suitable option to provide sufficient energy for wireless operation of the display. Second, the contact lens system must be biocompatible and meet regulations for radiofrequency (RF) radiation. For example, LEDs made of toxic materials (inorganic crystalline or organic amorphous) must be enveloped in a biocompatible substance for safe operation. Additionally, safety standards place limits on incident radio frequency radiation. Therefore, the energy efficiency of the electrical and optical subcomponents is of the utmost importance. In order to minimize losses, inorganic single-crystalline components (for display LED) and metal structures (interconnects and antenna) are the best candidates. Utilizing organic materials for display

LED, despite their acceptable efficiency, is more challenging because they are more difficult to integrate and are sensitive to oxygen and moisture. The third challenge is the mechanical and electrical integration of heterogeneous micrometer-scale components (e.g. silicon integrated circuitry and III–V semiconductor optoelectronics) on a polymer substrate. Furthermore, all components must fit within the volume of standard contact lenses, ~1.0 cm^2 in area with thicknesses of 200 μm or smaller[2]. Additionally, the human eye, with its nearest focus point (closest point of accommodation) ranging from 7 to 40 cm for teenagers to middle-aged adults[8], cannot resolve objects on a contact lens display. This raises the optical challenge of creating an in-focus image of displayed pixels on the eye.

An overview of our work to make wirelessly controlled contact lens displays with an unfocused single element is given below; detailed description of our effort to overcome the optical challenge through co-integration of micro-optics and the display element comes as the last part of this chapter.

2.1 Wireless powered active contact lenses

First, Ho et al. devised a fabrication process to deposit two metal layers and polymer insulation on a clear polymer substrate, upon which an array of micrometer scale LEDs was assembled. However, the LEDs failed when molding the device for corneal fitting[9]. Next, Pandey et al. used a similar fabrication process to create single pixel LED displays on planar polymer discs comprising custom integrated circuits (ICs), antennas, and LEDs. The on-lens antenna collected radiation from an external transmitter, and the power-harvesting IC rectified and stored energy to duty-cycle an LED at a frequency sufficiently high as to give the appearance of continual light emission[10]. The following year, the lenses were improved by electrolessly plating the custom ICs for flip-chip style assembly, and the polymer substrate fabrication process was modified to reduce antenna resistance and improve system

performance[11] (Figure 2.2). Using flip-chip style assembly, an operational molded structure was realized. Building from these efforts, systems comprising single blue LEDs, antennas, and ICs were tested *in vivo* on rabbits reported by Lingley *et al.*[12] (Figure 2.3). In the most recent effort, the author successfully assembled a single element LED with pre- determined text on the contact lens platform, wirelessly controlled utilizing RF system[13] (Figure 2.4).

To our knowledge, the only other attempt at developing a contact lens display was by De Smet[14]. A contact lens display based on liquid crystal modulation of light was theorized, as well as additional uses such as tunable sunglasses or artificial irises. Voltage controlled liquid crystals were embedded between two polymer sheets separated by photolithographically defined spacers. After spherical molding, an applied voltage caused the transparent crystals to rotate and become opaque.

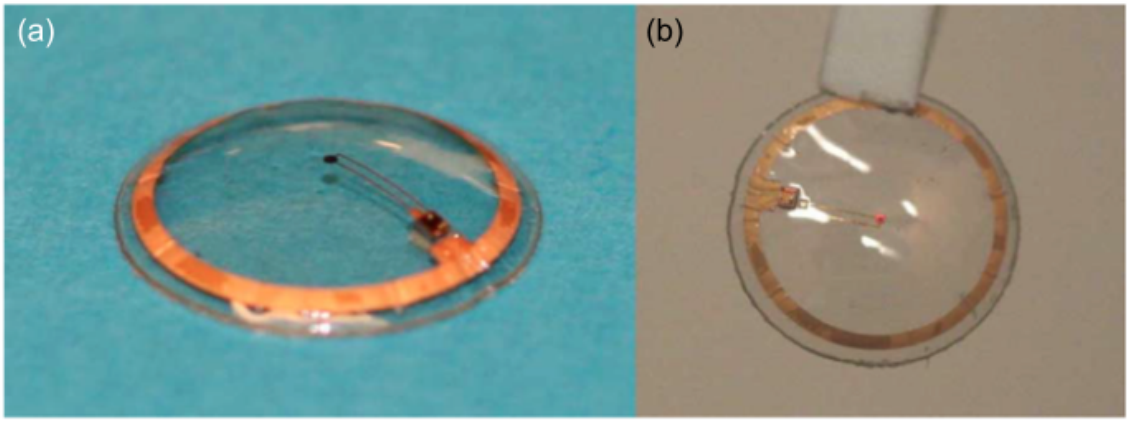

Figure 2.2 a) Contact lens with red LED assembled and molded. b) The LED can be seen lit in the center of the contact lens, powered with a dipole antenna.

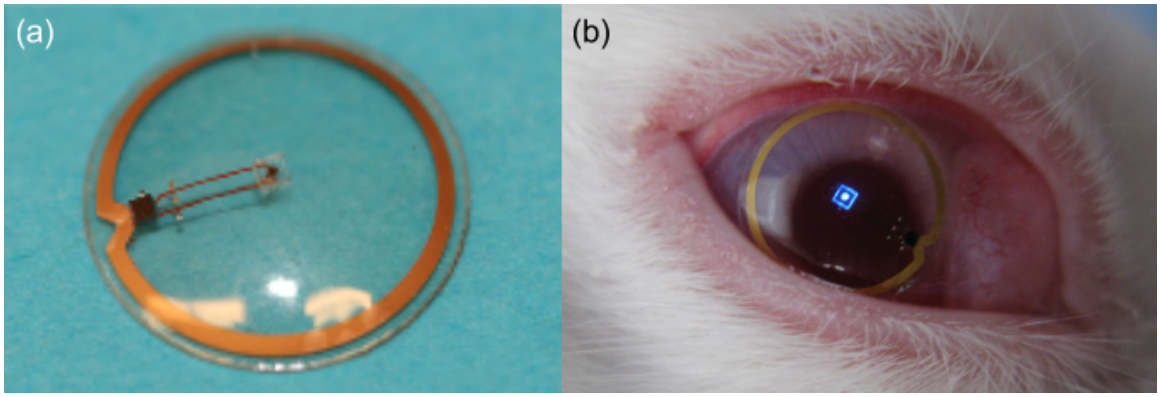

Figure 2.3 Wireless activation of a contact lens display on a live rabbit. a) Photograph of a completed contact lens system. b) The contact lens display was placed on the eye of a live rabbit and powered by a dipole antenna, resulting in bright blue emission from the on-lens pixel. The micro-LED indicator was activated periodically and remained *in vivo* for up to 40 minutes.

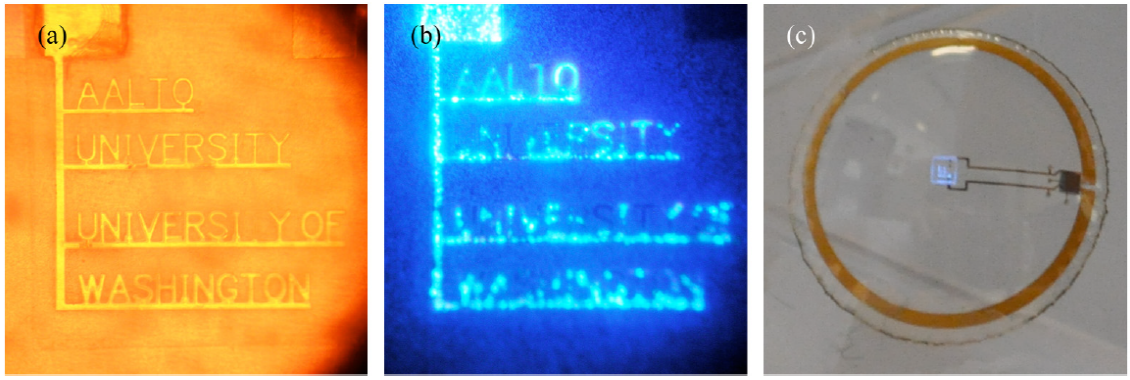

Figure 2.4 a) Optical microscope image of predetermined text, "AALTO UNIVERSITY, UNIVERSITY OF WASHINGTON", fabricated on LED by shaping the electrode pattern, b) Optical microscope image of the LED emitting the predetermined pattern upon application of a bias current, c) the LED chip assembled on contact lens with radio and antenna, and turned on wirelessly

2.2 Contact Lens Fabrication Process Flow

The major steps in reported active contact lenses[11,12,13] are as follows : 1) microfabrication of substrates with antennas, electrical interconnects, sensor electrodes, and component receptor sites, 2) assembly of circuits and optical components, 3) and substrate molding.

2.2.1 Template fabrication

Template fabrication process is as follows (Figure 2.5):

The antenna, electrical interconnects, electrical isolation, and pads for solder coating were fabricated directly on the contact lens. Polyethylene terephthalate (PET) was chosen as a substrate because of good chemical resistance, thermal stability during photolithography, and transparency. First, 100 mm wafers with major and minor flats were cut from 25.4 cm × 25.4 cm × 100 um sheets of polyethylene terephthalate (POLICROM, Inc.) using a CO2 laser cutter. The wafers were cleaned with sonication in acetone, isopropyl alcohol (IPA), deionized water and then spin-rinse-dried. Next, AZ4620 (MicroChem Corp.) was spun and soft baked. Ultraviolet exposure was done in an ABM contact aligner. Development was carried out in AZ400K (MicroChem Corp.). The wafers were plasma cleaned in a Branson barrel etcher and immediately placed in an electron beam evaporator. A layer of Cr/Ni/Au (20, 80, 350 nm) was evaporated at 5 $\times 10^{-6}$ Torr. Acetone and sonication for ~30 s facilitated metal lift-off. After lift-off, the wafers were rinsed in IPA, deionized water and put through a spin-rinse-dry. Next, a ~2 um layer of SU-8 2 was spun, baked, exposed and developed in SU-8 developer with agitation. Again, the wafers were rinsed in IPA, and sent through the spin–rinse–dry. Next, a 40 nm seed layer of Au was deposited using electron beam evaporation, and AZ4620 was patterned using the aforementioned method. Pulsed electroplating (1 ms on, 1 ms off) was used to plate ~5 um of Au using a cyanidebased Pur-A-Gold 401 formulation (Enthone-OMI Inc.). This electroplating step is necessary in order to produce more efficient antennas with thicker metal than is normally achievable with e-beam evaporation or sputtering. The photoresist was removed in acetone, and the seed layer was etched in 5:1 (vol:vol) deionized H2O:Gold Etch TFA (Transene Company, Inc.). SU-8 25 was spun, exposed and developed. Blue dicing tape was placed on the back of the wafers, and

individual contact lenses were cut out with a CO2 laser. Aluminum oxide sand paper (5 *um* grit) were used to polish the contact lens edges after laser cutting.

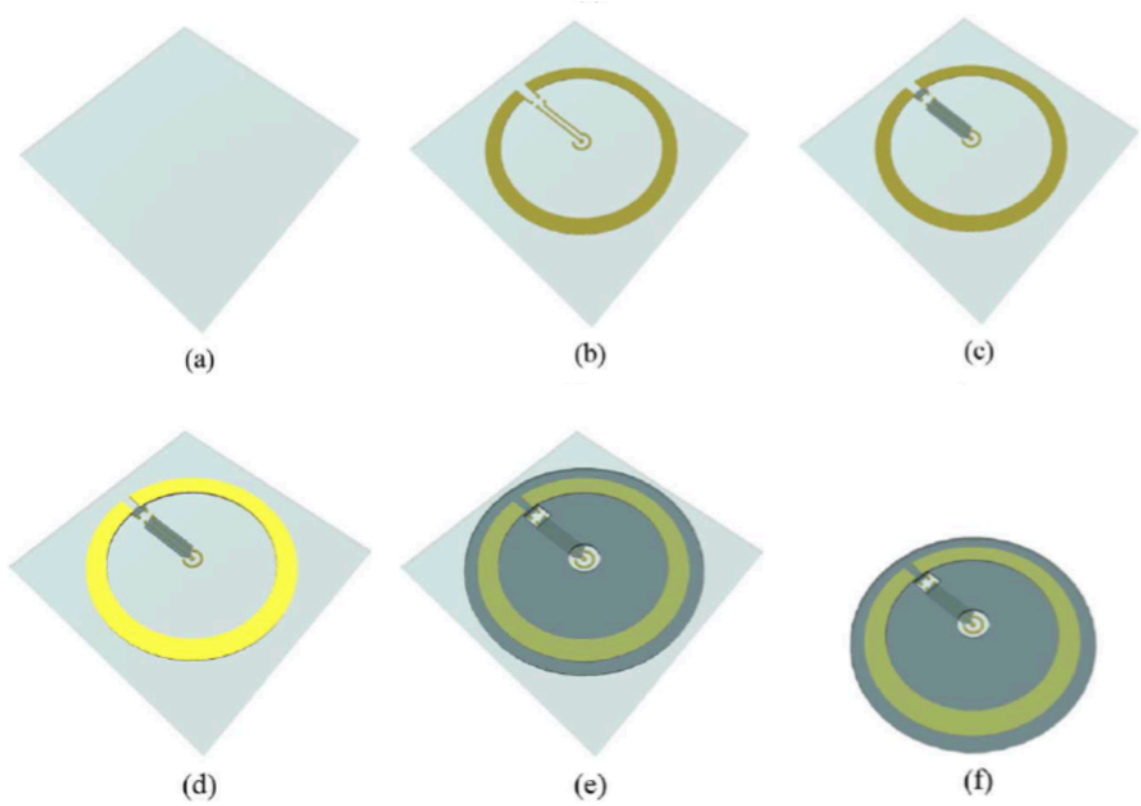

Figure 2.5 Process flow of the lens fabrication[11]: a) Start with blank PET wafer, b) Evaporate, lift-off Cr/Ni/Au, c) Spin-on and pattern electrical insulating SU-8 2, d) Electroplate 5 um Au antenna, e) Spin-on and pattern thick SU-8 25 for LED well (center) and chip well (upper left), f) Cut out contacts

2.2.2 Components Assembly

LED and CMOS circuit were connected to the lens in a manner similar to that presented in [11]. Prior to solder coating, the custom silicon IC aluminum pads (from MOSIS) were electrolessly plated with Ni and Au (CV Inc.). Leadfree, 60 ◦C eutectic solder (Indium Corp., Indalloy 19) was used to coat the exposed pads on the template, microchips, and micro-LEDs. The solder was melted in a 100 mL beaker while immersed in ethylene glycol (EG). Next, 60 *u*L of HCl was added to the ethylene glycol to clean the solder surface. While the solder was heating, a solution of 25 mL of EG and 10 *u*L of HCl was prepared in a petri dish.

Prior to coating, the EG used during heating was removed from the solder by pipette, and 10 mL of fresh EG was added along with 60 *u*L of HCl. Next, the IC, micro-LED chip and template were coated with solder using a pipette (Figure 2.6), and then placed in the prepared petri dish. The silicon microchip and micro-LED chip were placed on the contact lens in corresponding SU-8 25 wells using a microscope for observation. The petri dish was heated to melt the solder, at which time the components self-aligned and connected to the contact lens interconnects and antenna. The petri dish was removed from the hot plate approximately 30 s after chip alignment. After cooling for 5 min, the contact lenses were soaked in IPA for 20 min, then rinsed in IPA and dried with nitrogen.

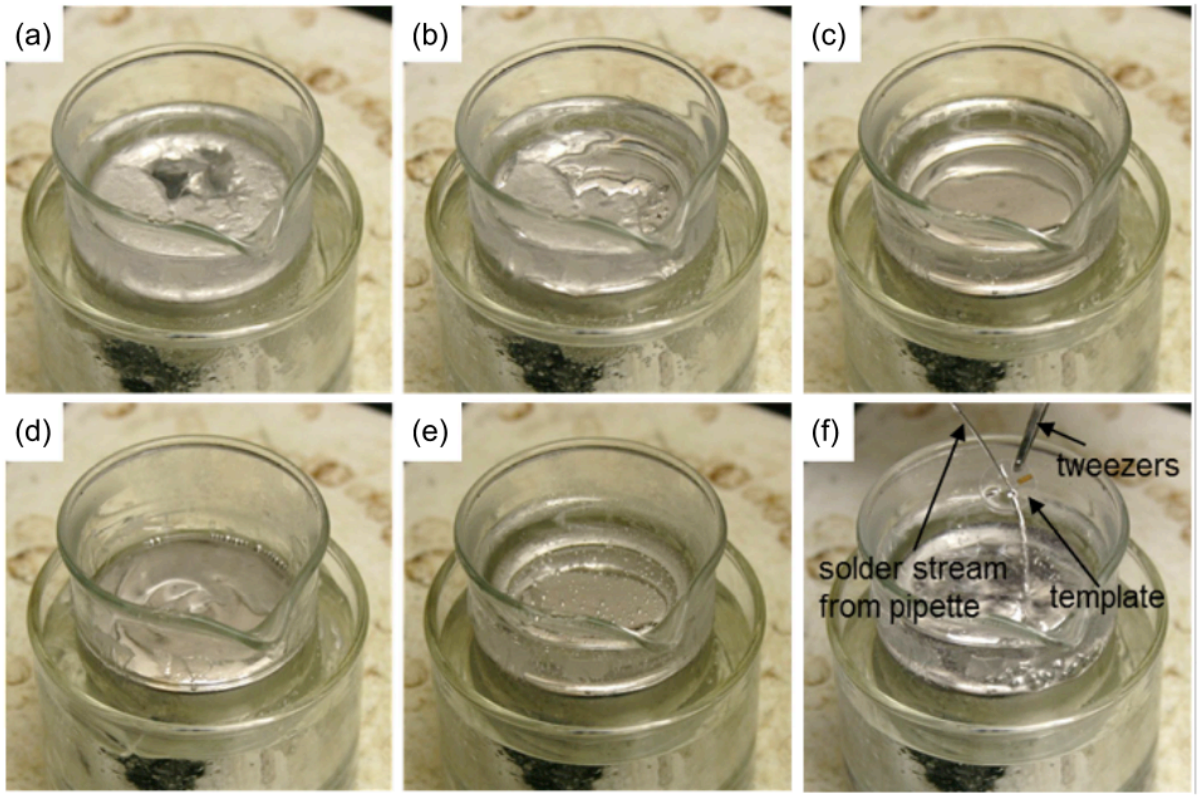

Figure 2.6 Solder coating process[15]. Boiling water in the outer beaker maintained the solder and overlying ethylene glycol at ~95 °C. a) Solid solder in a 100 mL beaker, placed in a second beaker filled with water. b) Partially melted solder. c) Fully melted solder. d) After removing dirty ethylene glycol. e) After adding 10 mL of fresh ethylene glycol and 60 µL HCl. f) Templates were coated with solder by pipetting molten solder across a template. Here, three out of four large Au pads were coated for easy visibility.

2.2.3 Molding and Packaging

A hemispherical aluminum mold (radius = 7.1 mm) was used to obtain the desired lens curvature. The mold contained a small hole drilled through the center and exiting the side, which was connected to a vacuum line. We heated the mold and a metal ring on hotplate set to 200 ◦C. The vacuum was pulled, and the contact lens was centered on the mold. We then placed the mold on an insulating surface, and the ring, having an inner diameter slightly less than the contact lens, was used to slowly press and shape the lens without disturbing the components. After cooling, the contact lens was removed from the mold, cleaned with IPA, and dried with nitrogen. Lastly, we deposited a layer of parylene-C (~10 *u*m, Specialty Coating Systems, PDS 2010 Labcoater 2) conformally over the contact lens for the purposes of biocompatibility and mechanical strength. The contacts lenses were sterilized in ethanol for 10 min and stored in a saline solution prior to testing on animals.

2.2.4 Summary of wireless controlled contact lens display

Such a single pixel or predetermined text system may be deployed for communicating immediate events to the user; however, it is of limited use for conveying more information. The custom designed wireless system (known as iChip1) could deliver 12 μW of power to the display, harvested from a 0 dBm (1 mW) Radio Frequency (RF) broadcast source, and used 3% modulation for power management[11]. In a single blue pixel display demonstration, the nominal visibility point for the InGaN LED (60 μA of current at 2.6V for a 260μm wide pixel[12]) translated to approximately 2.94 nW/μm^2. This in turn means the system as deployed could support up to nearly 50 pixels made of 50 μm wide LEDs (the sample size we used for experimentation).

2.3 Optical challenge for contact lens embedded display

Previously noted, one major challenge of constructing a display wearable in the form of a contact lens with multiple pixels is producing in-focus images from components that are placed directly on the cornea. As the closest accommodation point of the human eye ranges from 7 to 40 cm for teenagers to middle-aged adults[8], the output light of micro LED pixels on the contact lens will not be in focus on the retina. Therefore, optical components are needed to aid the eye in bringing the image into focus. One approach is to use a micro-lens in front of each group of LED pixels. The simplest way to collimate the output light of a source is to position the source at the focal point of a lens, which would theoretically create a ghost image of the displayed pixel behind the system. Integration of micro-lenses on micro LEDs to enhance the extraction of LED optical output has been previously reported [16-18]. The micro-lenses reported were either based on fabrication by reflow of transparent photoresist patterns acting as the lens or followed by an extra etch step to transfer the lenticular shape to the substrate[19,20]. Another approach to enhance the output extraction of LED is to integrate colloidal microspheres through self-assembly[21-23] or imprint lithography [24-26]. There are few issues regarding refractive micro-lenses for contact lens display application. Based on patterns resulted from photoresist reflow, micro-lenses fabricated in this manner do not give sufficient variation of focal distance, nor can their focusing and other optical properties be easily controlled. Additionally, these approaches would not work when the lens is embedded in a material with a similar (or very close) index of refraction, which in the case of the contact lens is the tear film covering the cornea. To minimize these effects and have a better control on focal distance, diffractive-based micro-lenses can be utilized.

2.3.1 Evolution of diffractive lenses

Let us first review a brief history of how refractive and diffractive lenses relate to each other, then study their basic performance and see how they can be utilized for multicolor display embedded in a contact lens platform.

2.3.1.1 Fresnel Lenses

A Fresnel lens is an optical component that can be used as a cost-effective, lightweight alternative to conventional continuous surface optics[33]. They can be traced back to the work of Augustin Fresnel, who improved lighthouse optics in the 1820s by segmenting large lenses to reduce their overall weight[34] (Figure 2.7a). Given that the refractive power of a lens is contained only at the optical interfaces (i.e. the lens surfaces), as much of the optical material as possible is removed while the surface curvature is still maintained. Another way to consider it is that the continuous surface of the lens is "collapsed" onto a plane[27].

There are no specific limitations on where zone boundaries need to be placed in a Fresnel lens, so boundary locations can vary with each application. One choice is to make the step heights constant, which requires that the zone widths vary (Figure 2.7b). Another choice is to give the zones a constant width, which requires that the step heights vary[28] (Figure7c).

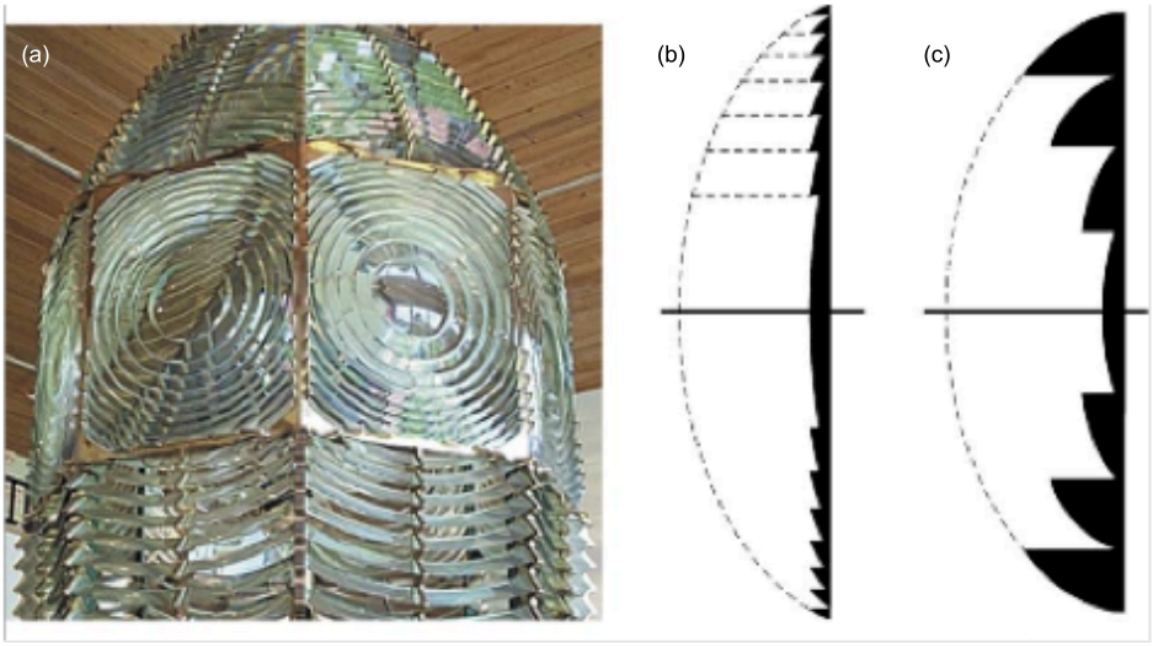

Figure 2.7 a) A large lighthouse lens. b) The underlying concept of a Fresnel Lens: The original bulk of the dashed lens is reduced, leaving a thin lens whose surface slope matches the original lens. This example has equal step heights. c) A Fresnel lens with equal zone width. Depicted from [28]

2.3.1.2 Fresnel Zones and the Fresnel Zone Plate

Before creating the lighthouse lens, Fresnel had contributed to the concept of diffraction at a time when there were questions about whether light consisted of particles or waves[29]. Huygens's construction, in which each point on a wavefront was taken to be the source of a new wavelet, was already well known at the time[29]. Fresnel's conceptual innovation in 1818 was to incorporate the ideas of amplitude, phase, and interference into the wavelet model of light propagation. This provided the potential for phase manipulations to have a significant effect on final wavefront characteristics. Working back from a distant point, the plane wavefront can be divided into zones by placing a zone boundary wherever the optical path increases by half a wavelength. If there is no diffracting obstacle, the light continues to propagate as a plane wave, but the theory indicates that if the central zone is obscured by an opaque object, a bright spot should appear in the shadow. This was found experimentally and called Arago's spot[30]; it has helped confirm the significance of Fresnel zones.

Fresnel's recognition of the importance of wavelength increments of the optical path distance

between 2 points is the fundamental basis for a diffractive lens, but the first focusing structure, the diffractive Zone Plate, was not described until 50 years later, in the 1870s. At that time, Lord Rayleigh observed that alternate half-period zones could be blocked to remove contributions from the second half of the wavelength cycle at the focus, and this led to the Fresnel Zone Plate structure depicted in (Figure 2.8)[30,31]

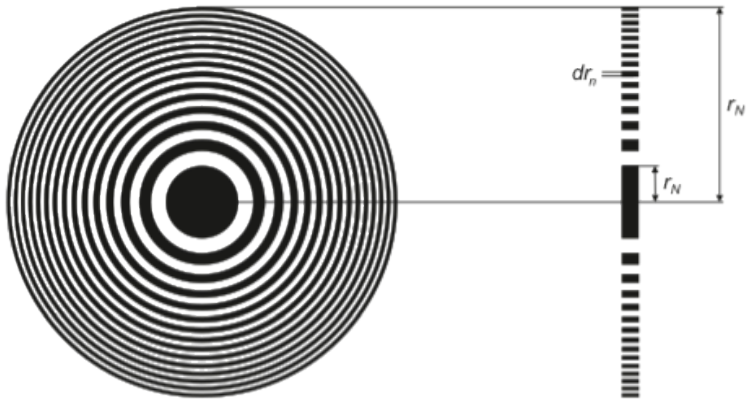

Figure 2.8 Front and cross section view of a Zone Plate. The radius for the innermost zone r_1 and outermost radius r_N and zone width dr_n for the n'th zone are shown.

Consider a wave immerging from point source *S* with wavelength λ. By interacting the wavefront with Zone Plate at a radius *r*, each point can be considered a Huygens-Fresnel secondary wavelet source which contributes to the amplitude at *P*. Depending on the total optical path length from *S* to *P*, the wavelets will reach *P* with different phase and amplitude. The composite amplitude at *P* can be found by integrating over all optical paths, with appropriate amplitudes and phases. If we restrict the case where the radius *r* is much less than *a* or *b*, then the amplitude can be treated as constant, and only the phase differences need to be considered.

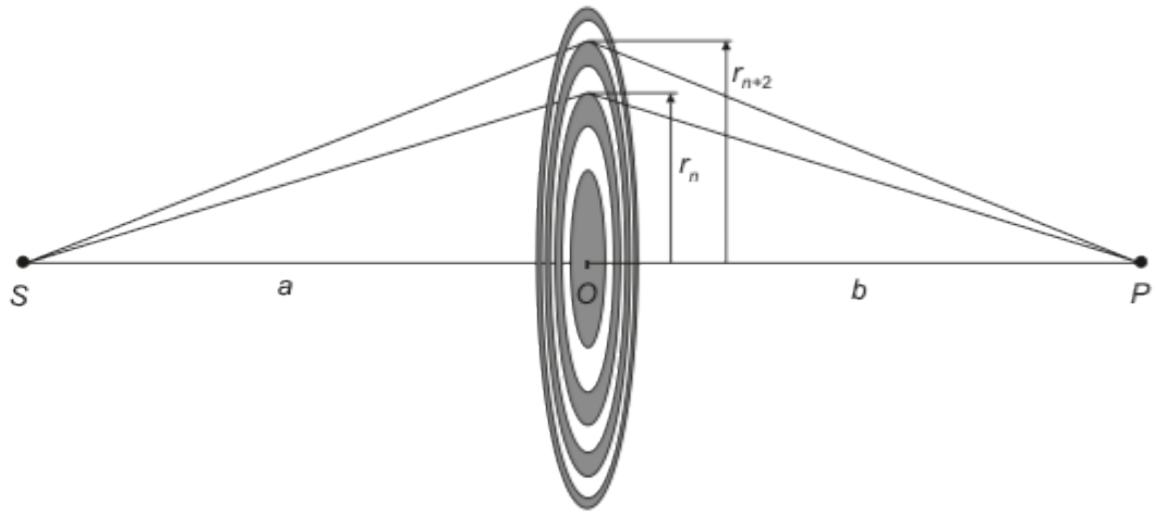

Figure 2.9 A diagram indicating the optical path length between the source point *S* and image point *P* via a zone boundary pair at radii r_n and r_{n+2}

From the optical paths shown in Figure 2.9 it is clear that with increasing radius the phase at *P* will oscillate between 0 and 2π, resulting in constructive and destructive interference. By blocking the contributions having phases between 0 and π with opaque zones, only contributions adding constructively at *P* will be transmitted. For this purpose each new zone must represent an optical-path-length increase of $n\lambda/2$ compared to the optical path length at the optical axis. The zone radii can now be determined by the Pythagorean theorem[32,33,34].

$$\sqrt{a^2 + r_n^2} = a + b + \frac{n\lambda}{2} \quad (2.1)$$

Solving for r_n :

$$r_n^2 = \frac{n\lambda(a+b)ab + \frac{1}{4}n^2\lambda^2\left(3ab + a^2 + b^2\right) + \frac{1}{8}n^3\lambda^3(a+b)\frac{1}{64}n^4\lambda^4}{\left(a + b + \frac{1}{2}n\lambda\right)^2} \quad (2.2)$$

If *a* is much less than *b*, and introducing the focal length of the Zone Plate as $1/a+1/b=1/f$, Eq. (2.2) can be simplified to

$$r_n^2 = nf\lambda + \frac{n^2\lambda^2}{4} \quad (2.3)$$

Another important consequence of the optical-path-length calculation is that the requirement of constructive interference is fulfilled also on other points than *P* on the optical axis due to higher diffraction orders. These points represent higher-order foci of order *m* (*m* is an integer) and are located at a distance *b*/*m* from *O*. They can be introduced into Eq. 2.2 just by replacing *n* with $n \cdot m$. For the ideal Fresnel Zone Plate it can be shown that the even orders (*m* even) cancel out. Figure 2.10 illustrates how the different orders are located along the optical axis[35].

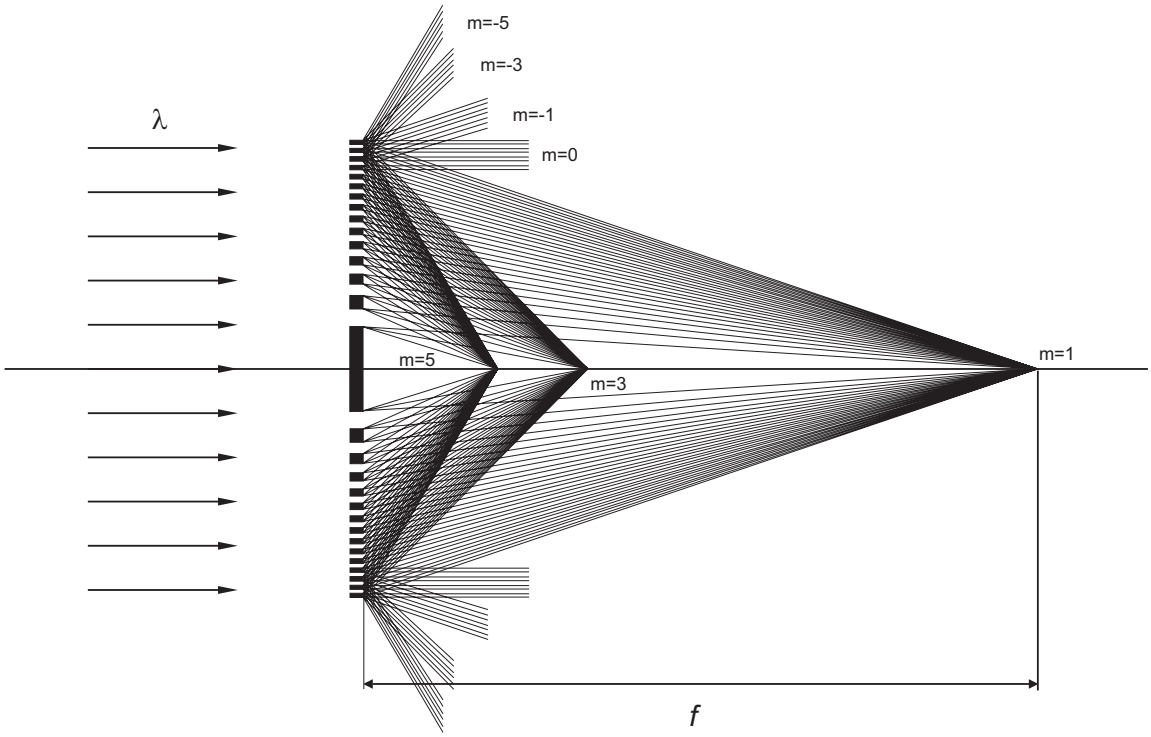

Figure 2.10 Focusing with a Zone Plate into the first three odd diffraction orders. The focal length for the first order is denoted *f*. Negative diffraction orders originating from virtual foci behind the Zone Plate are also indicated. In the figure, ray paths from the negative orders are only drawn for the outermost part of the Zone Plate for clarity[35].

The fraction of radiation diffracted into different orders decays with increasing diffraction order. The diffraction efficiency for a certain order is defined as the fraction of the incoming light that is diffracted into the specific order, which can be calculated by expressing the

amplitude transmission function of the Zone Plate as a Fourier series where the m^{th} coefficient of the series represents the complex amplitude diffracted to the m^{th} focus for an incoming wave of unit amplitude[38]. Therefore the diffraction efficiencies are given by the squares of these coefficients, which are $1/4$, $1/\pi^2$, $1/(3\pi)^2$, ..., $1/(m\pi)^2$, for the diffraction of order 0, ±1, ±3, ...,±m. The energy distribution can be described as: 1/2 is blocked by the opaque zones; 1/4 is contributed as undiffracted zero-order background; 1/8 is the background for nonconvergent negative-order diffraction. Only $1/\pi^2$=10% of the total energy contributes to the main focal length[36].

Lord Rayleigh provided further insight into diffractive lenses by considering what would happen if the phase of the light could be delayed in alternate zones by a half wave- length, i.e. π phase shift, rather than absorbing it using opaque zones. This concept was evaluated experimentally by Wood[37] in 1898 by bleaching a photographic Zone Plate, and it was found to yield more light at the point of focus. In contrast to amplitude Zone Plate, the zero-order diffraction from transparent zones and phase-shifted zones are of the opposite phase and cancel each other out. Therefore all foci gain by a factor of 4. In other words, this Wood Zone Plate (Figure 2.11c), or phase-reversal Zone Plate, can direct about 40% of the light into each of 2 lens powers, with the remaining light wasted in higher diffractive orders. This is a predecessor to the modern multifocal diffractive lens.

2.3.1.3 Monofocal Diffractive Lenses

A monofocal diffractive lens, sometimes named a kinoform[38,39], can be achieved if a phase delay of 1 wavelength is introduced at the Fresnel Zone boundaries (Figure 2.11b). The blaze profile within each zone of the diffractive lens provides perfect constructive interference at the focal plane for the design wavelength λ_0 (i.e., the wavelength that experiences a 2π phase jump at each zone boundary). Figures 11(c), known as phase reversal Zone Plate, and 11(d) illustrate different approximations to the desired blaze profile in Fig. 11(b) [40].

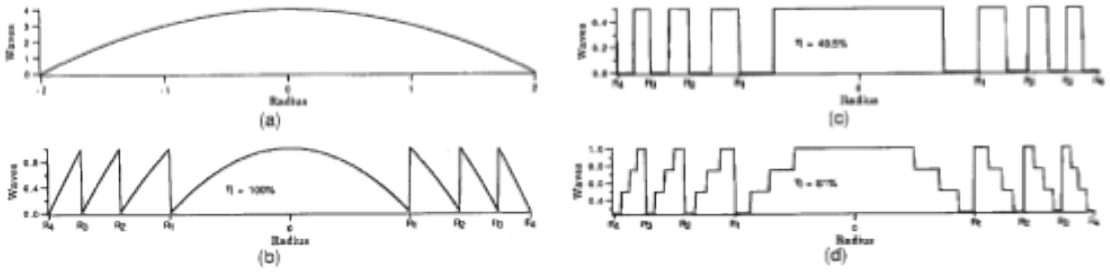

Figure 2.11 Diffractive lens construction: (a) conventional refractive lens, (b) diffractive lens with continuous quadratic blaze profile, (c) phase-reversal (or Wood) lens, (d) four-level approximation to quadratic blaze profile[40].

The efficiency of such diffractive devices is determined by how closely their stepped-phase profile approximates a true blaze. The theoretical efficiency at wavelength λ of an element with I steps designed for use at λ_0 is

$$\eta(\lambda, I) = \left| \mathrm{sinc}(1/I) \frac{\sin(I\pi\alpha)}{I \sin \pi\alpha} \right|^2 \quad (2.4)$$

where *sinc(x)= sin(πx)/πx* and *a=(λ0/ λ-1)/I* . The efficiency η(λ, I) plot for different numbers of steps I is illustrated in Figure 2.12 [41].

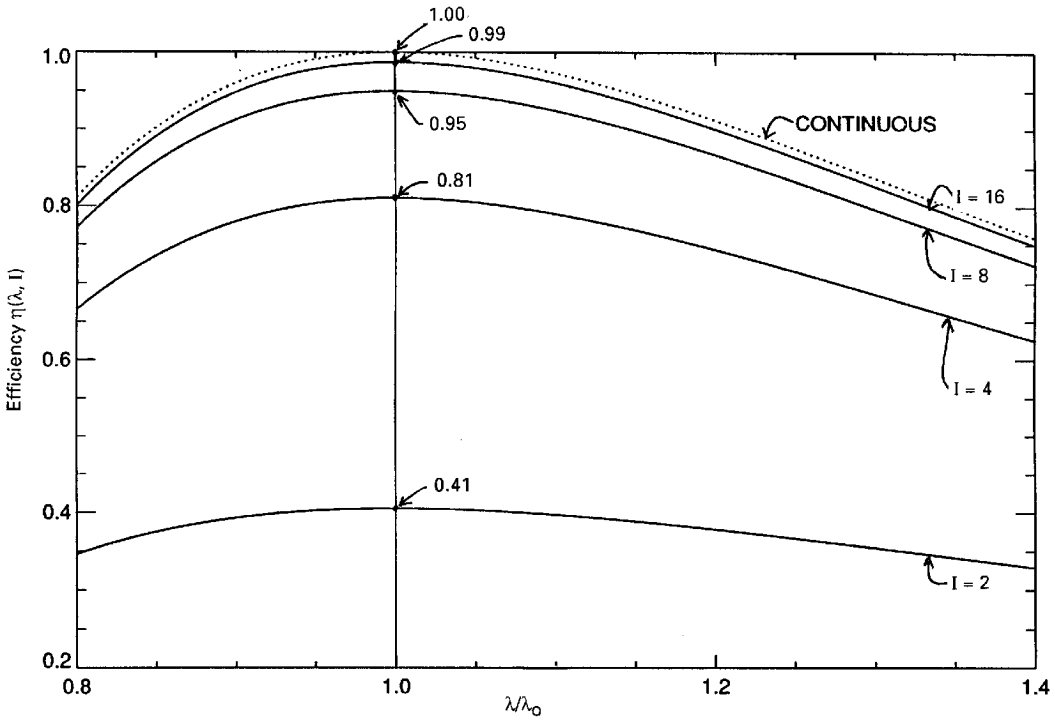

Figure 2.12 Diffraction efficiency of binary approximation of kinoform lens (continuous blaze profile) [41].

Thus, a conventional diffractive lens with blaze profile (Figure 2.11b), uses a single diffraction order in which the optical power of the lens is directly proportional to the wavelength of light (Figure 2.13a). With white light illumination, every wavelength focuses at a different distance from the lens. This strong wavelength dependence in the optical power produces significant chromatic aberration in the image, which is not acceptable for multicolor display purposes. To overcome such a challenge, more sophisticated version of diffractive lens, named as Multi-Order-Diffractive lenses (MOD), could be utilized. As illustrated in Figure 2.13b, with an MOD lens, the various diffractive orders bring different wavelengths to the common focal point[42].

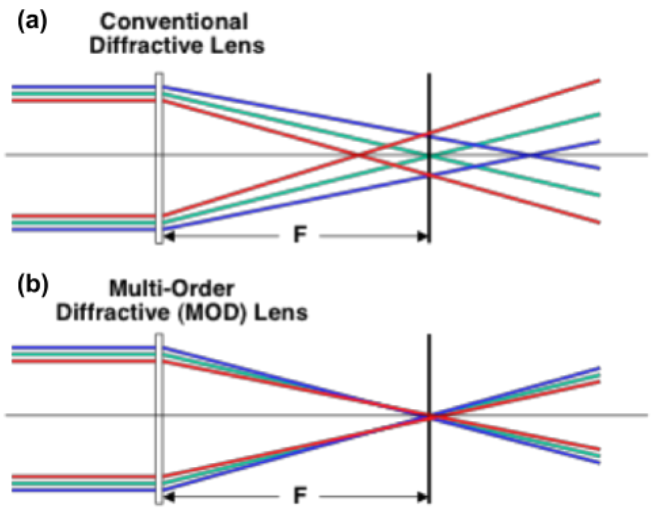

Figure 2.13 a) A conventional diffractive lens is highly dispersive and focuses different wavelengths of light to different focal positions, b) A MOD lens brings multiple wavelengths across the visible spectrum to a common focal point and is thereby capable of forming high-quality images in white light[42].

A MOD lens differs from the standard diffractive lenses described above in that the phase jump at the zone boundaries is taken to be a multiple of 2π, i.e., $\varphi(r_n) = 2\pi p$, where p is an integer ≥2, and the location of the zone radii are obtained by the solution of the equation $\varphi(r_n) = 2\pi pn$, where again $\varphi(r)$ represents the phase function of the emerging wave front. The number of 2π phase jumps, p, represents a degree of freedom for the designer[40].

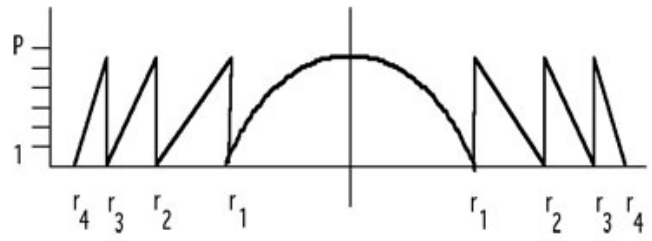

Figure 2.14 Cross section of a multi-order diffractive (MOD) lens. The phase jump at the edge of the various zones is 2πp, where p is an integer. The zone radii, r_n, are obtained by solving the equation $\Phi(r_n) = 2\pi pn$, where $\Phi(r)$ represents the desired phase function for the lens[43].

First-order properties of paraxial MOD lenses within the framework of the scalar diffraction theory were presented by Falkis et al[40], which we quote accordingly. The construction of the diffractive zone structure for Fresnel full-period zones is defined such that the optical path difference across the *j*th zone is equal to ($F_0 + jp\lambda_0$), where λ_0 is the design wavelength, F_0 is the focal length when the illumination wavelength $\lambda = \lambda_0$, and *p* is an integer that represents the maximum phase modulation as a multiple of 2π. In the paraxial region, the locations of the zones in the plane of the lens are given by[40]

$$r_j^2 = 2jp\lambda_0 F_0 \quad (2.5)$$

The optical phase introduced by the diffractive element is given by[44]

$$\Phi(r) = 2\pi\alpha p\left(j - \frac{r^2}{2p\lambda_0 F_0}\right), r_j \le r < r_{j+1} \quad (2.6)$$

where α is defined as the fraction of 2π phase delay that is introduced for illumination wavelengths other than the design wavelength and is given by[40]

$$\alpha = \frac{\lambda_0}{\lambda}\left[\frac{n(\lambda)-1}{n(\lambda_0)-1}\right] \quad (2.7)$$

where n is the index of refraction of the material in the grating region. The maximum height of the surface relief is given by[40]

$$h_{\max}(r) = \frac{p\lambda_0}{n(\lambda_0) - 1} \quad (2.8)$$

In a manner similar to that used in Ref. [44], the amplitude transmission function of the diffractive lens can be expanded as a Fourier series to give[40]

$$t(r) = \sum_{m=-\infty}^{\infty} \exp\left[-i\pi(\alpha p - m)\right] \times \operatorname{sinc}(\alpha p - m) \exp\left(-\frac{i\pi m r^2}{p\lambda_0 F_0}\right) \quad (2.9)$$

where $\operatorname{sinc}(x) = \sin(\pi x)/(\pi x)$ and m denotes the mth diffraction order. It is important to note that the transmission function in Eq. (2.9) represents a diffractive lens within the paraxial approximation and that transmission functions that describe other diffractive lenses (e.g. anamorphic or aspheric) are possible. It is interesting to compare Eq. (2.9) with the transmission function of a conventional refractive lens[45] given by

$$t(r) = \exp\left(-\frac{i\pi r^2}{\lambda F}\right) \quad (2.10)$$

where F is the focal length, which depends on the material properties of the lens. A comparison of Eqs. (2.9) and (2.10) suggests that there are an infinite number of focal lengths given by[46]

$$F(\lambda) = \frac{p\lambda_0 F_0}{m\lambda} \quad (2.11)$$

Where λ_0 is the designed wavelength, F_0 the desired focal length and m, the diffraction order. It is interesting to note that when the quantity in Eq. (2.11), $p\lambda_0/m\lambda$, is set equal to unity,

several wavelengths within a given band can come to a common focus. Clearly p is a construction parameter and is usually constant across the lens radius, and the wavelengths that are focused to a common point are chosen from a set of diffraction orders (i.e. MOD lenses). Although a diffractive lens with a maximum phase modulation of 2π (i.e. conventional diffractive lens) can allow a mutual focus for simple harmonics of the design wavelength, the parameter p now offers a mechanism to control specific wavelengths in a given band or bands that will come to a fixed focus. This property allows the design of achromats and apochromats by the use of a single diffractive surface.

The scalar diffraction efficiency, η_m, of the mth diffracted order is given by the squared modulus of its Fourier coefficient in Eq. (2.9), i.e.,

$$\eta_m = \mathrm{sinc}^2(\alpha p - m) \quad (2.12)$$

The diffraction efficiency given by Eq. (2.12) is unity when the argument of the sinc function is equal to 0. This condition can allow for high diffraction efficiency for several wavelengths. For example, consider the case of a MOD lens operating in the visible region with p = 10. Figure 2.15 illustrates the wavelength dependence of the diffraction efficiency for a range of diffracted orders, with material dispersion neglected. The peaks in diffraction efficiency occur at precisely those wavelengths that come to a common focus [see Eq. (2.11)], i.e.,

$$\lambda_{peak} = \frac{p\lambda_0}{m} \quad (2.13)$$

Also note that the material dispersion [see Eq. (2.7)] is an important parameter that must be retained in a detailed optical design.

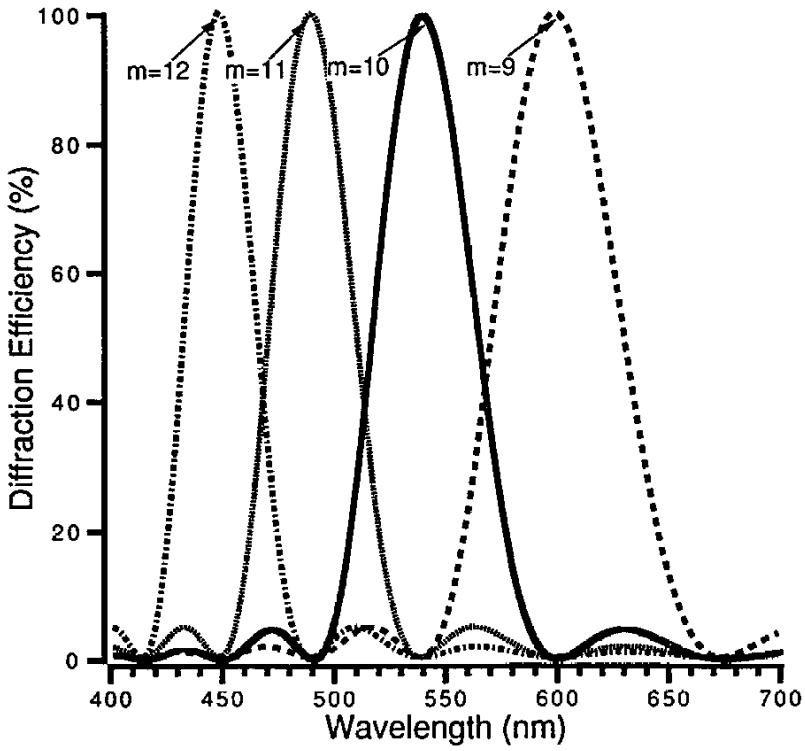

Figure 2.15 Diffraction efficiency of the *m*th diffracted order versus wavelength for a MOD lens[40] with $p = 10$.

Using Eq. (2.13), one can choose the parameters p and m that can allow high diffraction efficiency for certain bands in a given spectrum. The center wavelength of each of these bands comes to a focus a distance F_0 behind the lens. To illustrate the spectral characteristics of a MOD lens, Faklis[40] designed and fabricated an optical element for operation in the visible spectrum at $p = 2$ and $m = 2, 3$ with design wavelength of 640 nm, which gives a third-order wavelength of 427 nm. For this particular case, the integrated diffraction efficiency of the element was measured to be 91% for $m = 2$ and 3.

Thus to create an in-focus image of a high resolution multicolor pixel on retina, MOD elements could eventually be co-integrated with display chip, but the first step toward realization of contact lens embedded display with in-focus pattern would be to test the feasibility of collimation of a single color display element using the basic diffractive lens, i.e.

Fresnel Zone Plate (FZP). So we tried to design and integrate an LED/FZP system, which is described in the following section.

2.3.2 LED-FZP System, Experimental

2.3.2.1 Design

To collimate the LED light output, the source needs to be positioned at the main focal point of the FZP. In our design FZPs were intended to be integrated on the opposite side of sapphire wafers supporting the LED epitaxial layers on the surface; hence, the wafer thickness determined the required focal distance of the lens. With successful results of wireless powering and control achieved with GaN LEDs, we decided to continue the optical design utilizing same structure. Hence, with a measured peak wavelength of 475nm for the LED structure[12], Fresnel Zones were calculated by applying equation (2.3). We conducted two simulation approaches in ZEMAX-EE to check our design: first, we simulated the FZP and its focusing behavior, and second, we simulated the LED structure with integrated FZP.

In the first approach, in order to model diffractive effects, we used Physical Optics Propagation (POP) analysis of sequential mode ZEMAX. We implemented our opaque zones of FZP as concentric obscurations (Figure 2.16a) and used a coherent Gaussian beam with 475 nm wavelength as an illumination source. The Zone Plate created a high intensity point at a designed focal distance (Figure 2.16b)

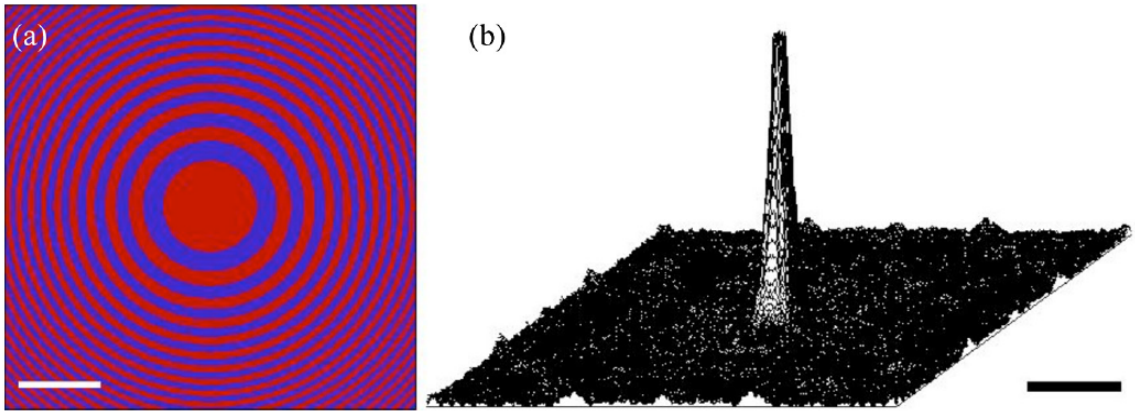

Figure 2.16 a) An FZP implemented as obscurations in ZEMAX; the scale bar is 20 µm. b) Physical Optic Propagation analysis of FZP: 60 µm waist Gaussian beam, illuminated through the designed FZP focuses at the desired 275 µm; the scale bar is 10 µm

To model the InGaN LED structure, we used the Non-Sequential mode of ZEMAX. The non-sequential mode is not capable of modeling amplitude FZP, although it can model phase type FZP using Binary2 Surfaces. As phase and amplitude type FZPs are analogous in focal distance measures, we implemented the FZP as a Binary2 Surface to determine the light distribution pattern.

Considering the dimensions we calculated for fabrication, we implemented the LED p-metal contact, p-GaN region, n-GaN region, sapphire substrate, and FZP using a mirror layer, a GaN cylinder with embedded source volume, a GaN rectangular volume, a sapphire rectangular volume, and a Binary2 surface, respectively.

Positioning the LED active region at the FZP's first order focal distance would collimate the largest fraction of incident light, while subsidiary focal points would converge smaller fractions. Having multiple focal points, the functionality of the LED/FZP system can be tested by tracking the footprint of subsidiary focal points using regular optical microscopes, while measuring the beam angle of collimated output caused by main focal point requires more complex side-view microscopy. Hence, to simplify the required equipment for testing we aimed for detecting the image created by the *f/3* subsidiary focal point. Following the

same strategy in the simulation, the *f*/3 subsidiary focal point creates a high-intensity spot at a distance of 250 µm from the surface (Figure 2.17a), while the LED output without integrated FZP created a non-focused result at the same distance (Figure 2.17b).

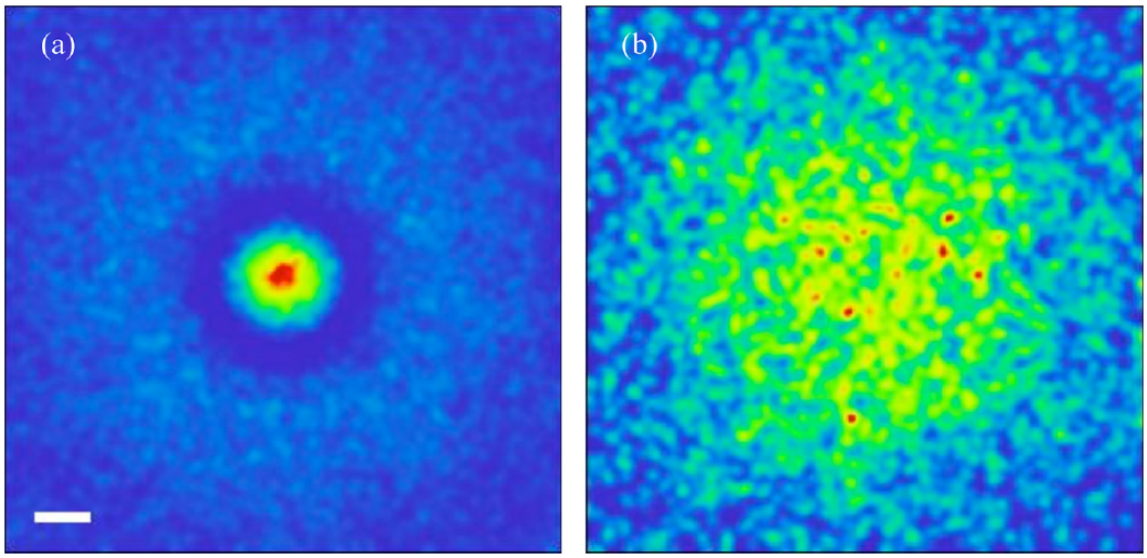

Figure 2.17 Simulated light intensity maps. a) LED structure modeled in non-sequential ZEMAX with integrated Binary2 surface as FZP gives a focused spot caused by subsidiary f/3 focal point at 250 µm distance from the surface, b) while the LED without integrated Binary2 surface does not have the focusing behavior. The scale bar is 100 µm.

2.3.2.2 FZP fabrication:

A nominal FZP is comprised of concentric rings with progressively increasing radius and decreasing width moving away from the center. As the outermost ring in design was in submicron range, we used electron beam lithography to create the structure with high fidelity. To develop the process we made our first attempts on a blank C-plane sapphire substrate.

After a standard cleaning procedure of Acetone/IPA/DI rinse and dry, to remove residual water off the surface we baked the wafer at 180 C for 3 minutes. For better lift-off results we used a bilayer stack of E-beam resist with a more sensitive layer at the bottom that requires a lower exposure dose. Hence when exposed as a part of a bilayer stack, the bottom layer gives

a wider line width for the same dose than the top layer, which results in an undercut profile that aids the lift-off. For the bottom layer we spin coated the wafer piece with 7% P(MMA-MAA) copolymer (MicroChem Corp., MA) for a preferred thickness of 200 nm and baked it at 180 C for 3 minutes, followed by spin coating of 2.5% 495PMMA A resist (MicroChem Corp., MA) in Anisole for a thickness of more than 100 nm as the top layer, followed by the same baking steps. As sapphire is not conductive, in order to prevent charging up the surface during the E-beam lithography step, we sputtered a very thin layer of Pd/Au (less than 10 nm) using a small sputtering machine (Quorum, Q150RS). Then the piece was loaded on the electron beam lithography machine (JOEL JBX6300).

To choose the optimum exposure dose, we conducted a few test runs with different doses. Higher doses resulted in overexposure for larger patterns at the center while underexposure of outer most rings was observed for lower doses (Figure 2.18) Once the parameters were optimized, electron beam writing was conducted. Then we etched the thin PD/Au layer by dipping the sample in TFA Gold etchant (Transene Company, Inc.) for 10 seconds. The sample was developed in standard PMMA developer,1:1 mixture of Methyl-Isobutyl-Ketone (J.T Baker Inc.) and IPA, then rinsed with IPA/DI water and air dried. Prior to depositing the metal layer the sample was attached to a 4-inch silicon wafer as a holder. To get minimal step coverage, we mounted the wafer on a custom-made vertical wafer holder in the deposition chamber of an E-beam evaporator. 100 nm of chromium was deposited and the piece was then soaked in acetone for lift-off, leaving metal rings as opaque zones of FZP (Figure 2.19h, Figure 2.20).

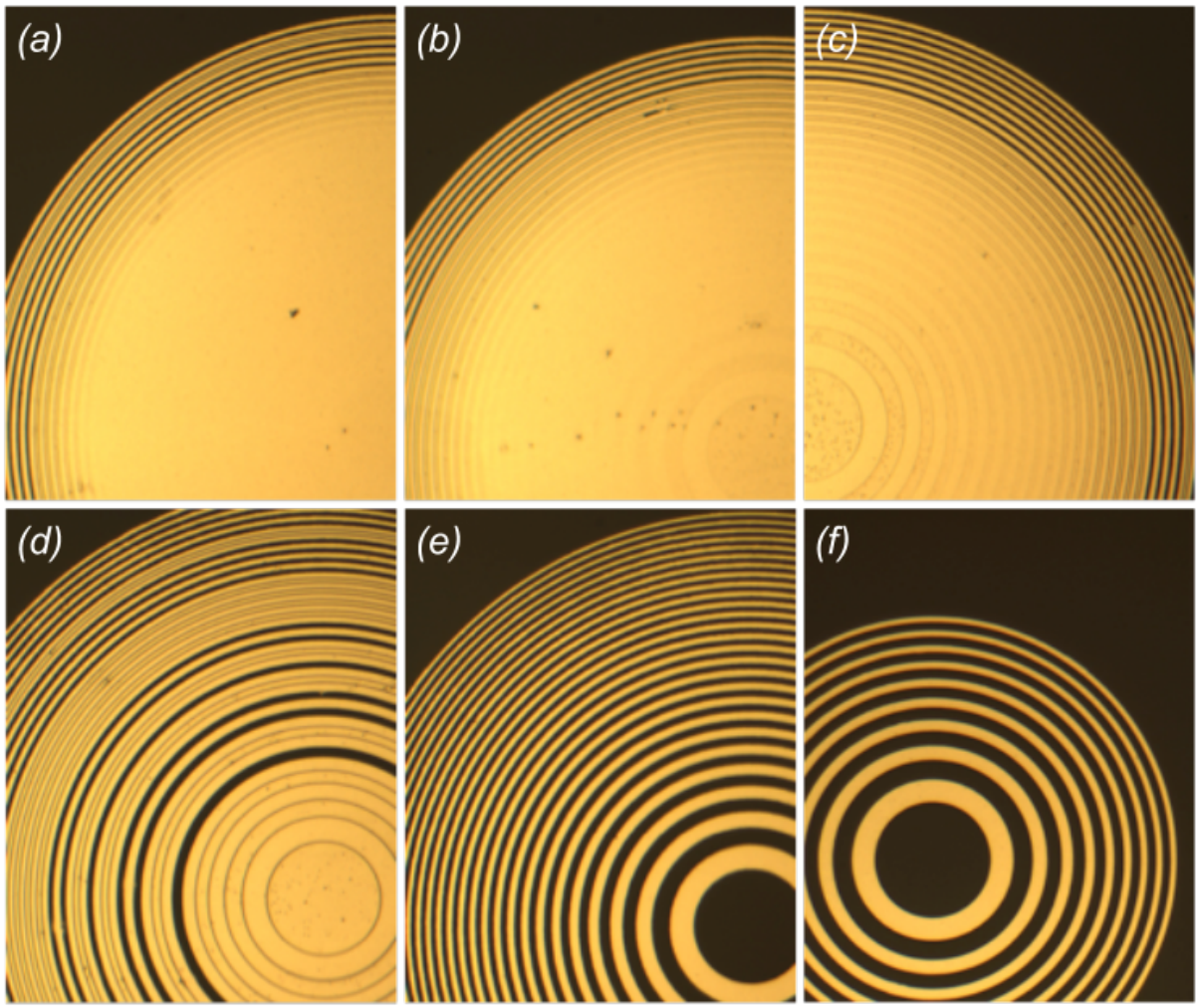

Figure 2.18 Different doses can overexpose larger features (innermost rings) and underexpose smaller features (outermost rings). Lift-off result of different exposure doses in uC/cm^2: a) 500, b) 475, c) 425, d) 325, e) 275, f) 150.

2.3.2.3 Blue micro LED fabrication:

We started with epitaxial layers of InGaN/GaN grown on standard 2 inch, 435 um thick c-plane sapphire wafers by metal organic vapor phase epitaxy (MOVPE) with the same characteristics reported in [12] (Figure 2.19a).

First, we defined the size and shape of each LED by evaporating a 120 nm thick layer of Ni to protect the p-GaN region (circular shape of 60 μm diameter in this case) during the chlorine-based Inductively Coupled Plasma Reactive Ion Etching (ICP RIE). We used AZ5214E (MicroChem Corp., MA), an image reversal photoresist, to gain sloped sidewalls

and good lift-off results. The photoresist was spun coated, prebaked, exposed under a mask, hard baked, and finally flood exposed and developed resulting in a ~1.1 μm thick pattern. After development, the Ni layer was deposited by E-beam evaporation. The wafers were soaked in acetone for lift-off and then rinsed with isopropyl alcohol (IPA) and air dried (Figure 2.19b). To reach the n-GaN region and make metal connections, we used a chlorine-based ICP RIE to remove about 800 nm of top surface- p-GaN/multi quantum well stacks/ and partially the n-GaN layer. After etching, the Ni layer was removed by soaking the wafer in a mixture of 1:3 HCl:HNO3 (Figure 2.19c). To make metal connections for p-GaN, we used patterned AZ5214E photoresist, E-beam evaporated Ni:10nm /Ag:70nm /Au:150nm layer, and performed a lift-off (Figure 2.19d). P-GaN contacts then were annealed at 500 C for 5 minutes in nitrogen ambient. After a similar photolithography step, the n-GaN metal connections were deposited and lifted off as Ni: 20nm/Al: 300nm/Au: 200nm (Figure 2.19e). After the completion of LED metallization, the wafers were lapped and polished (Valley Design Corp., CA) in order to make the final LED chip thin enough to be embedded in a contact lens template, which resulted in an actual thickness of 273 μm – 276 μm (Figure 2.19f).

As the FZP must be fabricated on the lapped and polished side of the wafer, we needed to fabricate alignment marks for electron-beam lithography. We need to fabricate the marks from a material which can be imaged easily by scanning electron microcopy (SEM) and which has good adhesion to sapphire. Chromium was a good option as was reported in a process to mask sapphire during anisotropic etching and for making the alignment marks[46].

The alignment marks were designed large enough (~10 μm) to allow photolithographic fabrication. Negative photoresist, nr7-1000 (MicroChem Corp., MA), was spun coated and patterned through a standard lithography process resulting in a 1.2 μm thin film. A 100 nm thick layer of chromium was evaporated. Then the wafer was soaked in acetone for lift-off,

rinsed with IPA and de-ionized (DI) water and air dried (Figure 2.19g). The wafer contained more than 2000 LED chips. To minimize losses during different tests the wafer was saw-diced into smaller pieces by the following process: The sapphire wafer was mounted on a 4 inch silicon wafer as mechanical support by applying Crystal Bond. Using diamond resin blades (Thermocarbon Blades) mounted on K&S dicing machine, we cut small 9 mm squares. Conducting 5 pairs of perpendicular cuts, the wafer was soaked in acetone to release the pieces from the handle wafer. Pieces were then IPA/DI water rinsed, air dried, then prepared for Electron Beam Lithography (EBL) following the process developed earlier. Then a piece was loaded on the electron beam lithography machine (JOEL JBX6300) and, after proper alignment of the FZP pattern in front of the LED mesa, it was exposed. Then the pattern was developed and the 100nm Cr layer was evaporated through the lift-off procedure.

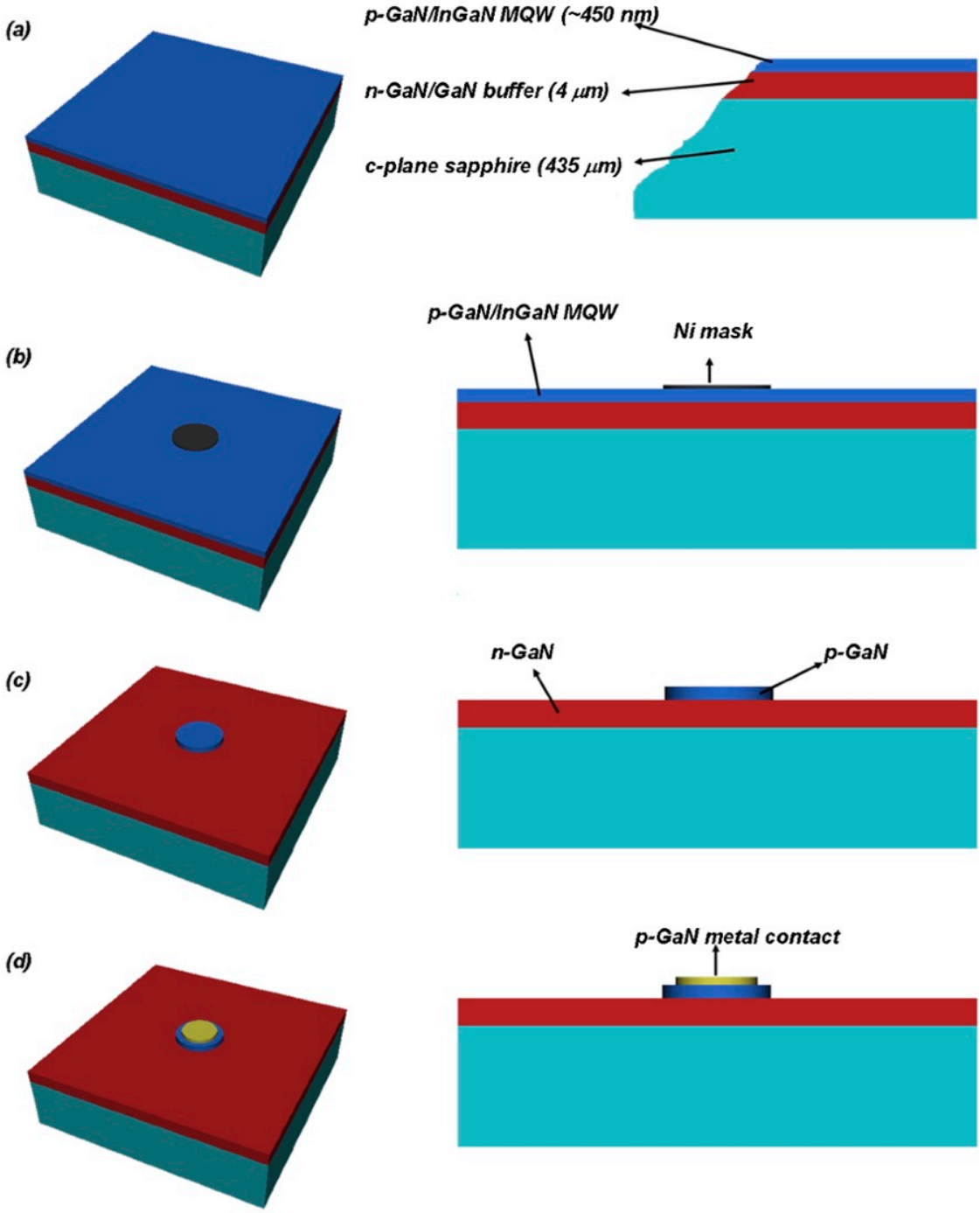
(a)
p-GaN/InGaN MQW (~450 nm)
n-GaN/GaN buffer (4 μm)
c-plane sapphire (435 μm)
(b)
p-GaN/InGaN MQW
Ni mask
(c)
n-GaN
p-GaN
(d)
p-GaN metal contact

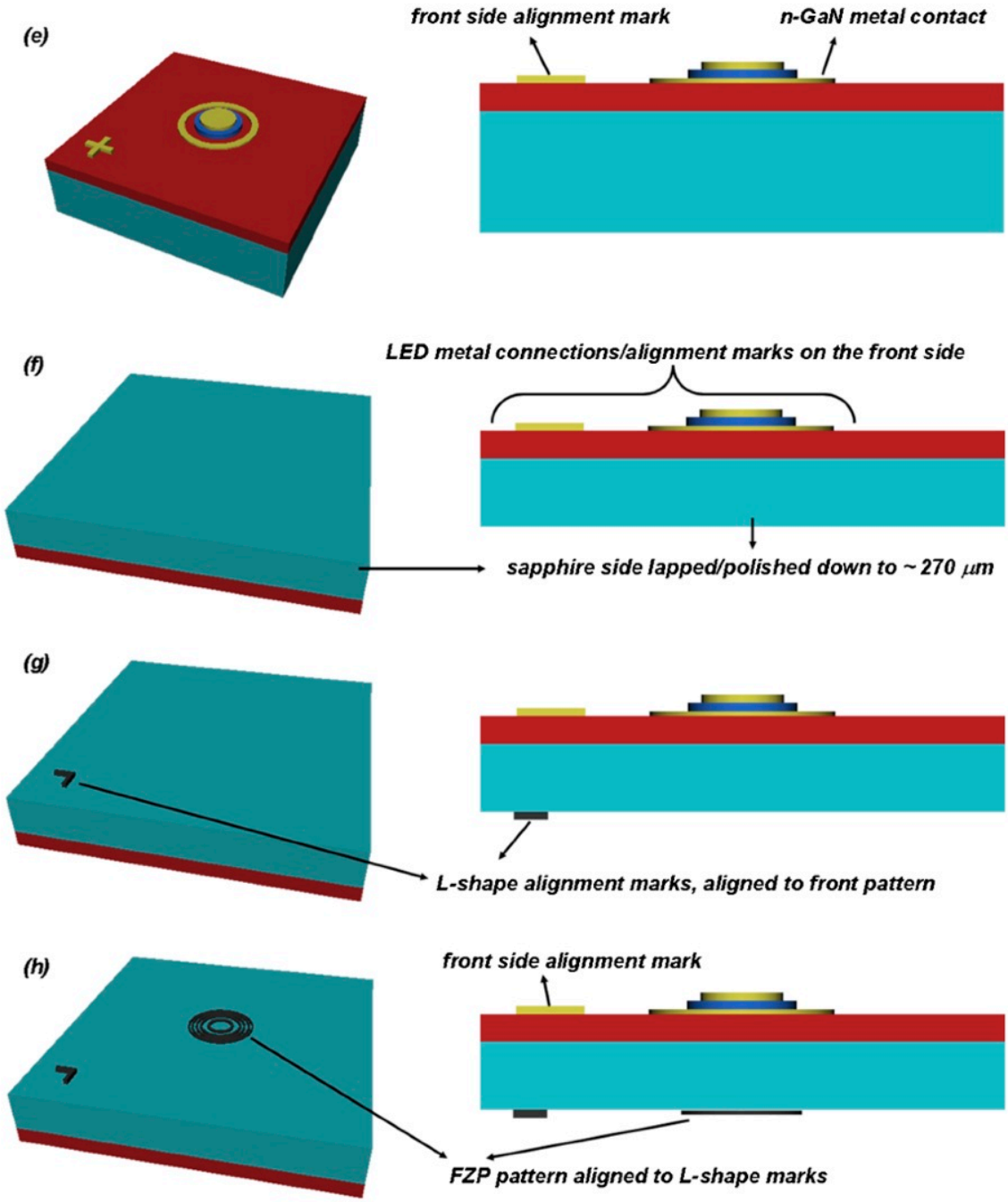
(e)
front side alignment mark
n-GaN metal contact
(f)
LED metal connections/alignment marks on the front side
sapphire side lapped/polished down to ~ 270 μm
(g)
L-shape alignment marks, aligned to front pattern
(h)
front side alignment mark
FZP pattern aligned to L-shape marks

Figure 2.19 LED and FZP fabrication process, a) Sapphire substrate with epitaxially grown layers of p-GaN/InGaN MQW/n-GaN/GaN buffer, b) Ni deposition as etch mask, c) Chlorine-based ICP RIE etching of top layer (p-GaN/ InGaN MQW) to reach the n-GaN region, then removing the Ni mask, d) p-contact metallization Ni/Ag/Au, e) n-contact and cross shape mark for backside alignment deposition, f) sapphire side lapped and polished down to ~270 mm, g) Aligned to front side cross marks, L-shape alignment marks deposited using Cr, h) FZP opaque rings deposited after Electron Beam Lithography.

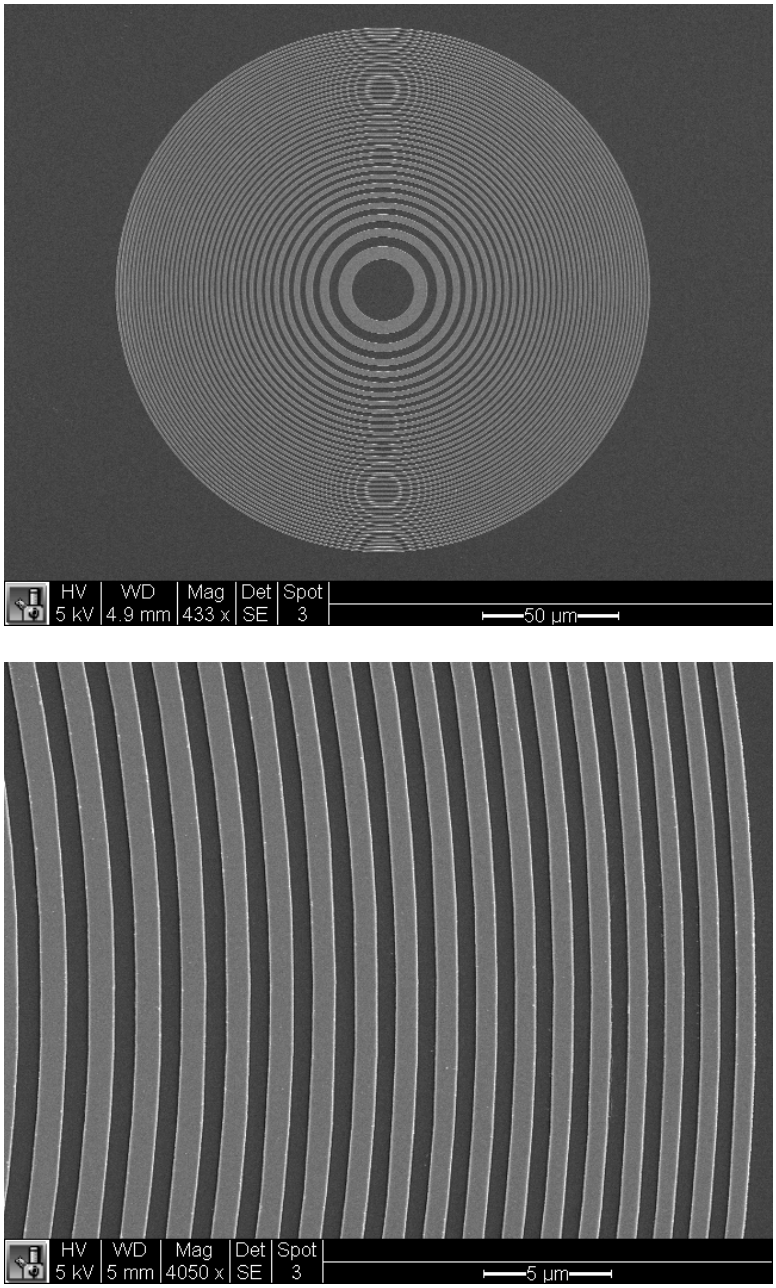

Figure 2.20 SEM image of a 275um foci Fresnel Zone Plate

Each wafer piece contained 100 LED chips that had to be separated for individual testing. Because of the fragility of sapphire and the crystal orientation used in our design, mechanical dicing/scribing would cause unacceptable chipping through the dicing path (Figure 2.21). To minimize the damage to the chips and fragile metal lines, we used a laser to scribe the pieces. The pieces were scribed down to ~200 um using a DPSS laser at 266 nm (JPSA, Inc.,NH) and separated to single chips by applying manual pressure to the edges.

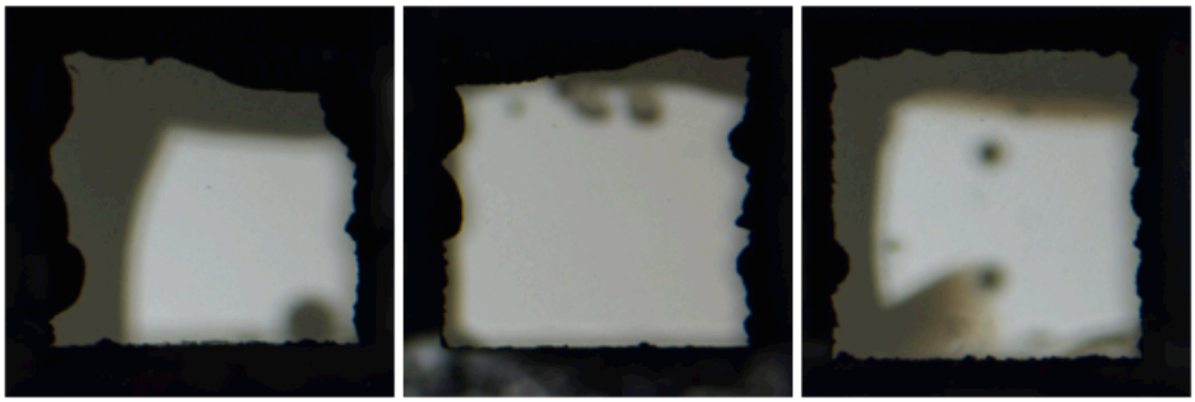

Figure 2.21 Severe chipping of sapphire resulted from saw dicing due to crystal orientation.

2.3.2.4 Template Fabrication and assembly

As we will eventually assemble the LED chips on a flexible contact lens template, we used transparent polyethylene terephthalate (PET) to make templates for testing our chips. Simplifying the previously described template fabrication process by omitting the Antenna seed layer deposition and electroplating steps, we fabricated testing templates with a housing for the LED/FZP integrated system and 2 metal interconnects to access the LED pads for power injection.

Following the process, described in section 2.2.2, we assembled the FZP/LED integrated system on the templates.

2.3.2.5 Testing and Results

In addition to integrating Zone Plates in front of LED structures, as described earlier, we also fabricated Zone Plates on bare sapphire substrates to optimize the fabrication parameters for the E-beam lithography that we utilized to conduct several tests.

One of the first tests was to see the wavelength dependency of FZP focusing behavior. An aperture with a custom pattern was located in front of a white color illumination source, far from (~20 cm) FZPs with 325um focal distance designed for 475nm wavelength. As expected, the lens creates a real image of a far field pattern at 1^{st} and 3^{rd} order foci by diffracting the respective wavelength (Figure 2.22).

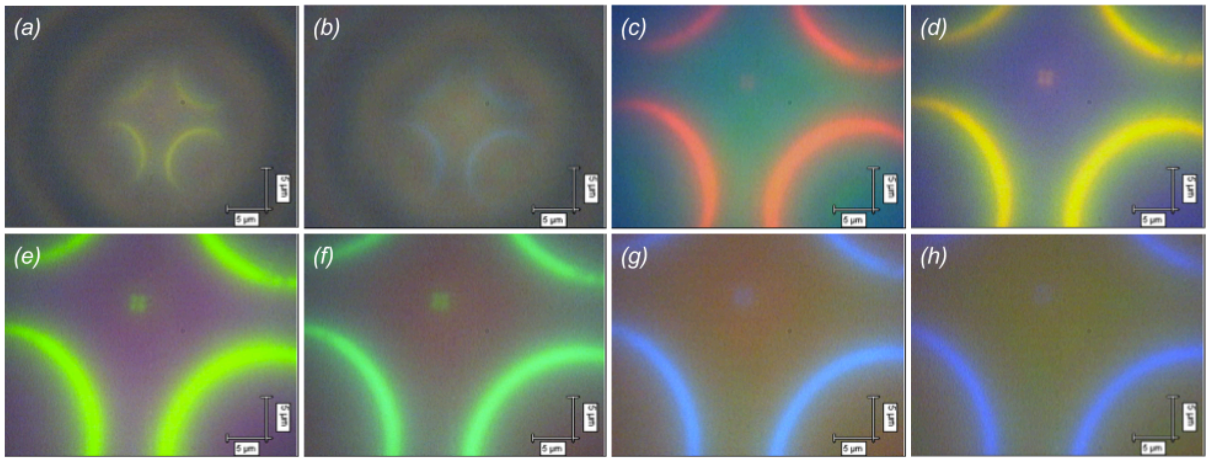

Figure 2.22 Far field image of a custom pattern white source diffracted at designated focal distance of an FZP with 325um foci for 475nm (blue) at different distances of its surface image created by f/3 subsidiary focii a)84um and b)103um. Images created by main power of lens at c) 236um, d) 261um, e) 282um, f) 300um, g) 325um, h) 345um.

In another test we put a sapphire wafer with 450um focal FZP patterns 5 mm away from an illuminating LED chip with a complex pattern (Figure 2.23a) under an optical microscope (ML7000, MEIJI TECHNO Co., Japan). Initially we focused on the FZP surface, and then by moving the microscope objective, we changed the objective focal plane and were able to detect an upside-down image of the LED chip in front of the FZP (Figure 2.23b).

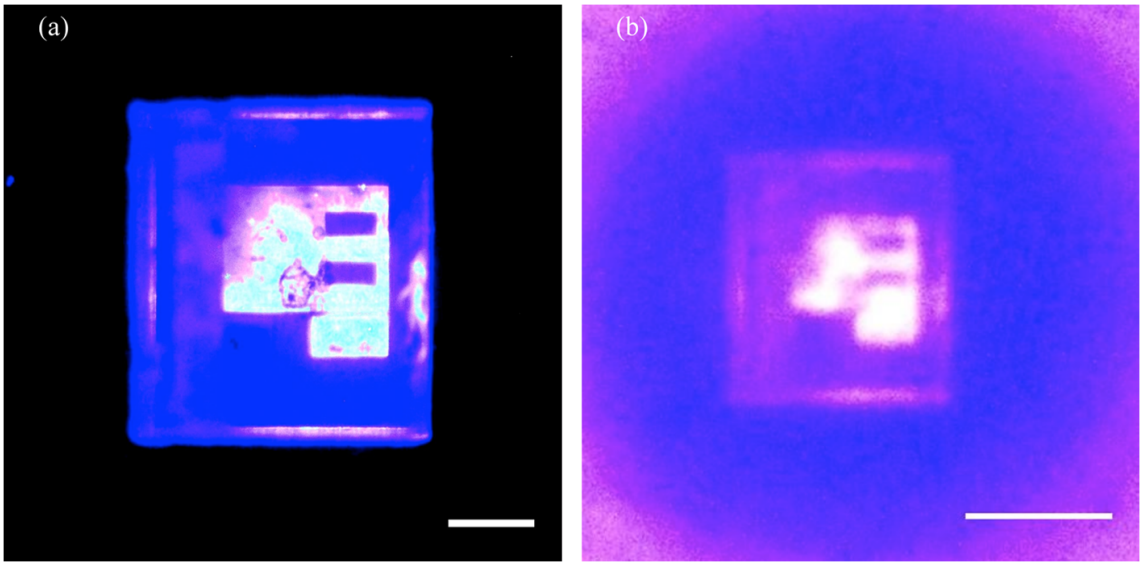

Figure 2.23 a) Optical microscope images of the rectangular test LED chip with pre-determined illumination pattern. The scale bar is 200 µm. b) FZP creates an upside-down image of the LED chip (which is ~5mm away from the FZP) approximately at the focal point. The FZP is visible as shadowed blue circle and the LED chip image is recognizable as the rectangle with a bright illuminated pattern (we flipped the image to make the object and image comparison more convenient). The scale bar is 50 µm.

As the simulation results of the LED with integrated FZP indicate, we expect the Zone Plate to focus the light at a point in front of the structure while the LED without a Zone Plate should have a diverging output. The assembled LEDs were put under the microscope objective, while current was fed by probe-station needles. The LED pixel (Figure 2.24a), with integrated FZP, produces a bright spot resulting from the f/3 subsidiary focal point at ~230 µm from FZP surface (Figure 2.24b). This positioning concurs with the thin lens formula approximation and simulations prediction of 250 µm.

With subsidiary foci creating a real image in front of the FZP, the main focus creates a magnified hovering ghost image behind the chip, in front of the eye (Figure 2.24c, d). These results verify the functionality of the Zone Plate in collimating the pixel output.

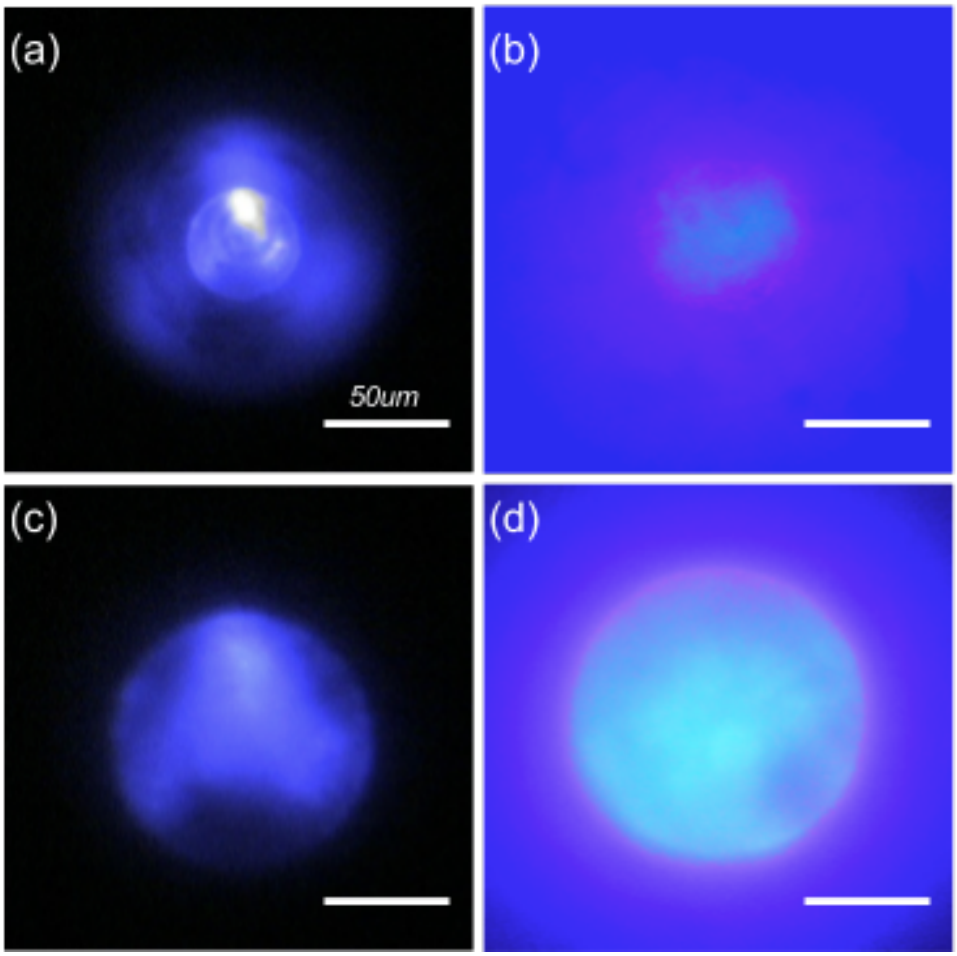

Figure 2.24 Testing of 2 different LEDs with an integrated FZP under an optical microscope: a) 50 µm wide LED pixel #1. b) Real image of LED pixel #2, focused at 230 µm from FZP surface in front of system, created by f/3 subsidiary focal point. c) Upright ghost image of LED pixel #1 created in the back plane of system. d) Ghost image of LED pixel #2 in the back plane of the system. Scale bars are 50 µm.

2.3.3 LED-FZP Discussion and Summary

We were able to verify the functionality of the designed Zone Plates and detect the LED output focused by the *f*/3 subsidiary focal point at the expected location and hovering ghost image behind the lens. However, there are several parameters that could be optimized in future implementations to make the LED/FZP system output more efficient and applicable for multicolor display purposes. Noted previously that there is a 10% limit for the diffractive efficiency of the amplitude-type Zone Plate, which could be increased to 40% by using a phase-type FZP. This is achievable by adding a sapphire etch step of 308 nm to make a π

phase shift. This etch could be performed after deposition of chromium layers (exactly as in the amplitude–type design) and utilizing them as sapphire etch masks[46]. φ would be the phase shift occurring[47] using a wavelength of λ after passing a layer of material with thickness of t and refractive index of n :

$$\varphi = 2\pi (n-1)t/\lambda \quad (2.14)$$

The efficiency could still be enhanced by increasing the π phase shift quantization illustrated in Figure 2.11c, d. For example, increasing the phase change quantization from two levels (0 and π) to four levels (0, π/2, π, 3π/2) would increase the efficiency up[48,49] to 81% (Figure12). This approach adds two more Electron Beam Lithography/etch mask deposition/anisotropic sapphire etching steps to the process, compared to a two-level phase type FZP. It also requires precise alignment. Note that special care is needed to protect the phase pattern during the molding process in the contact lens – for example, by bonding a flat transparent thin glass layer to the Fresnel Zone after etching. No matter how close we are able to approximate the ideal blaze pattern with binary step phase Zone Plate, the lens focusing/collimation behavior is highly dependent on the wavelength; this is a major deficiency for contact lens embedded multicolor display. As introduced in section 2.3.1, by utilizing an MOD component, one can make several wavelengths to a mutual focus. Fabrication of a binary approximation of an MOD through e-beam lithography increases writing/masking/etching steps by a factor of p, which is not practical for large values. For example, an MOD with p=10, λ_0=550nm which has mutual focusing/collimation for peak wavelengths of 460nm,540nm,650nm at diffraction orders of m=5, 6, and 7 requires a surface relief of ~7um calculated by Eq.(2.8). Such structures can be directly transferred on substrate through Focused Ion Beam (FIB) milling[50-53].

Another point to consider is that a lens can do an excellent job of collimating an idealized point source located at its focal distance. In real life, no source is a true point, as LEDs can be

quite small, so with enough distance between the lens and the LED, the lens may be approximated as a point source. Thus a Fresnel lens can be used to collimate the LED output. A rule of thumb for the distance at which the LED die can be approximated as a point emitter is given according to the far field region convention[33]:

$z > a^2/\lambda$ (2.15)

where z is the LED to lens distance, a is the pixel size and λ is the wavelength of the light. For the current structure with 275 μm LED-lens distance and 475nm wavelength, proper pixel size would be less than 11 μm, which is achievable through conventional photolithography. Decreasing the LED size not only makes the LED more similar to a point source that gives more uniformity in the collimated output but also increases the pixel count on the limited size display chip. This consequently decreases the electrical power required per pixel, as is preferred for such a wireless powered system.

Chapter 3 Universal Basic Identification Tag

3.1 Introduction

It was noted earlier that the dominant trend in industry is toward smaller products with more capabilities. With available miniaturization techniques and the ubiquity of the global network, we envision assigning a digital identity to physical objects in order to include them in cyberspace. The approach is to attach a tag that can be mass-produced at a low cost and can communicate wirelessly with each object. The tag is read-writable and holds the unique ID of the physical object. Further information about the ID can be stored in the cloud so that the tag itself does not need to have a very large permanent memory. In order to seamlessly integrate the tag in physical objects of various sizes, the tag must to be very small. The infrastructure of such a system can be illustrated as in Figure 3.1. Data can be assigned to and readout from tag by a custom Reader circuit-controlled by a conventional smartphone. Information such as technical specs, manufacturing date and corporation, vendors, current/previous owners or any other relevant data about the object (ID) can be stored on the cloud database.

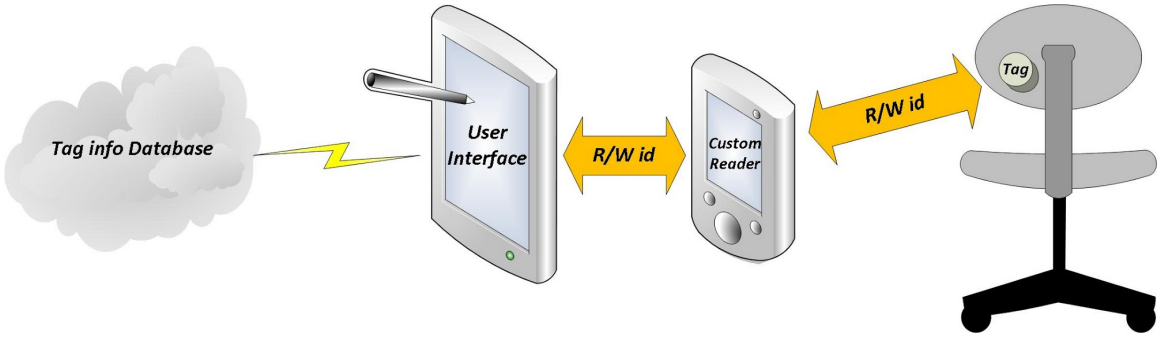

Figure 3.1 UBITag infrastructure: A miniature generic tag attached to a physical object loaded with information such as ID, assigned and readout by a custom Reader, controlled through a use interface on a conventional mobile device. Information about the ID is stored in the cloud.

Establishing the infrastructure illustrated in Figure 3.1 can be accomplished by utilizing conventional identification tags such as RFID. But because of their fundamental miniaturization limit, the range of the object sizes they can be seamlessly attached to would be limited. The general achievable harvesting efficiency through an RF pathway is usually higher than that of other transducer technologies (Table 3.1) [54], but this efficiency drops precipitously if the antenna is much smaller than the electromagnetic wavelength[55]. Antenna efficiency is the measure of the antenna's ability to transmit the input power into radiation[55]. The total antenna efficiency is the multiplication of different types of efficiencies, which is affected by the losses within the antenna itself and the reflection due to the mismatch at the antenna terminal. The radiation efficiency of the antenna can be computed as the ratio of the radiated powers to the input power, which is only related to the conduction losses and the dielectric losses of the antenna structure:

$$\eta_a = \frac{R_{rad}}{R_{rad} + R_{ohmic}} \quad (3.1)$$

While the total efficiency of the antenna with presence of a matching network would be[56,57]:

$$\eta_s \approx \frac{\eta_a}{1 + \frac{Q_a}{Q_m}} \quad (3.2)$$

Where R_{rad} and R_{ohmic} are radiation and ohmic loss resistances, Q_a is the radiation quality factor and Q_m is quality factor of matching network.

Electrically small antenna (ESA) is usually defined as one whose maximum dimension is less than $\lambda/2\pi$ and may be enclosed in a sphere of radius *a*, defined by H. A. Wheeler[58,59].This relation is often expressed as $ka<0.5$, where *k* is the wave number and equals to $2\pi/\lambda$. The ESA situation is illustrated in Figure 3.2.

Table 3.1 Characteristics of various energy sources available in the ambient and harvested power [54].

Source	Source power	Harvested power
Ambient light		
Indoor	0.1 mW/cm^2	10 μW/cm^2
Outdoor	100 mW/cm^2	10 mW/cm^2
Vibration/motion		
Human	0.5 m @ 1 Hz 1 m/s^2 @ 50 Hz	4 μW/cm^2
Industrial	1 m @ 5 Hz 10 m/s^2 @ 1 kHz	100 μW/cm^2
Thermal energy		
Human	20 mW/cm^2	30 μW/cm^2
Industrial	100 mW/cm^2	1–10 mW/cm^2
RF		
Cell phone	0.3 μW/cm^2	0.1 μW/cm^2

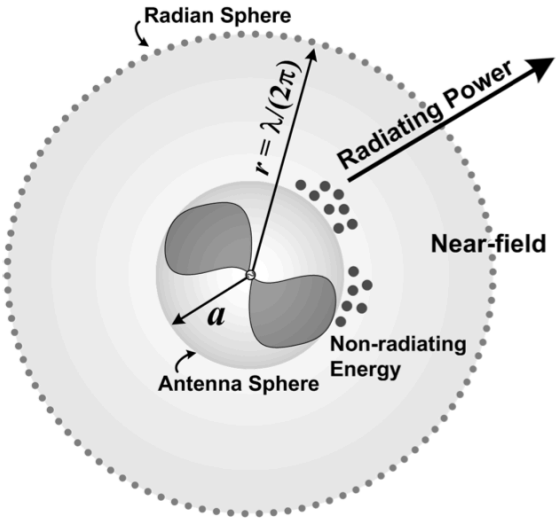

Figure 3.2 The antenna and radian sphere view of an electrically small antenna [60]

Electrically small antennas are known to be inefficient radiators due to the relative magnitudes of the radiation and ohmic loss resistances[55]. It also has been established that for an ESA contained within a given volume, the antenna has an inherent minimum quality factor (Q_a), which places a limit on its attainable impedance bandwidth. For sizes much smaller than design wavelength, Q_a is inversely related to k^3a^3. Thus, the smaller the size, the higher the antenna Q_a, which results in smaller impedance bandwidth and total efficiency[60,61]. Figure 3.2 shows the minimum radiation Q for 100% radiation efficiency versus ka from different literature formulations. Even though it has been shown that the optimal power transfer frequencies for mm sized coils is in the GHz range[62], achieved power transfer efficiencies for mm-sized coils are less than 0.1% [62,63].

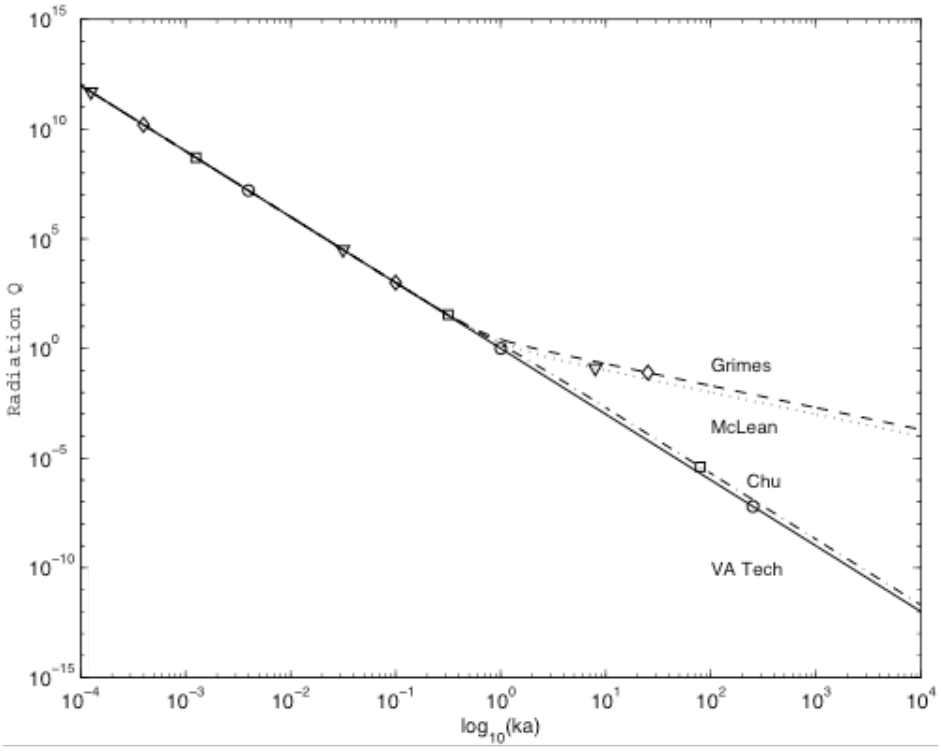

Figure 3.3 Comparison of classical fundamental limits for Q_a [60]

On the other hand, miniaturization limitation of the RF antenna results in a non-monolithic fabrication process for RFID tags that adds inevitable extra expenses to the mass-production

costs of silicon IC. Thus, by replacing RF pathway with a more scalable and monolithically manufacturable alternative, the cost and size of the tags can be tremendously reduced. By using an optical pathway to transmit power and data, the tag can in principle be made much smaller than RFID as LEDs and detectors do not face the fundamental scaling limitation of the RF antenna. This allows not only miniaturization of the tag down to sub-mm range but also reduction of the final cost nearly down to the semiconductor fraction of the finished RFID tag cost. For ease of reference, the name "Universal Basic Identification Tag (UBITag)" is chosen for the envisioned optical tag, which would be referred to through the rest of this script.

The compelling point about UBITag is the potential to miniaturize and mass-produce the generic tag through a monolithic fabrication process. Existing CMOS infrastructure can make high-density and efficient core circuitry for data storage and processing, while CMOS-compatible optical detectors and illumination sources can replace the RF antenna for optical power scavenging and data transmission.

Optical Power Harvesting

For optical detection and power harvesting, research in a variety of fields is directed at extremely low-power, fully functional, autonomous sensing systems powered by photovoltaic devices. For example, Smart Dust was developed to determine the feasibility of packing sensing, computing, and communication into devices on the order of a cubic millimeter for military uses, animal or insect tracking, inventory control, and product quality monitoring. Systems comprised batteries, solar cells, sensors, charge storage capacitors, readout and transmission circuitry, and photodiodes for data reception. In addition, active and passive data transmission was described, the former with a laser diode and beam steering mirror, and the latter with a modulated corner reflector. In 2001, a 63 mm^3 device was reported[64], and

more recently a 16 mm^3 solar-powered node was described, capable of ~12% power conversion efficiency and power outputs of 1.0 mW/mm^2 and 1 $\mu W/mm^2$ in full sunlight and bright indoor light, respectively[65].

Autonomous UBITag systems are conceptually similar to conventional and computational RFIDs (CRFIDs). CRFIDs communicate through backscattering, but also perform sensing, computation, and storage, and then transmit data instead of an identification number. Normally, CRFIDs require continuous RF power from a nearby reader to function, but recently focus has been directed toward making such systems autonomous by incorporating additional power sources. It has been demonstrated that solar energy harvesting can allow for sensing, data storage, and increased RF read range [66–68].

Because only minimal budget power can be harvested from solar energy or indoor illumination sources, photovoltaic powered CMOS systems have mostly been used for sensing applications. But for the UBITag application, with abundant optical power transmitted from an external source with a specifically chosen wavelength to maximize absorption, silicon photovoltaic is a suitable choice to harvest power for the system. They can be either co-fabricated through a mainstream CMOS process[69-76] or post-fabricated on finished circuitry[77-80]. Additional circuitry is necessary when using solar cells as a power source. The output voltage of silicon solar cells ranges from a few tenths of a volt to a maximum of about 0.7 volts under different light levels. Stacking solar cells can provide higher voltages, but to ensure reliable operation, voltage converters and regulators would be necessary. It has been demonstrated that optimal conversion efficiency under different input voltage levels can be achieved through reconfiguration of charge pump circuits [81].

Optical Output

Arguably, integrated optical devices are of great importance for telecommunications and

sensing applications[82,84], as they are used for coupling light sources, optical devices, and detectors with microelectronics[87]. This integration can be accomplished either as a hybrid or monolithically. The hybrid integration requires at least two different substrates bonded together through a careful alignment process, which is in fact the major disadvantage of such a system, as it increases the cost and complexity. On the other hand, in the monolithic integration, all required components can be fabricated directly in the same substrate, thereby eliminating the complex bonding process and reducing the mass-production cost. Although efficient electronics are made chiefly on silicon, research for the fabrication of integrated crystalline light sources in silicon substrates is still developmental, largely because silicon is not an efficient light-emitting material due to its indirect bandgap[85]. One possibility is to integrate incandescent microlamps, which emit a blackbody spectrum of radiation with wavelengths ranging from infrared to visible. They have been reported in a variety of applications such as spectrophotometry; IR signal generation; and calibration of photosensors, pressure sensors, and displays[86-89]. These light sources have been fabricated utilizing polycrystalline silicon and tungsten, among other materials[88,90,91]. Resistive filaments are heated by electric current to incandescent temperatures (400–1200 K) through the Joule effect, and when these filaments are exposed to the atmosphere, oxygen, moisture, and contaminating particles change the filament's emission characteristics and shorten its lifetime[88]. Therefore, vacuum-sealed[92,93] structures have been developed to isolate the filament from the surroundings. The process of fabricating a vacuum-sealed silicon incandescent light is a complicated patented[94] process that yields a pressure-sensitive device, while the silicon oxynitride isolated chromium filament is claimed to have a simpler structure to fabricate and minimal pressure sensitivity[95-97]. Despite interesting applications, integrated incandescent microlamps are not yet known as efficient optical output elements.

With recent progress achieved in organic illumination materials[98], organic light-emitting diodes (OLEDs) seem to present a compelling opportunity to integrate highly efficient light sources with photodetectors onto CMOS substrates, thereby enabling completely integrated optoelectronic applications based on silicon to be realized on one chip. The direct light emission from the OLED enables small devices without additional backlight, making them suitable for sensor and microdisplay applications[7,99-103] and perhaps the most suitable choice for UBITag.

Therefore, by powering the system through a tuned optical source, UBITag can be monolithically fabricated through standard CMOS and OLED technologies, occupying a die area of sub-mm^2 range (Figure 3.4). This can result in reducing the final fabrication cost of a single UBITag as low as that of the semiconductor portion of an overall RFID tag. An autonomous miniature optical chip can be encapsulated in transparent resin spheres with partial reflective coating and attached to any object. Line of sight communication can be interpreted as a favorable feature to increase security, making UBITag less prone to hacking.

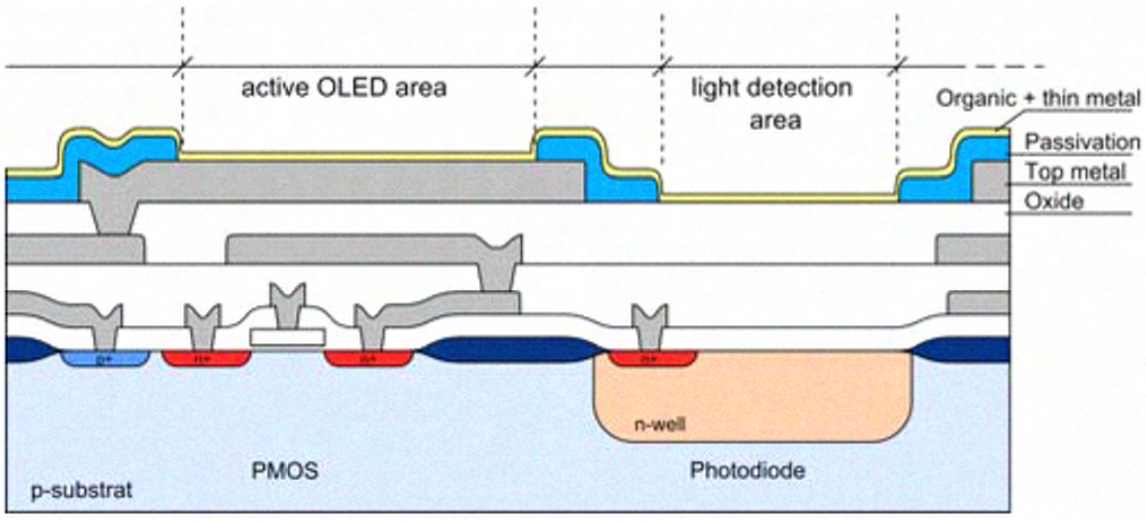

Figure 3.4 Envisioned monolithic UBITag can be fabricated through CMOS and OLED processes[94].

In the rest of this chapter we first describe our effort toward developing a CMOS compatible fabrication process of a polymeric LED, then present our effort to prototype the infrastructure of the UBITag system. In the finl section, we develop a packaging process for encapsulating autonomous optical systems applicable for a miniature UBITag chip.

3.2 Organic Light Emitting Diodes (OLED)

In contrast to inorganic LEDs that require matching crystalline substrate for epitaxial layer growth, organic LED structures can be fabricated on any substrate. They have been co-integrated with CMOS circuitry, especially for microdisplay applications[104-108]. The possibility of monolithic fabrication with the CMOS process makes them suitable for UBITag purposes as well. Therefore as the first step toward realization of a miniature UBITag, we studied the basic physics of organic electroluminescence devices and aimed for developing a CMOS-compatible polymeric OLED at accessible fabrication facilities.

3.2.1 Brief history

Organic electroluminescence (EL) is the electrically driven emission of light from non-crystalline organic materials, which was first observed and extensively studied in the 1960s[109,110]. In 1987, a team at Kodak introduced a double-layer organic light-emitting device (OLED), which combined modern thin film deposition techniques with suitable materials and structure to give moderately low bias voltages and attractive luminance efficiency[111,112]. Shortly afterwards, in 1990, the Cambridge group Friend announced a conducting polymer-based LED[113,114]. Since then, there have been increasing interest and research activities in this field, and enormous progress has been made in improving color gamut, luminance efficiency, and device reliability. The growing interest is largely motivated by the promise of the use of this technology in flat-panel displays. As a consequence, various OLED displays have been

demonstrated. The design of EL materials for used in OLEDs is critical to device performance. Great strides have been made towards the development and improvement of molecular materials for display applications. Intense research in both academia and industry over the past two decades has yielded OLEDs with remarkable color fidelity, device efficiencies, and operational stability, competing the crystalline counterpart. A comparison of the efficiencies of several different display and light sources is shown in Figure 3.5, and progress in LED efficiencies over the last few decades is summarized in Figure 3.6.

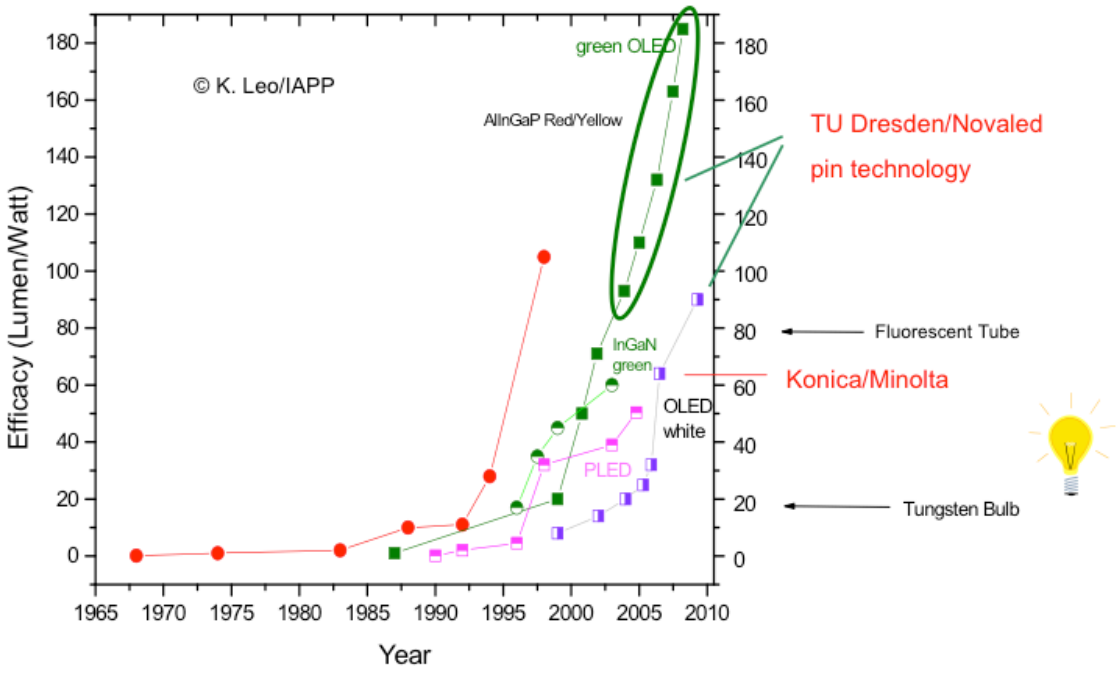

Figure 3.5 Progress in various lighting and display source efficiencies over the past few decades. Copyright K. Leo/IAPP.

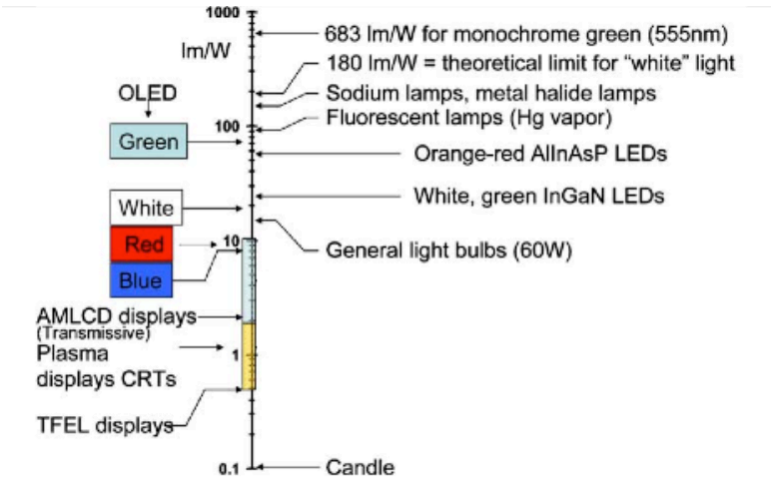

Figure 3.6 Comparison of the luminance efficiencies of several different lighting and display sources. Figure courtesy of C.W. Tang, Kodak, Inc[115].

3.2.2 Basics

An OLED has an organic EL medium consisting of extremely thin layers sandwiched by two electrodes (Figure 3.7 a).

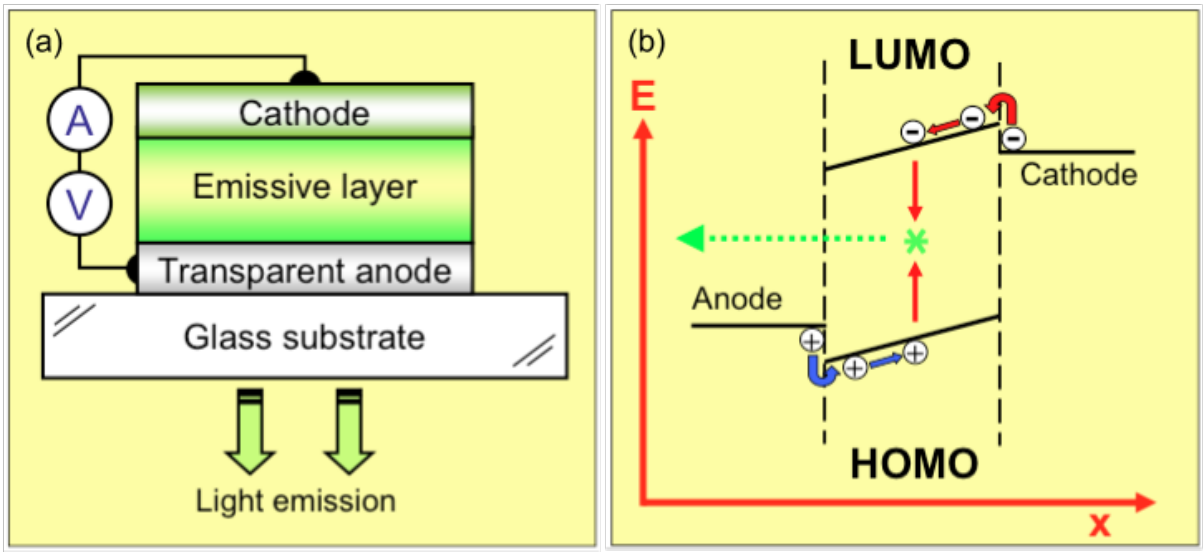

Figure 3.7 a) An OLED is a special amorphous material sandwiched between two electrodes, b) Band diagram under forward bias illustrating the charge injection, transport, and recombination processes. LUMO and HOMO are analogous to conduction and valence bands of semiconductors.

OLEDs are constructed using glassy and amorphous organic molecules or polymer films and thus provide significant advantages in device fabrication and cost reduction. They are

markedly different in structure from inorganic LEDs consisting of epitaxial semiconductor thin films, and the mechanism governing their operation is also quite different from that of a crystalline semiconductor-based LED. The origin of the semiconducting nature of these materials must be described using the molecular orbital theory rather than the semiconductor band theory, which is beyond the scope of this dissertation. Despite the fundamental differences in the formalism required in describing the origin of semiconductivity in crystalline inorganics and polymers, significant analogies exist in their fundamental behavior. The terms HOMO (highest occupied molecular orbital) and LUMO (lowest unoccupied molecular orbital) are introduced in the organic illumination concept and become analogous to the top of the valence band and the bottom of the conduction band, respectively[116] (Figure 3.7 b). In a basic two-layer OLED structure, one organic layer is specifically chosen to transport holes and the other organic layer is specifically chosen to transport electrons. The interface between the two layers provides an efficient site for the recombination of the injected hole–electron pair and resultant electroluminescence.

When an electrical potential difference is applied between the anode and the cathode such that the anode is at a more positive electrical potential with respect to the cathode, injection of holes occurs from the anode into the hole-transport layer (HTL), while electrons are injected from the cathode into the electron-transport layer (ETL). The injected holes and electrons each migrate toward the oppositely charged electrode, and the recombination of electrons and holes occurs near the junction in the luminescent ETL. Upon recombination, energy is released as light, which is emitted from the light-transmissive anode and substrate.

The heterojunction should be designed to facilitate hole-injection from the HTL into the ETL and to block electron injection in the opposite direction in order to enhance the probability of exciton formation and recombination near the interface region. As shown in Figure 3.8a, the highest occupied molecular orbital (HOMO) of the HTL is slightly above that of the ETL, so

that holes can readily enter into the ETL, while the lowest unoccupied molecular orbital (LUMO) of the ETL is significantly below that of the HTL, so that electrons are confined in the ETL. The low hole mobility in the ETL causes a buildup in hole density, thereby enhancing the collision capture process. Furthermore, by spacing this interface at a sufficient distance from the contact, the probability of quenching near the metallic surface is greatly reduced.

The simple structure can be modified to a three-layer structure, in which an additional luminescent layer is introduced between the HTL and ETL to function primarily as the site for hole–electron recombination and thus electroluminescence. In this respect, the functions of the individual organic layers are distinct and can therefore be optimized independently. Thus, the luminescent or recombination layer can be chosen to have a desirable EL color as well as a high luminance efficiency. Likewise, the ETL and HTL can be optimized primarily for the carrier-transport property.

The extremely thin organic EL medium offers reduced resistance, permitting higher current densities for a given level of electrical bias voltage. Since light emission is directly related to current density through the organic EL medium, the thin layers coupled with increased charge injection and transport efficiencies have allowed acceptable light emission to be achieved at low voltages.

3.2.3 Standard Fabrication processes

Molecular OLED

Vacuum evaporation by resistive heating is most appropriate for depositing molecular materials. Organic vapor phase deposition (OVPD) has also been demonstrated to deposit organic materials on large substrates[120]. It is also common to deposit cathode materials using the same vacuum evaporation from filaments. For the deposition of high-temperature metals,

one may employ e-beam evaporation or sputtering. The latter is particularly useful for large substrates and high throughput production. However, because OLEDs are extremely sensitive to radiation, special care needs to be taken. For example in e-beam deposition, a magnetic field is applied across the substrate to repel electrons and ions. In sputter deposition, a buffer layer is required to minimize the radiation damage inflicted on the OLED organic layer stack. Typical molecular base bottom emitting device fabrication occurs by the following sequence: devices are grown on glass slides pre-coated with transparent ITO. Substrates are ultrasonically cleaned in detergent solution, followed by thorough rinsing in DI water. They are then cleaned in organic solvents and dried in pure nitrogen gas. After cleaning, the ITO glass is subject to an oxygen treatment using either UV ozone or oxygen plasma to enhance hole-injection. Single heterostructure devices (Figure 3.8 b) are formed by sequential high vacuum (10-5 to 10-6 Torr) vapor deposition of a hole-transport layer such as NPB, followed by an electron-transport layer of Alq3, previously purified by temperature gradient sublimation. Deposition is carried out by thermal evaporation from a baffled Ta crucible at a nominal deposition rate of 0.2–0.4 nm/s. An electron-injecting electrode of approximately 10:1 Mg:Ag volume ratio is subsequently deposited by co-evaporation from separate Ta boats at a vacuum of 10-5 Torr in the same chamber. The device preparation is completed with encapsulation in a dry argon box[118].

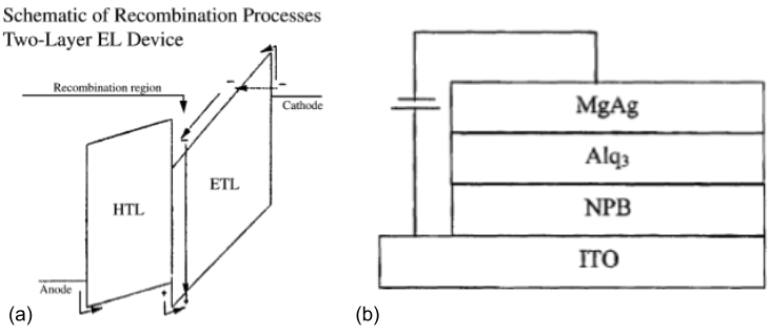

Figure 3.8 a) Energy level diagram of a two-layer OLED. b) Common electron and hole-transport materials and a two-layer OLED [117].

Polymeric OLED

The generic fabrication process can be described as follows: a layer of PEDOT-PSS is spin cast onto an ITO patterned glass substrate to function as the device's anode. The polymer layer is then spin cast above, and finally a layer of calcium followed by aluminum is thermally evaporated to serve as the cathode. The function of the PEDOT-PSS is twofold; it assists in hole injection into the device and creates a smooth even surface on which to spin the polymer film. The calcium functions as the effective cathode of the device; an evaporated layer of aluminum is added to the process to help shield the calcium against oxidation. A typical energy level / work function diagram for such a device is given in Figure 3.9[107].

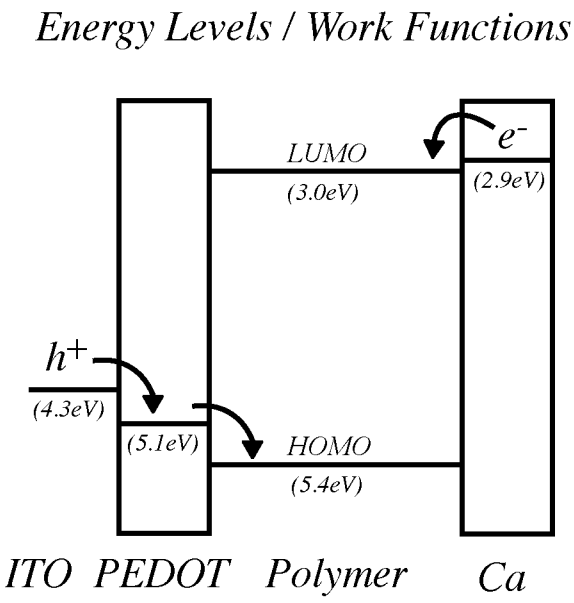

Figure 3.9 An sample energy level / work function diagram for a PLED[116]. The HOMO/LUMO levels for the polymer shown are that of MEH-PPV[125-126]. In this example, no barrier exists for electron injection.

The schematic diagram of this type of device structure in forward bias is similar to Figure 3.7b. Electrons from the cathode are injected into the LUMO of the polymer on one end of the device, and holes are injected from the anode into the polymer HOMO on the other. The charge carriers recombine within the polymer layer and emit light. Charge injection, one of the main processes affecting the operation of the device, is characterized primarily by the difference between the electrode work function and the polymer HOMO/LUMO levels.

3.2.4 Single layer Polymeric OLED process development

As the OLED structure would eventually be fabricated on a finished CMOS wafer, conventional silicon substrate with a previously grown oxide layer was used for process development. To continue developing the process, we had to select between molecular and polymeric OLED types. Despite better a chance for higher optical efficiency of molecular OLEDs, no accessible fabrication facility was equipped with a proper deposition chamber. Therefore, we decided to develop a process for polymeric OLEDs (PLED). The general structure of a bottom-emitting PLED was previously described. Despite significant structural

similarity between bottom- and top-emitting devices, the steps required in post-fabricating them on finished CMOS wafers occur in reverse order. For top-emitting devices, the first step is to select the electroluminescence layer – in our case, Poly[2-methoxy-5-(2-ethylhexyloxy)-1,4-phenylenevinylene] (MEH-PPV), the most commonly studied soluble light-emitting polymer[116,119-125]. LUMO and HOMO levels of MEH-PPV located at 3.0eV 5.4eV respectively[126] would guide us toward proper material selection to minimize the injection barrier. The conductor most suitable for minimizing the potential barrier at Metal-Polymer interface would be Ca with work function of 2.9eV, while the most popular transparent conductor, ITO, has work function of 4.3e.V-4.7eV.

Depositing Ca requires a thermal deposition chamber (in contrast to E-beam evaporation), but the accessible microfabrication facility was not equipped with one. Therefore the practical solution was to choose Mg as the cathode, since it could be deposited using an E-beam evaporation chamber and has a low work function of 3.7eV. Starting with a 4" silicon wafer carrying pre-grown oxide (Figure 3.10 a), we first deposited the cathode layer through lift-off (Figure 3.10 b). A negative photoresist, nr7-1000, was spun and patterned through photolithography. A cathode layer comprising Al:120nm-Mg:30nm was deposited through E-beam evaporation. Al was used as the main conductor, while the thin Mg layer minimized the potential barrier at the Metal/Organic layer boundary. Eventually the last Al layer of CMOS process would be used as the cathode.

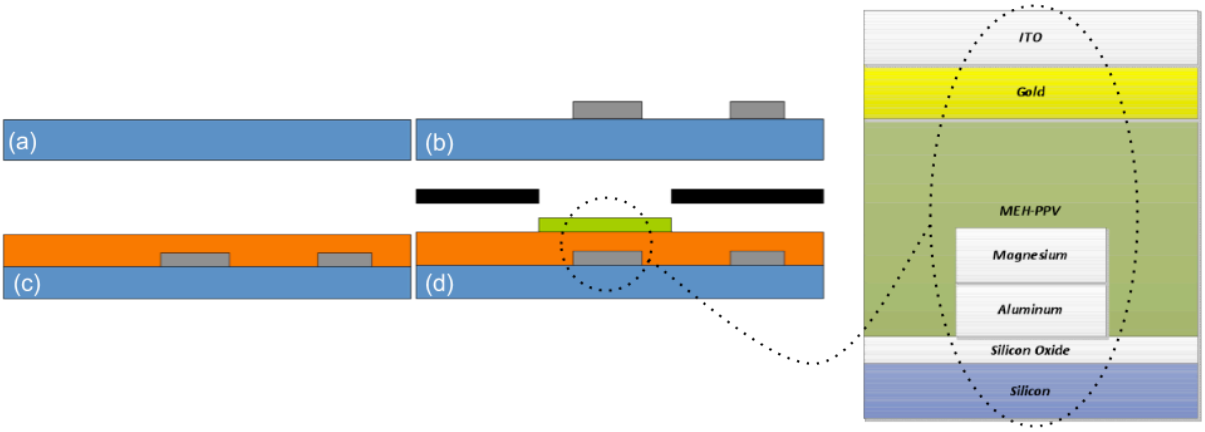

Figure 3.10 a) Silicon wafer with pre-grown oxide, b) Al/Mg layer deposited and patterned through lift-off, c) MEH-PPV solution spun and vacuum dried, d) Anode layer deposited through shadow mask.

To deposit a uniform organic layer, polymer material would be dissolved in a solvent and the solution is spun on the wafer in an inert ambient to prevent oxidation of organic material. Wafer would be left under vacuum to remove the solvent overnight. MEH-PPV solutions 0.8 wt % of polymer to weight of p-Xylene were stirred for a minimum of 48 h at 50 °C. Not having access to a glove-box, the solution was spun on the wafer in air ambient and put under lab-vacuum overnight to remove the solvent (Figure 3.10 c). The nominal process mentioned a PEDOT:PSS layer between ITO and the polymer, which is spun and dried prior to polymer layer spin casting. The presence in the PEDOT:PSS solution of water, which could oxidize the polymer, prevented us from using this material in our structure. So we completed our structure by depositing the anode layer through a shadow mask (Figure 3.10 d). For the anode we ran several tests. The first test was to use ITO through sputtering. Having only ITO as the anode at the polymer interface introduces a large potential barrier (~1.1eV), which results in a high turn on voltage for the device, ~5V (Figure 3.11, series1). In order to reduce the electrical barrier, thus decreasing the turn-on voltage, we evaporated a very thin gold layer (10nm : ~70% transparent) prior to sputtering ITO layer (Figure 3.11, series 3). This introduces the Au work function (5.1eV) as an intermediate energy level between ITO's work

function (4.3eV) and the polymer's HOMO (5.4eV). As a result the turn-on voltage reduced considerably to ~3V. We also tried to deposit the thin gold layer and ITO by sputtering, but the final devices did not act as diode and never turned on (Figure 3.11, series 4). We suspect that the polymer layer had been damaged during sputtering gold and created short connections between anode and cathode. Devices with solely a thin Au layer were laterally broken at high electric fields (Figure 3.11, series 2).

Despite low optical output, the spectrum of the LED from the batch with the Au/ITO anode was measured using an integration sphere (Ocean Optics FOIS) with peak wavelength at ~580nm (Figure 3.12). A sample illuminating OLED is shown in Figure 3.13.

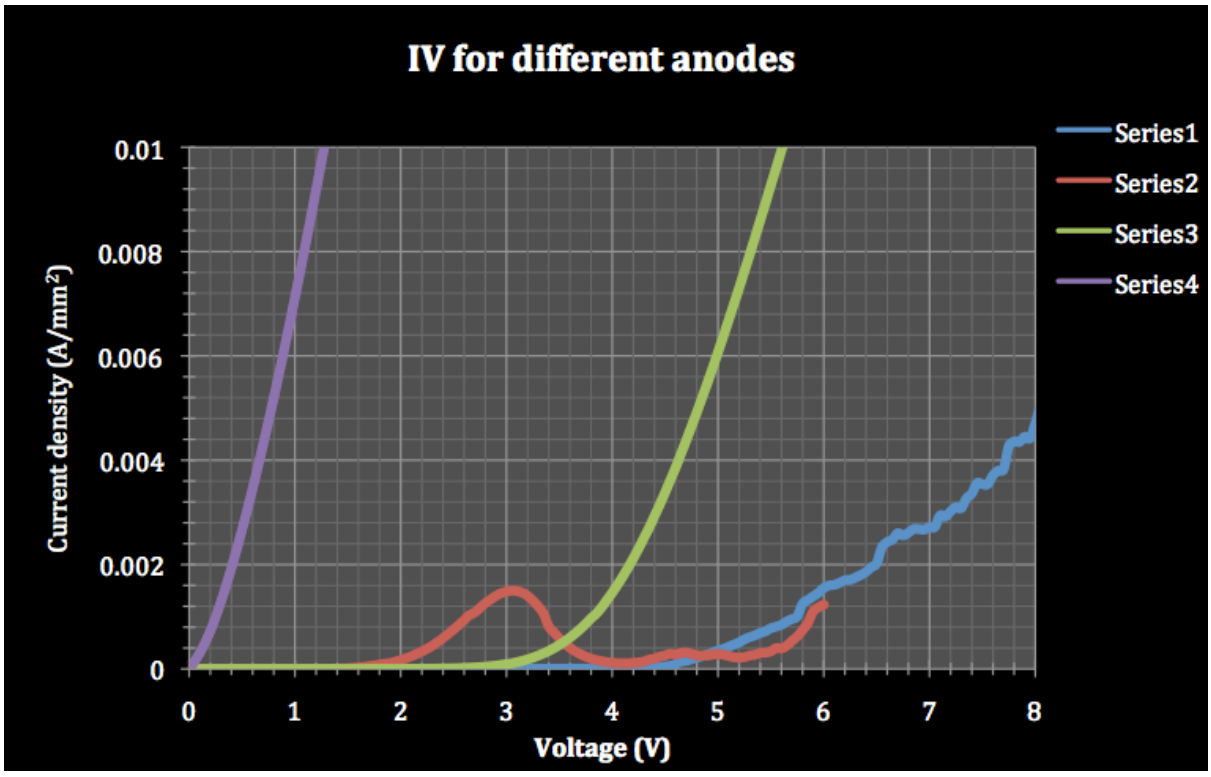

Figure 3.11 IV characteristic of OLED with different anodes: series1) ITO only, series2) 7nm Au only, series3) Evaprated 7nm Au/ Sputtered ITO, series4) Au/ITO sputtered

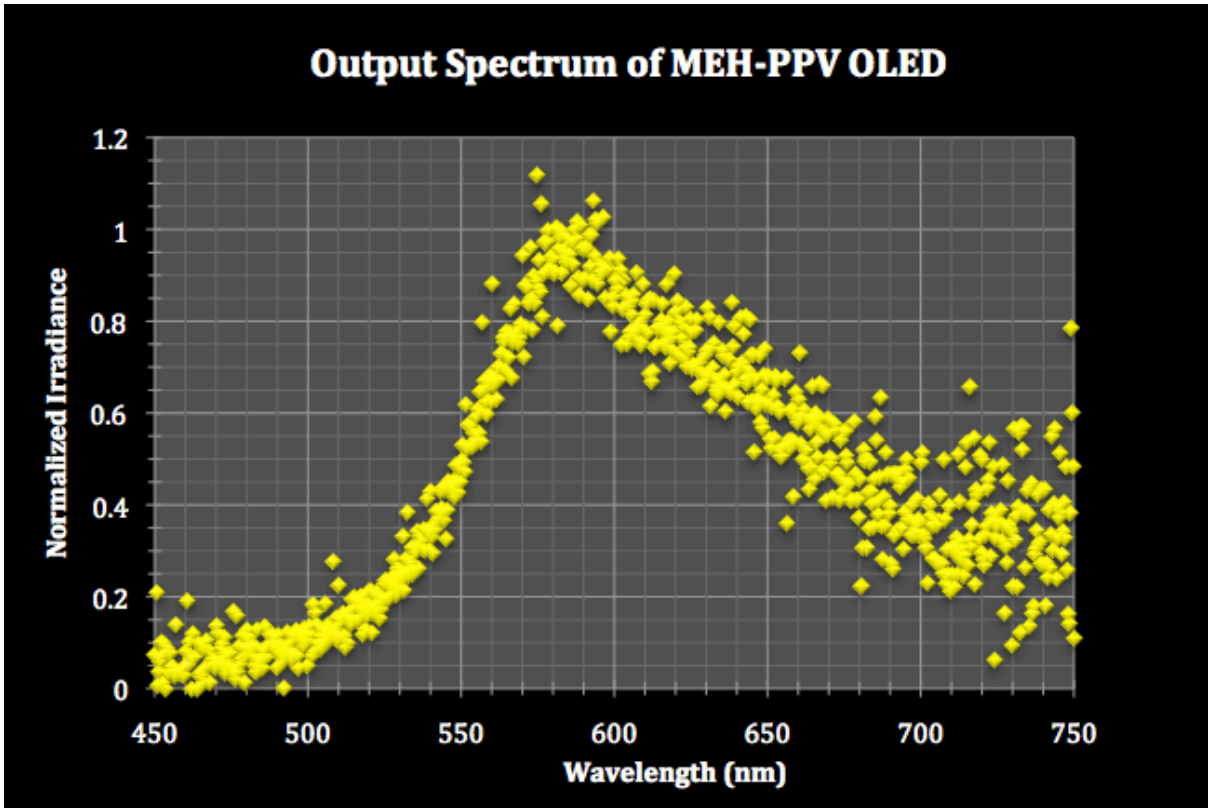

Figure 3.12 Optical Spectrum of MEH-PPV OLED with peak at 580nm.

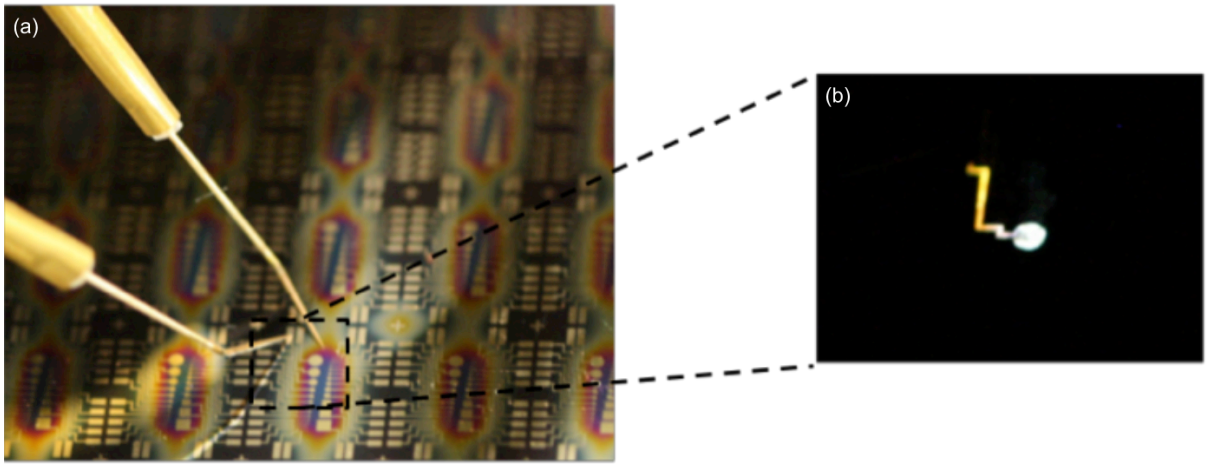

Figure 3.13 a) Fabricated OLED tested with probestation, b) Sample illuminating OLED.

3.3 Prototyping UBITag system infrastructure

For a miniature monolithic Tag, OLEDs are the best way to implement the optical output of the system, but as described previously, we are not equipped with a proper equipment to deposit organic materials nor to fabricate efficient PV cells at accessible facilities. Nonetheless, the scope of the entire tag system design – comprising silicon-integrated circuit and optoelectronics, organic luminescence design, packaging, and software layers development – is beyond a single PhD. Therefore, to illustrate the concept of UBITag, we decided to demonstrate the system infrastructure through prototyping using off-the-shelf components. Furthermore, despite the impossibility of monolithic miniature tag fabrication at available facilities, we developed a packaging process for encapsulating the miniature autonomous optical tag to take a small step toward making UBITag system a reality.

As previously illustrated, the envisioned UBITag system infrastructure comprises a miniature tag capable of storing a unique ID, a Reader to assign and readout ID from the Tag, a cloud database to store complementary information regarding the ID, and a user frontend on a conventional mobile device (Smart phone) to interact with the cloud database and control the Reader (Figure 3.1)

Tag

The autonomous tag system is envisioned to be powered and communicate data through optical path. Therefore, the miniature tag system consists of three main sub-systems:

- Optical reception system: To transmute incident optical beam to electrical signal.
- Integrated circuit: To store, process, and transmit information, and to manage power.
-Optical output: To communicate data with external systems using coded optical communication in free space.

Reader

The Reader is the link between the user frontend and the tag. The Reader's interfacing can be divided into 2 main categories:

-Reader interaction with user frontend**:** depending on the user's command via a communication thread, the Reader receives and stores the new ID for eventual assignment to a tag or report a recently read-out ID from a tag to the UI for further database investigation.

-Reader interaction with tag: again depending on the command, it initiates an optical link for enabling power for and data communication with the tag, assigns a new ID or read-out, and stores the previously written ID from the tag.

Cloud database

A global database is necessary for storing the tag IDs and the definition of the objects they represent. The database would need to be updated prior to every new ID assignment.

User Interface

Apparently an interface is needed for the user to enter or display data. More descriptively the user frontend is needed for entering new ID and definition, checking and updating the cloud database, assigning the legitimate new ID to the Reader or receiving the recently read-out ID from the Reader, and looking up and displaying the read-out ID definition from the database.

To demonstrate the system infrastructure we should design and manufacture the hardware for the tag and the Reader, implement the proper firmware, develop a web database to store tag ID and other information, and develop a mobile device software application to control Reader actions and interact with the database. Prototyping procedure can be broken down into two major sections: hardware and software.

3.4.1 Hardware

To minimize the circuit design complexities of our prototype, microcontroller units (MCU) are utilized as the core circuitry of both tag and Reader hardware to benefit from the data storage, processing, and communication features with which they are equipped.

3.4.1.1 Tag

Considering MCU as the data storage and processing block, the Optical tag system comprises 4 main subsystems (Figure 3.14):

- Data storage and processing unit (MCU)
- Input data detection
- Power harvesting
- Optical output

Input data detection:

In the UBITag introductory section we envisioned using modulated single wavelength beam conveying power and data from Reader to Tag. It would be the Tag's custom circuitry task to harvest the power and retrieve data from the photogenerated current created by the incident beam. This introduces some circuit design challenges for prototyping using off-the-shelf components. To minimize complexity, we resolve this issue through optical filtering, transferring power and launching data from the Reader utilizing different wavelengths: a visible wavelength DC stream to supply power and an infrared modulated stream for data transmission. In this way the visible DC stream can be blocked by optical filtering previously mounted on a photodetection block.

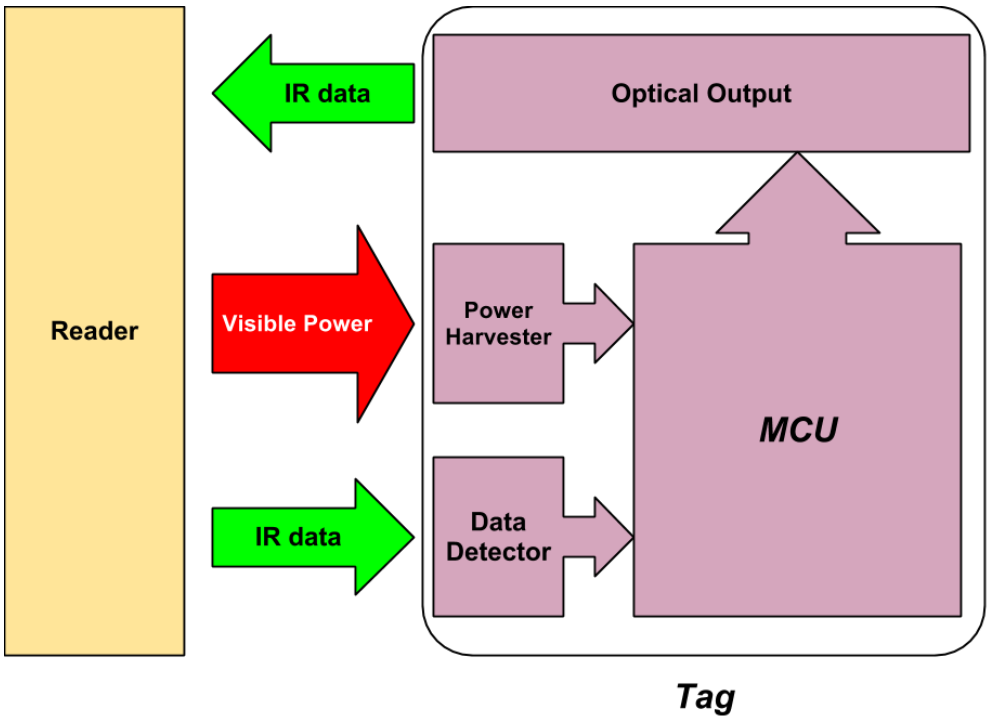

Figure 3.14 Block diagram of tag

A data detection block can be assembled using an Ir-PIN diode (Si PIN diode mounted with infrared band-pass filter) to transmute input infrared data to a photocurrent and transform that to voltage logic level by a transimpedance amplifier. A logic inversion to the input signal can be introduced, depending on the PIN diode orientation, which we will further discuss below (Figure 3.15).

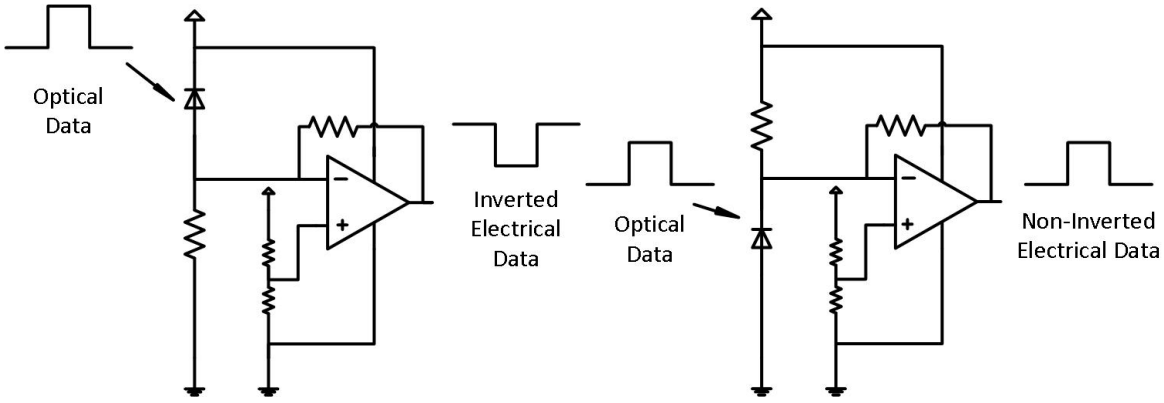

Figure 3.15 Optical data detection circuit schematic with and without logic inversion

Power harvesting:

As noted above, power is supplied through a DC visible stream launching from the Reader, so an optical-electrical transducer is required for harvesting. Aiming for CMOS-compatible

processes, we utilized silicon PV cells for prototyping. The proper supply voltage level for the system can be obtained either by serially connecting multiple PV cells or by boosting the output of a single cell. Due to additional power conversion loss of commercially available boost converters and extra circuit complexity, we decided to provide the source voltage level of the tag system through serial connection of multiple silicon PV cells. The minimum supply voltage of tag components will define the number of single cells required to be serially connected, while required surface area depends on tag total power consumption, available optical power from Reader and PV cell conversion efficiency.

Memory/DSP Unit:

As previously mentioned, conventional microcontroller units can take care of data storage and processing; they can also equip us with a choice of various communication ports and protocols that can be used to establish a connection between the tag and the Reader.

Optical Output:

Although organic LEDs would be the proper choice for UBITag's optical output block due to their CMOS-compatible fabrication process, in contrast to crystalline LEDs, they are not commercially available for indication purposes. Therefore we had to use inorganic LEDs for the Tag's optical output to communicate with Reader. To ensure continuous presence of a visible DC stream during every Tag-Reader communication cycle, we anticipated needing an AC-DC photocurrent separation block on the Reader system in case of utilizing visible wavelength LED as Tag's optical output. This issue can be resolved by using an infrared stream for data transmission from the tag and using optical filtering for the Reader system.

Among several goals we are seeking by prototyping UBITag's infrastructure, a major one is to make a functional tag, harvesting power by a small PV area, because that would be the main limiting factor to miniaturizing the ultimate tag chip. Therefore we tried to find and

utilize miniature, commercially available PV cell arrays with an output voltage range of 2-3.6V (standard low voltage supply level), but the smallest PV array we could access commercially had an active area of ~8mm^2 and an open circuit output voltage of 4V, which was overqualified for both perspectives. So to provide the proper voltage supply we decided to reach the desired level by serial connection of multiple PV cells. As previously mentioned, despite the fact that miniature PV cells were not available on the market, we were able to find another CMOS-compatible component in more miniature packaging available on the market: silicon PIN diodes. With Voc ranging between 0.4-0.6V for a single PIN junction, serial connection of 4 Si PIN diodes would provide a Voc level larger than 2V (the minimum supply voltage for our tag system design). Linear relation of photogenerated current with surface area made us test several PIN diodes with various surface areas ranging from 7mm^2 to 0.36mm^2. Aiming for a total current consumption of less than 500uA, the serial connection of 4 PIN diodes with 0.36mm^2 surface area could convert enough input optical power stream to electricity. As different wavelengths are used for data and power transmission, a miniature packaged PIN diode with mounted visible wavelength filter was used to block the power stream and detect infrared input data. To assemble a circuit with minimal power consumption, components were selected from available power-efficient products. The main consumers on the tag circuit are the microcontroller unit, the transimpedance amplifier of the data detection block, and the infrared LED for data transmission. A thorough search on the market for low-power MCUs led us to the MSP430FR57xx family (Appendix C) from Texas Instruments, which have a 2V-3.6V supply voltage range and 81 μA/MHz current consumption during Active mode. Available in a 4mm×4mm PVQFN-N24 packaging, MSP430FR5738 was chosen as the Tag's main processing unit. To convert the photogenerated current from the input Ir-PIN diode (TEMD7100, Figure 3.19b) into proper voltage form, we utilized MIC863 as our transimpedance amplifier. MIC863 was chosen due

to its low quiescent current consumption (<5 uA) and wide voltage supply range (2V-5.25V). An infrared LED with miniature packaging was selected as the optical output of the tag (SFH4050). A schematic of the tag prototype is shown in Figure 3.16.

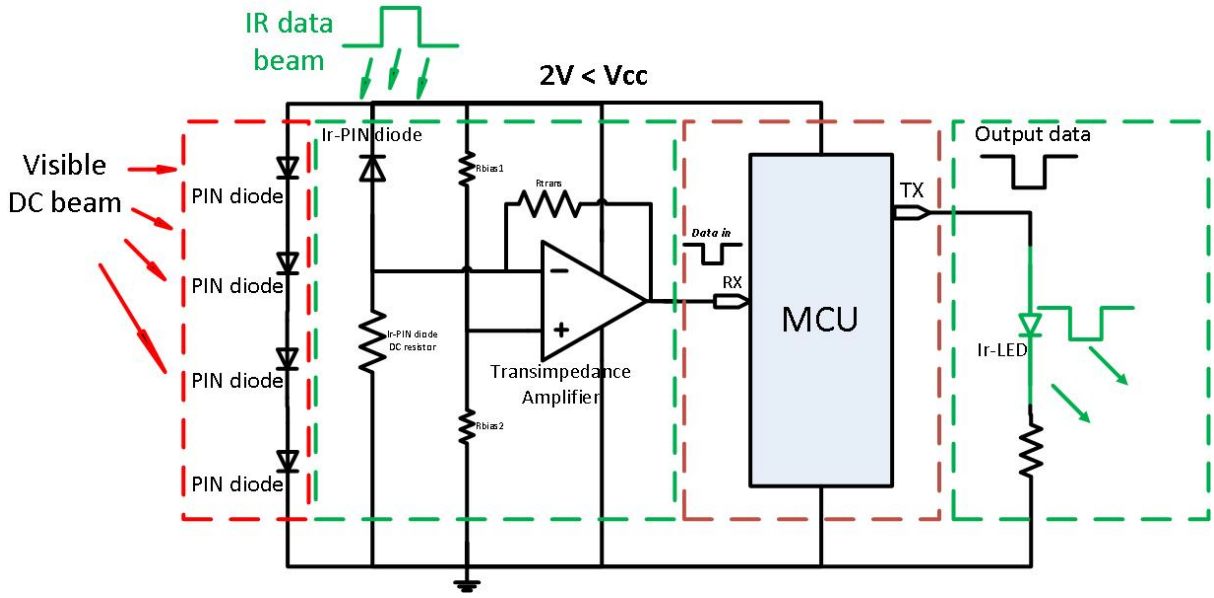

Figure 3.16 Schematic of tag prototype circuit

Utilizing the miniature-size and low-power components available, the Tag's printed circuit board (PCB) was designed using EagleCAD software with optoelectronic components mounted on one side and electronics on the other (Figure 3.17).

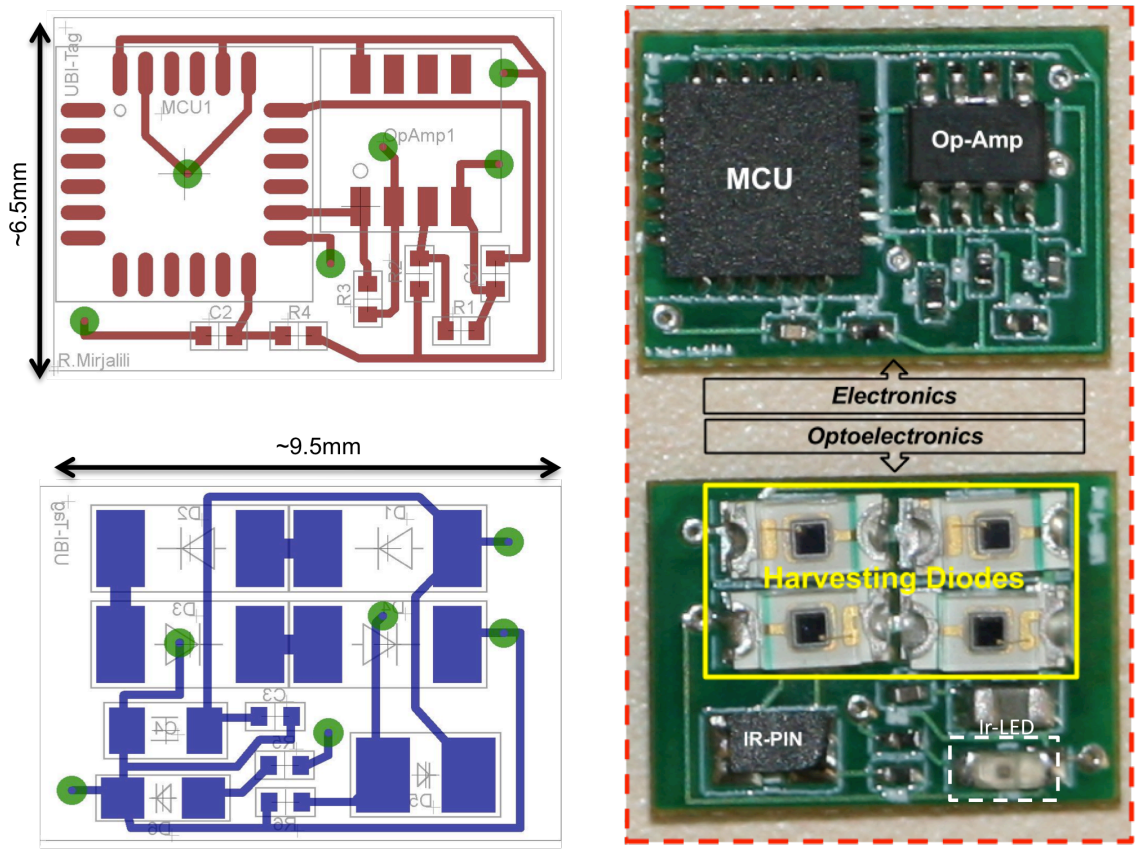

Figure 3.17 Tag, prototyped PCB board

3.4.1.2 Reader

The Reader system should be capable of interacting with the tag and a handheld device such as cell phone or tablet that controls Reader actions through an Application. Communication and power supply to the tag will be through an optical path, thus there would be some analogy between a couple of Reader sub-blocks and Tag's such as: *Data storage and processing unit (MCU), Infrared data detection* and *Infrared output*. An additional block among Reader optical subsystems compared to the tag is a *visible wavelength optical output* that supplies power for the Tag. The Reader would also be controlled by the mobile device for data readout/retrieval or new data assignment, through a standard communication thread such as *Universal Serial Bus (USB)* or *Bluetooth* (Figure 3.18).

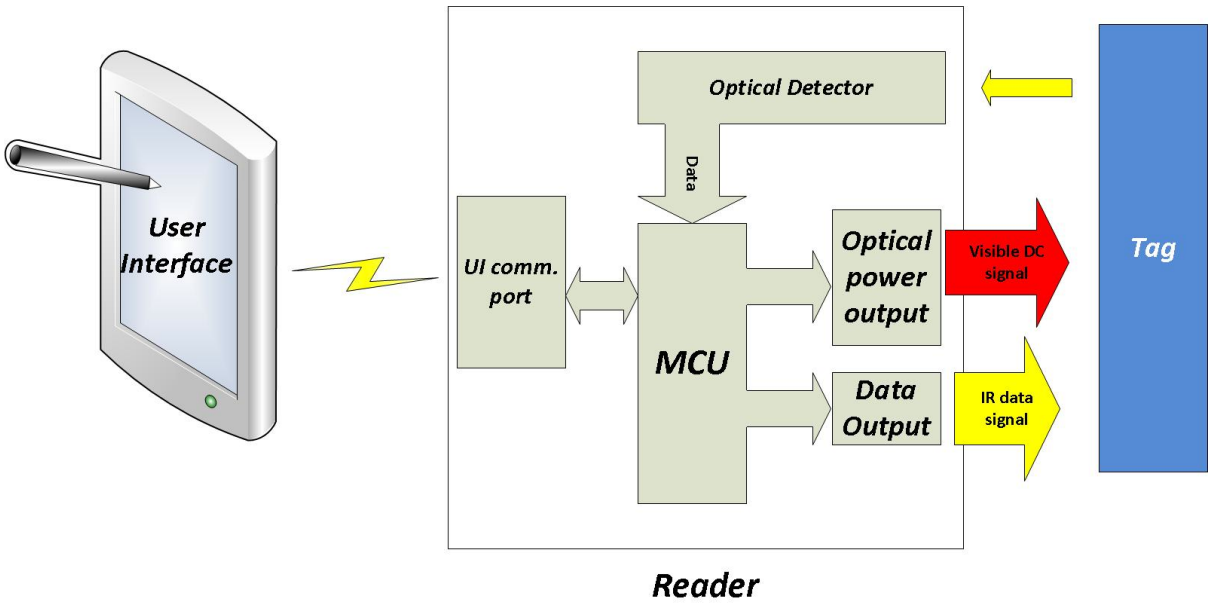

Figure 3.18 Reader block diagram

Optical data detection:

The most challenging block to design for the Reader is the detection circuit. Because of the low amount of power available for the tag from optical conversion, the amount of power dedicated to the output LED will be low (I_{LED} < 300uA). Therefore, the Tag's wide-angle optical output (SFH 4050 with 130 deg illumination angle) will be comparable to the leakage current resulting from the DC powering stream passing the PIN diode's optical filter. Hence the Reader's data detector has to be more sensitive than the Tag's. One way to improve sensitivity is to increase the detection area, thus a PIN diode with a 7mm^2 active area mounted with an optical filter has been used. The second step would be to amplify the output of the transimpedance stage. This step would also invert the output of the data detection block; depending to PIN diode orientation, data can retain its correct logic form (Figure 3.20)

Optical power source for Tag:

Considering the absorption diagram of PIN diodes on the Tag's power harvesting (Figure 3.19a) and data detection blocks (Figure 3.19b) demonstrates that the closer the powering wavelength to the edge of the optical filter (650nm) and harvesting peak (800nm), the higher

the conversion efficiency. Therefore, an optical source with peak wavelength smaller than but as close to 650nm would be more efficient.

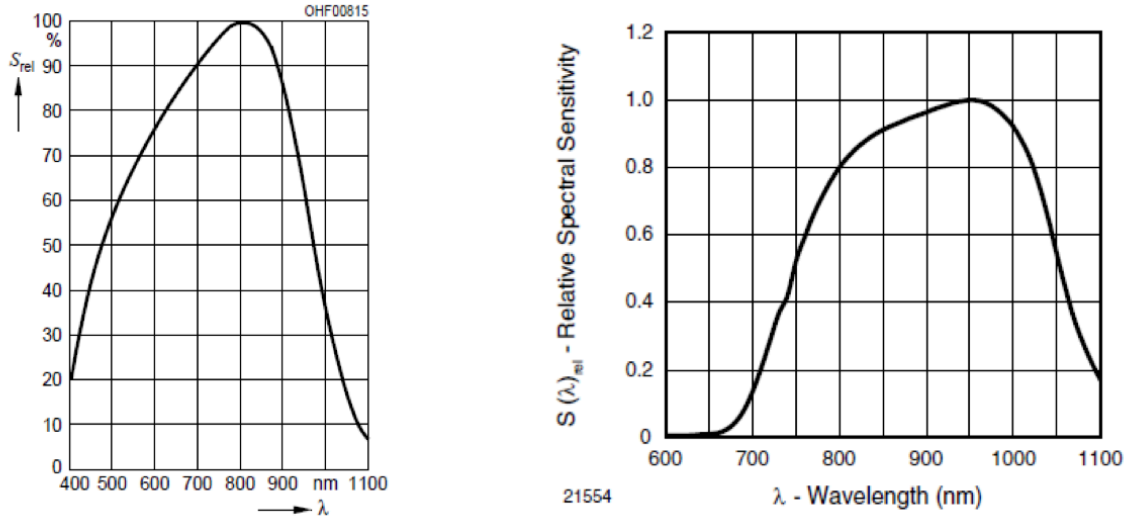

Figure 3.19 a) Spectral sensitivity of harvesting PIN diodes (SFH2701), b) Spectral sensitivity of detecting PIN diodes (TEMD7100)

As for the source to supply optical power for the Tag, two options could be considered:

-Lasers

-Bright LEDs

The first issue with lasers is that they require complex optics for beam expansion to cover the Tag's optical surface (18mm^2 for final tag board). Another issue is that they are not widely available in small packaging (SMD) for the visible wavelengths spectrum. Therefore we proceeded to the second option and looked into bright, visible LEDs. The main downside of bright LEDs is their wide angle of illumination, which limits the maximum distance between tag and Reader for sufficient power transfer—something that was not a major concern for prototyping purposes. Therefore a bright LED with nominal peak wavelength of 645nm was chosen to supply power for the Tag. Serial connection of multiple PIN cells on the tag system dictates the necessity of equal optical power illumination on every cell in order to maximize conversion efficiency. Otherwise extra photogenerated carriers in each individual cell would

recombine, and the output current of the array would be limited to the cell with the minimum photogenerated current. Therefore assembling the harvesting PIN diodes on the tag with minimal spatial distance can increase the chance of equal incident optical power from Reader to Tag. To increase this chance, we used 2 bright LEDs serially on the Reader because of the PIN diodes' orientation on the Tag. These issues would have been minimal if PV cells were fabricated monolithically, rather than as individual assemblies. Thus 2 bright LEDs and a current limiting resistor are serially connected; they would be turned on by activating an NMOS switch controlled by MCU (Figure 3.20).

The final step to complete the optical side of the Reader is assembling and driving infrared LED for data transmission. Direct connection of the LED to MCU's transmission pin (Tx), as with the Tag, presented an issue. The Tx pin of MCU is set to a high level by default during idle mode (when no data is transmitting from this port, i.e. the Reader is not sending but receiving the Tag's relatively low intensity response). Therefore if the LED is connected directly, a relatively high intensity infrared stream would illuminate, conveying zero information, which cannot be filtered optically by the Reader's PIN diode filter, thereby making it almost impossible to detect the Tag's relatively low intensity response. To resolve this issue, a PMOS switch was added to let the current pass from the LED only during transmission periods. This in turn would add a logic inversion to the data transmitted optically to the Tag. Therefore, the Tag's detection circuit was designed so as to add another inversion to the incoming data, thereby attaining the correct logic (Figure 3.20).

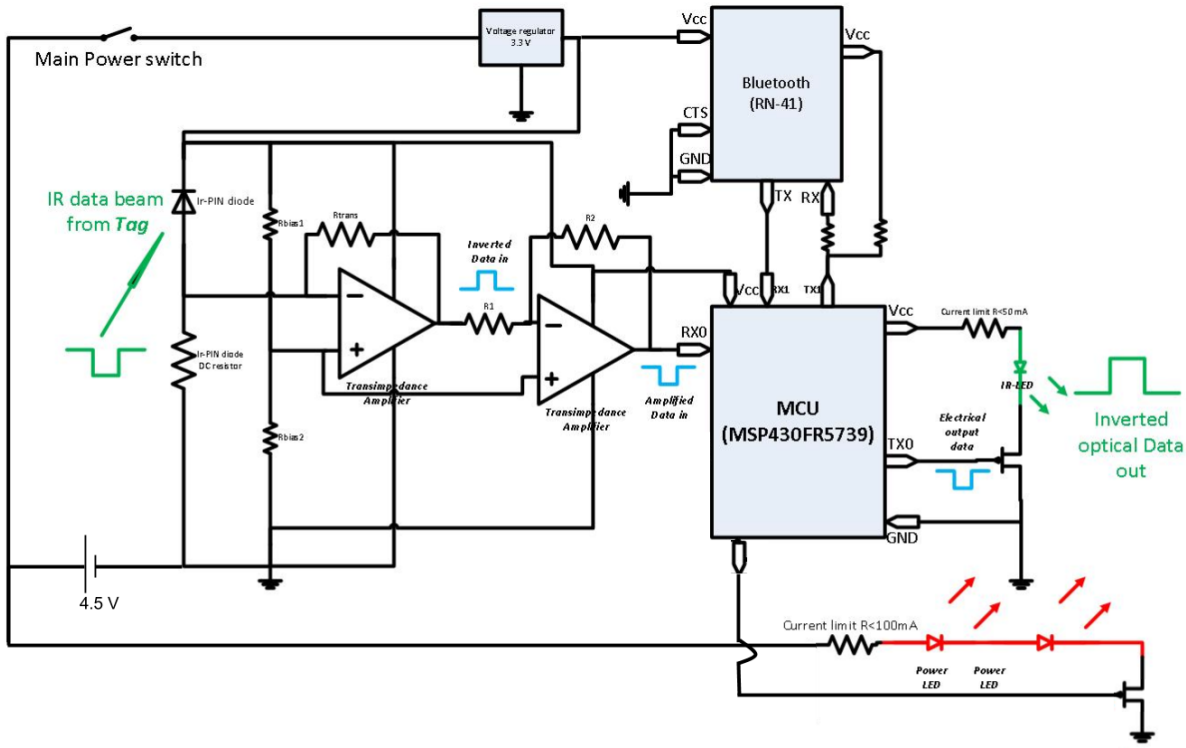

Figure 3.20 Reader optical data detector and driver

To complete the Reader's hardware, a suitable mechanism for data transmission between handheld device and Reader need to be implemented. Since one of today's most frequently used devices is the Smartphone, we decided to develop the user interface for controlling the Reader's actions on the Android platform. Data transfer could be accomplished through two conventional methods: Universal Serial Bus (USB) or Bluetooth. Using USB presented two problems. First, we found that the way that Android OS interfaces with USB, called Android Open Accessory Mode, only allows for connecting peripherals to an Android platform where the Android is the USB device and the peripheral (accessory) is the USB host, which is the complete reverse of a conventional interconnect. This issue introduced so many complexities to the design of both our hardware and our software that we suspected the USB option might not be worth the time and effort needed to resolve them. Seeking advice from available resources and from field experts, including CSE professor G. Borriello, we realized that creating a Bluetooth connection with Android is a well-established feature and less

troublesome than USB. Hardware design complexity was also minimal in directly connecting the Reader's MCU serial ports (MSP430FR5739) to a Bluetooth device (RN-41). Utilizing 2 LED junctions in series passing relatively high current requires a supply level of larger that 3V, which we reached by powering the Reader circuit by 3 serially connected AAA batteries. A 3.3V voltage regulator is utilized to provide the standard supply level for the rest of the Reader circuit (MCU, Bluetooth and Op-Amp). We custom-designed and manufactured a printed circuit board for the Reader with optoelectronics and electronics on one side and 3 AAA batteries on the other side (Figure 3.21). The board has a single physical switch for activation while it is fully controlled by Android Application via Bluetooth. A custom-designed box was 3D-printed to conceal the main part of the board (Figure 3.22)

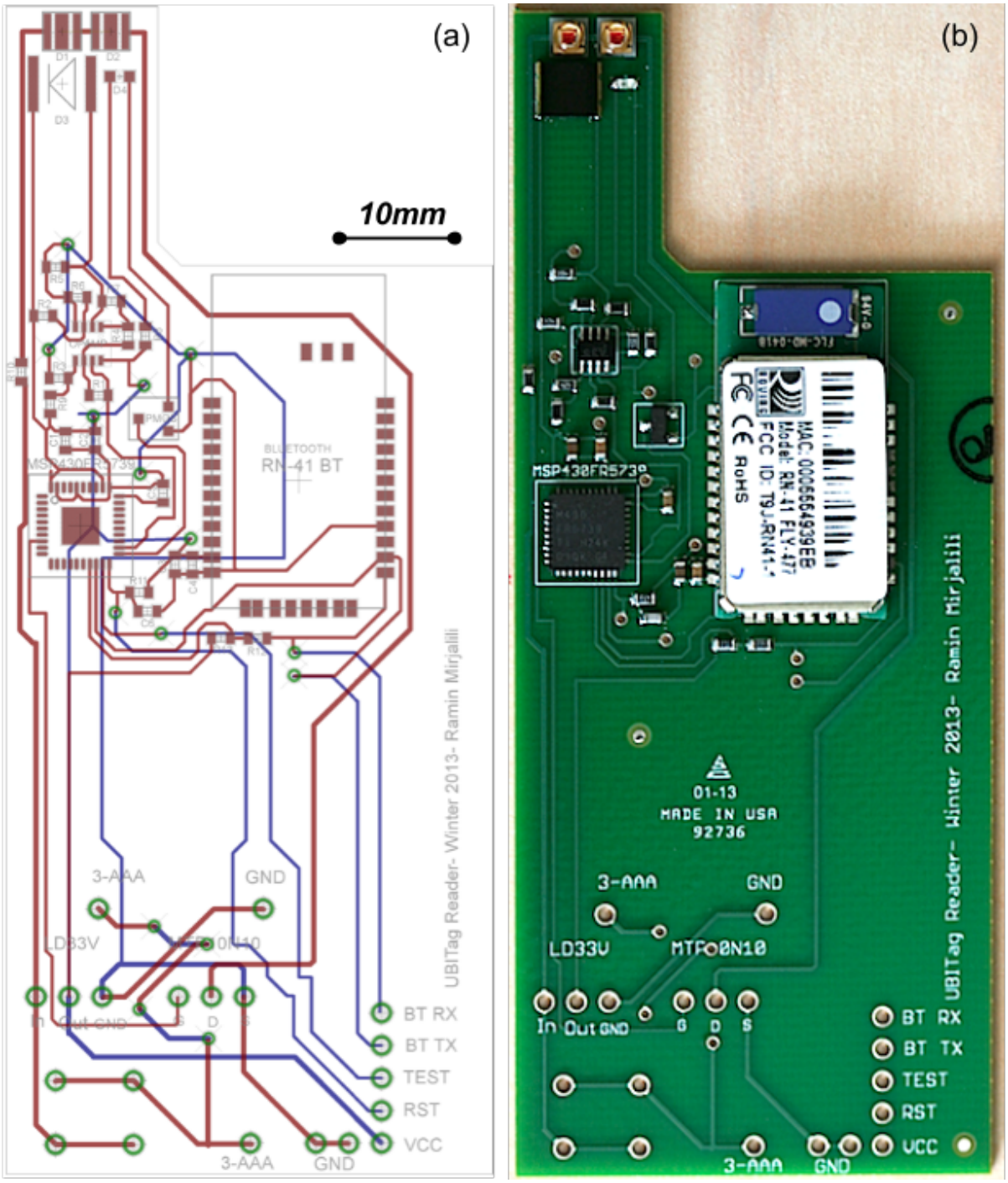

Figure 3.21 a) Reader PCB design, b) Manufactured board with SMT components

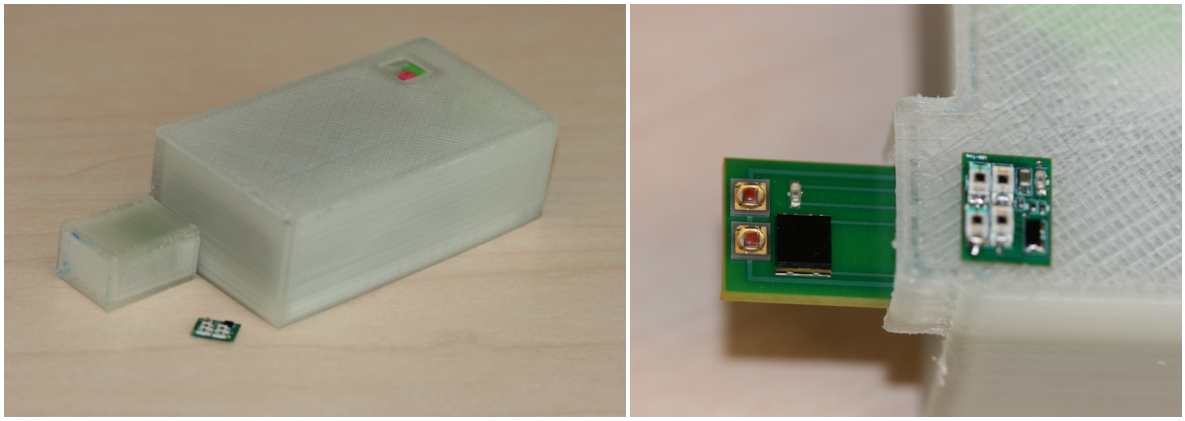

Figure 3.22 Reader, packaged in a 3D printed box, with a cap to access optical head

3.4.2 Software

3.4.2.1 Protocol

Utilizing microcontroller units as the main processing block will facilitate establishing a communication thread between Reader-Tag-mobile device using standard protocols. As we envisioned assigning a unique ID to every object and storing complete information on the cloud, the data package swinging between devices, the ID, should be small. For our prototype purposes, the ID was selected as a 64-bit integer, giving sufficient unique options. To reduce power consumption required for higher clock frequencies, a 9600 baud rate was chosen for serial communication.

3.4.2.2 MCUs Firmware

With only 2 MCU's communicating at a time- Reader with one tag, an asynchronous serial connection (UART: Universal Asynchronous Receiver/Transmitter) can be established between them. Depending on the command byte (Write or Read) sent by the Reader, the tag will either store the 8-byte data package or transmit the previously stored data pack optically. A flow chart of the Tag's MCU is sketched in Figure 3.23. A key consideration is minimizing power consumption for tag circuitry. Texas Instruments offers several low-power modes for

its MSP430 product family. Setting the MCU to Low Power Mode 3 (LPM3) and DCO to the lowest frequency (5.3MHz) reduces the current consumption down to 100µA at 2V of power supply.

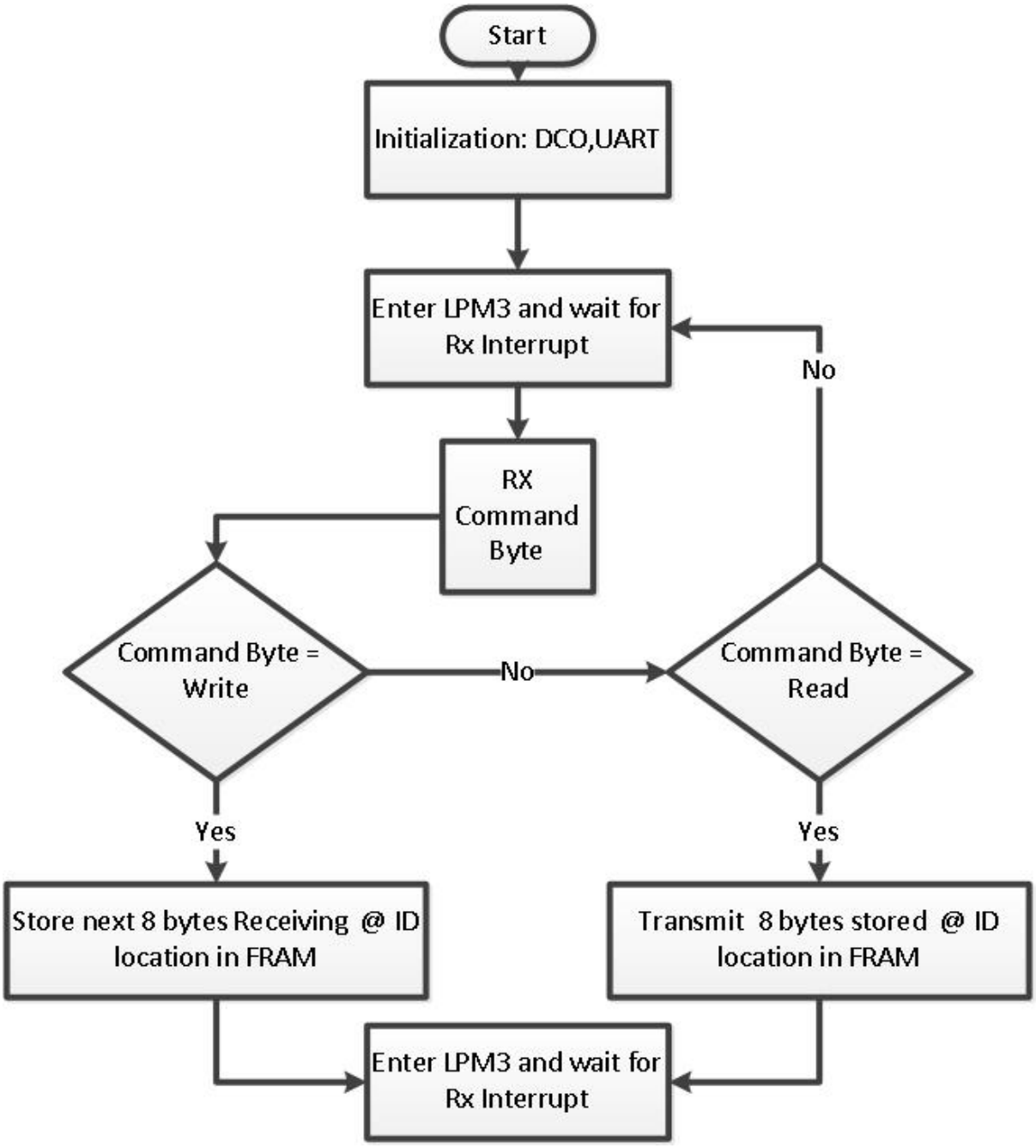

Figure 3.23 Tag MCU flow chart

On the Reader side we utilized another member of the MSP430FR57xx family with 2 UART channels (MSP430FR5739), assigning one port for communicating with the tag and the other for communicating with the Bluetooth device. Depending on the command

(Write/Read/Retrieve) transmitted from the handheld device to the Reader's Bluetooth, the Reader will either store the new data and assigns it to the tag optically, or read out the tag ID and store it, or transmits the previously read-out tag ID to handheld device for database investigation. Whether the Reader is interacting with the tag on Write or Read cycles, a designated NMOS switch would be activated to turn on the bright LEDs to supply optical power for the tag (Figure 3.20). A flow chart for Reader logic is sketched in Figure 3.24.

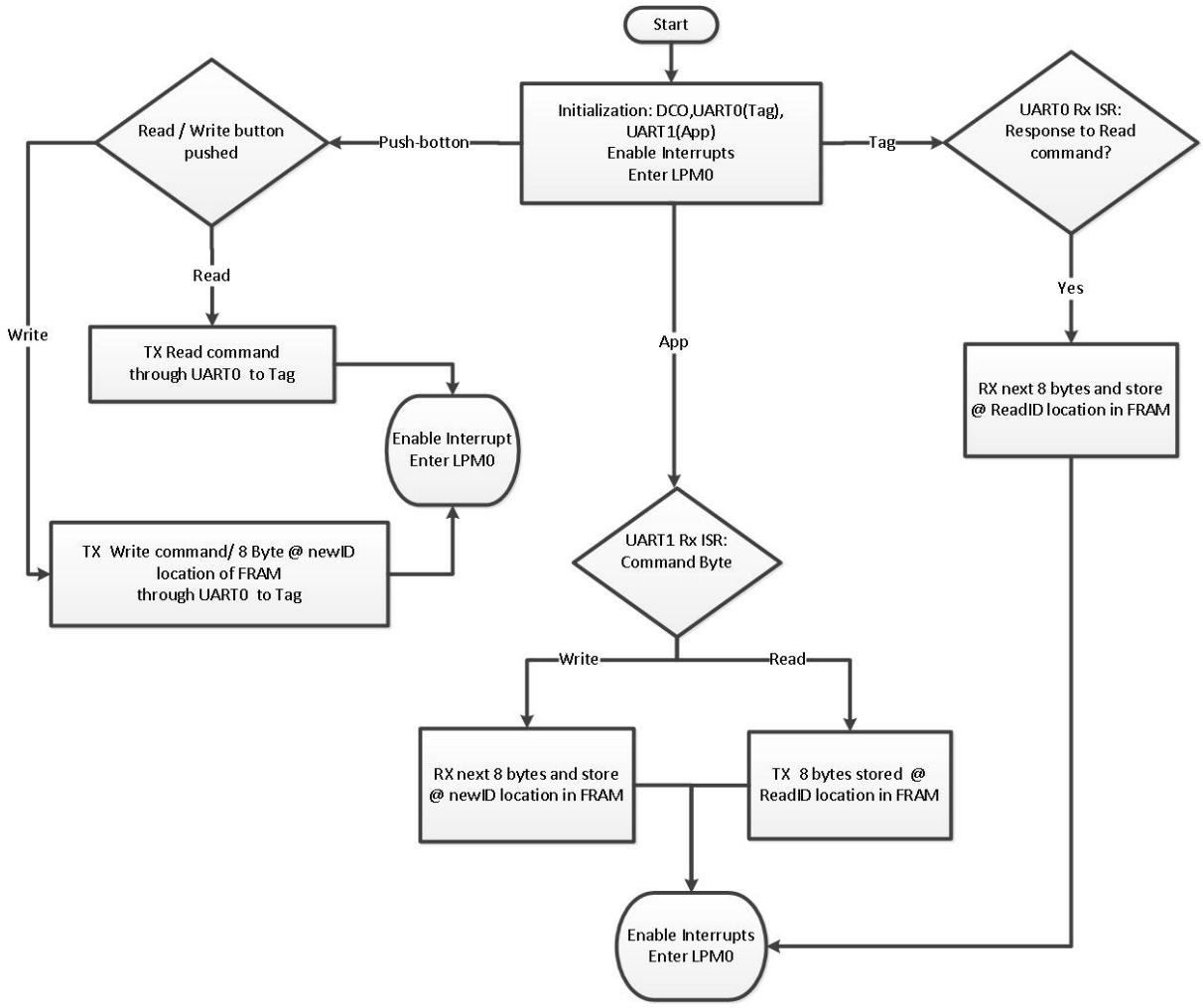

Figure 3.24 Reader MCU flow charts

Proper coding for Reader and tag MCUs was implemented using TI's Code Composer Studio v5 software (provided in Appendix A). Output signals of the emulator were directly probed to MCU pads through probe-station needles.

3.4.2.3 Database development

Since we envision assigning a unique ID to any object and storing the complementary information on the ubiquitous cloud, the next step is to develop a global database for our infrastructure.

We first needed to set up web-server software (Apache 2) on a personal computer and make the local IP accessible through the Internet. Using MySQL for database development, we created a database, named UBITagDatabase, containing a single table called ubitaginformation containing 2 columns: TagID and TagInfo. The first one is the unique integer ID, which will be assigned to each tag (64bit data swings between tag and Reader), and the second one is the complete description of the object in text format. In order to update or read from the database, queries should be executed through a conventional database interfacing syntax such as PHP. The following 3 pieces of code have been developed to cover the basic objectives of our prototype (the syntax is provided in Appendix B).

1- write.php: It will get a new ID from user ($_GET[]). The entered data will first be checked to not be blank (!empty) and to be an integer (is_int($TagID)). Passing the *is_int* test, it will execute a SELECT query to check for redundancy of TagID. In case of a redundant ID the proper text warning will be printed (Figure 3.25), otherwise it will create a 2-segment PHP form (Figure 3.26):

- One for TagID filled with number entered by user in readonly format to prevent any further change in this step.
- A large textbox for entering the object definition.

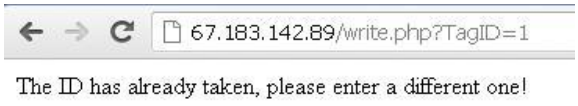

Figure 3.25 Message in case of redundant ID selection

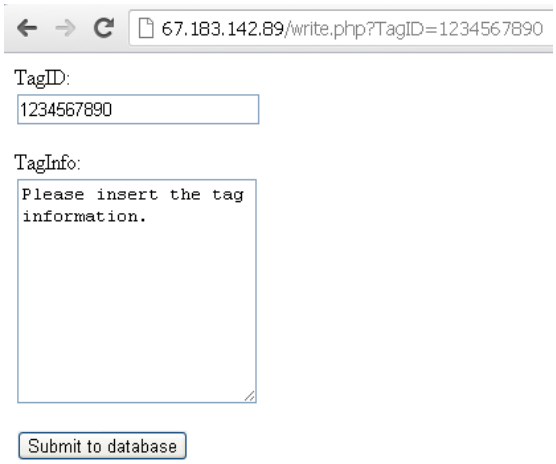

Figure 3.26 New ID/Information assignment form

Once submitted to the database, the information will be posted to the second PHP code (action: newtag.php).

2- newtag.php: Having received the information posted from write.php, the database will be updated by executing INSERT INTO query and the update confirmation message on display will be printed (Figure 3.27).

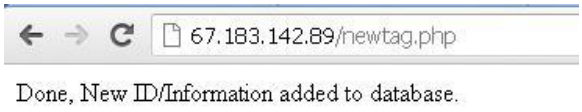

Figure 3.27 Confirmation message after each database update

3- read.php: This code will get the ID ($_GET[]) retrieved from the Reader and search through the database for a matching TagID column. In case of no match it will show a no-entry message (Figure 3.28); otherwise TagID and TagInfo will be showed to user (Figure 3.29).

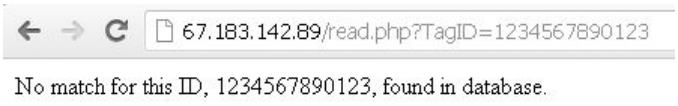

Figure 3.28 No-entry matched message for ID

Figure 3.29 TagID and TagInfo looked up from database

3.4.2.4 Mobile Application development

The Android platform was chosen to develop the user frontend Application. The main objectives of this application are listed below:

1) Create Bluetooth connection thread with Reader to establish in/out stream

2) Get a new ID from user

3) Check the database for redundancy; get the object definition from user and update the database

4) Send the new ID to the Reader via Bluetooth and command the Reader for optical assignment of the ID to the tag

5) Read out the ID from the tag and store it in Reader

6) Retrieve recently read-out ID from Reader, look it up in database, and display respective database entry to user.

Using Eclipse software, a single-activity application was developed with 5 buttons, 1 editable textview and 1 webview segment (Figure 3.30). The tasks assigned to each segment are described below:

1) Connect button: Creates a Bluetooth thread with MCU's Bluetooth and establishes in/out stream.

2) Editable Texview: User enters the new ID here.

3) Check button: The App checks that the ID is entered in integer format and then posts the ID to write.php through the webview segment. As described before, write.php will get the ID and load the PHP form for updating the database. Further submission is accomplished through webview. Additionally, pushing the Check button converts the legitimate ID into a byte array for transmission to the Reader.

4) Write button: A command/data package comprising a single byte command followed by an 8-byte ID array will be sent to the Reader through the Bluetooth OutputStream, and the Reader will perform consequent optical assignment.

5) Retrieve button: A single command byte will be sent to the Reader, the Reader will optically command the Tag, and then the Reader will receive an 8-byte array of data from the Tag, which will be stored as read-out data in the Reader's flash memory.

6) Read button: A single command byte will be sent to the Reader to retrieve recent read-out data from the Tag. The 8-byte data will be converted to its long integer format and then posted as input for read.php. Hence, the database investigation will be executed and the proper result will be displayed through the webview segment.

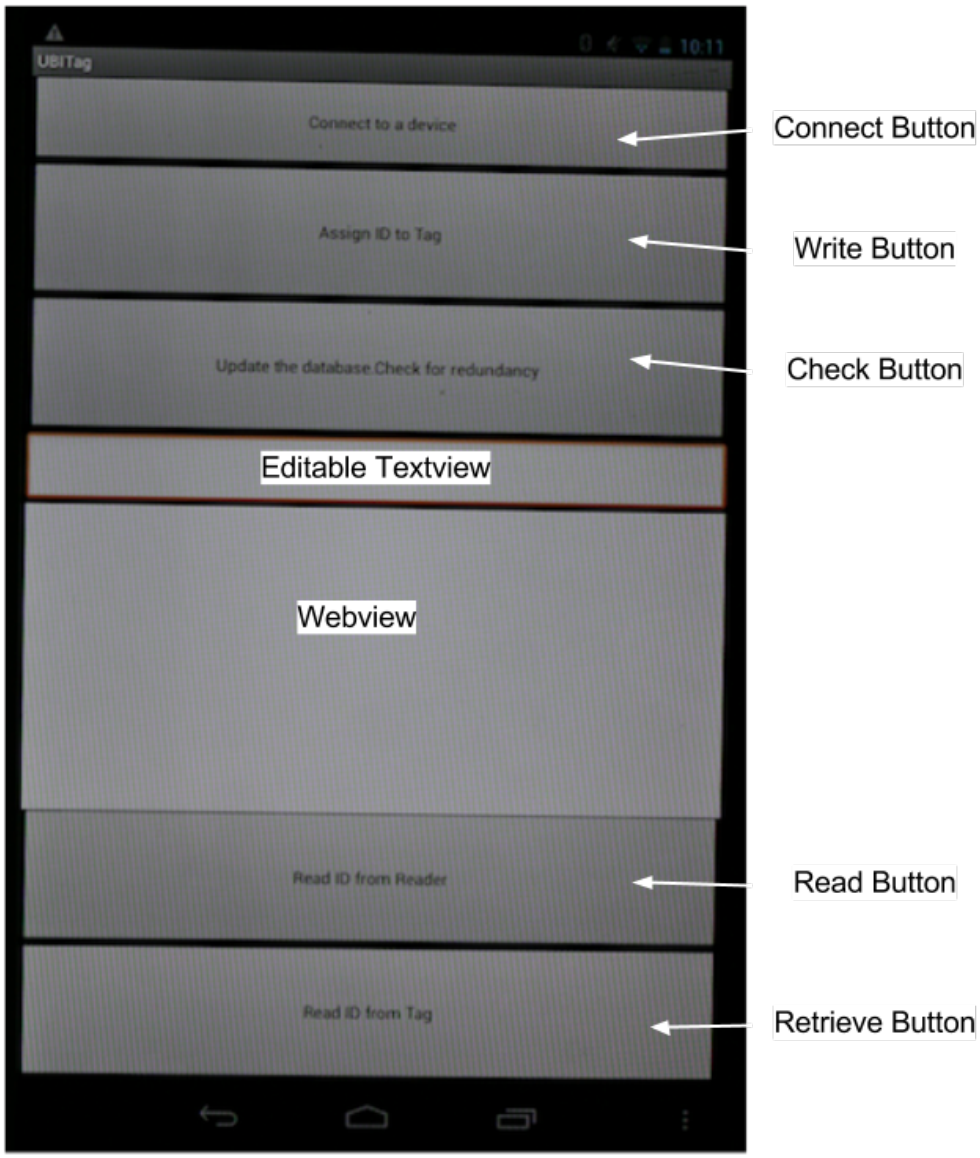

Figure 3.30 Android UBITag Application interface.

3.4.3 Infrastructure Prototype, demonstration result

Utilizing the miniature-size and low-power components available, with a view toward minimizing tag circuit size, the board was manufactured with dimensions of 9.7mm × 6.9 mm, with optoelectronic components on top and electronics on the bottom. For the custom designed Reader, with no intention of miniaturizing the board, the final circuit was manufactured with packaged dimensions of 25mm × 45 mm × 85 mm; it was powered by 3 AAA batteries and fully controlled by Android App via Bluetooth.

By programming the tag microcontroller to function in low-power mode, we measured the required power for the functional tag with detectable optical output around 800uW. Test wires were connected to the circuit's Vcc and GND nodes, and a 2V source was supplied for the Tag. A current consumption of 425uA was measured during active mode. Excluding a reverse current passing through the 4 PIN diodes in series, which was measured around ~35uA at 2V, the total current consumption of the tag with a detectable output signal was less than 400uA.

The complete infrastructure—comprising the Reader and tag circuit boards, the Android application, and the web database—demonstrates the universal identification system we envision. After running the UBITag application on an Android device and activating the Reader, a sample assignment procedure can be accomplished through the following steps:

a) Connect to Reader Bluetooth (Figure 3.31).

b) Enter new ID in textfield section of app. Check for redundancy. Error would be displayed in case of a redundant ID number (Figure 3.32).

c) Reenter a new non-redundant ID, if necessary (Figure 3.33).

d) New redundancy check, if necessary (Figure 3.34).

e) PHP form appears (Figure 3.35).

f) Enter information about the object in designated box (Figure 3.36).

g) ID and Info are submitted to database (Figure 3.37).

h) Assign new ID to the tag by positioning the Reader optic head at the tag optic side proximity and clicking the "Write" button of the app (Figure 3.38).

i) Read-out the ID of the tag by locating Reader and tag properly and clicking the Read button of the app (Figure 3.39).

j) To retrieve the respective information of recently read-out ID, click the Retrieve button on App. ID and object definition would be displayed in the webview segment (Figure 3.40).

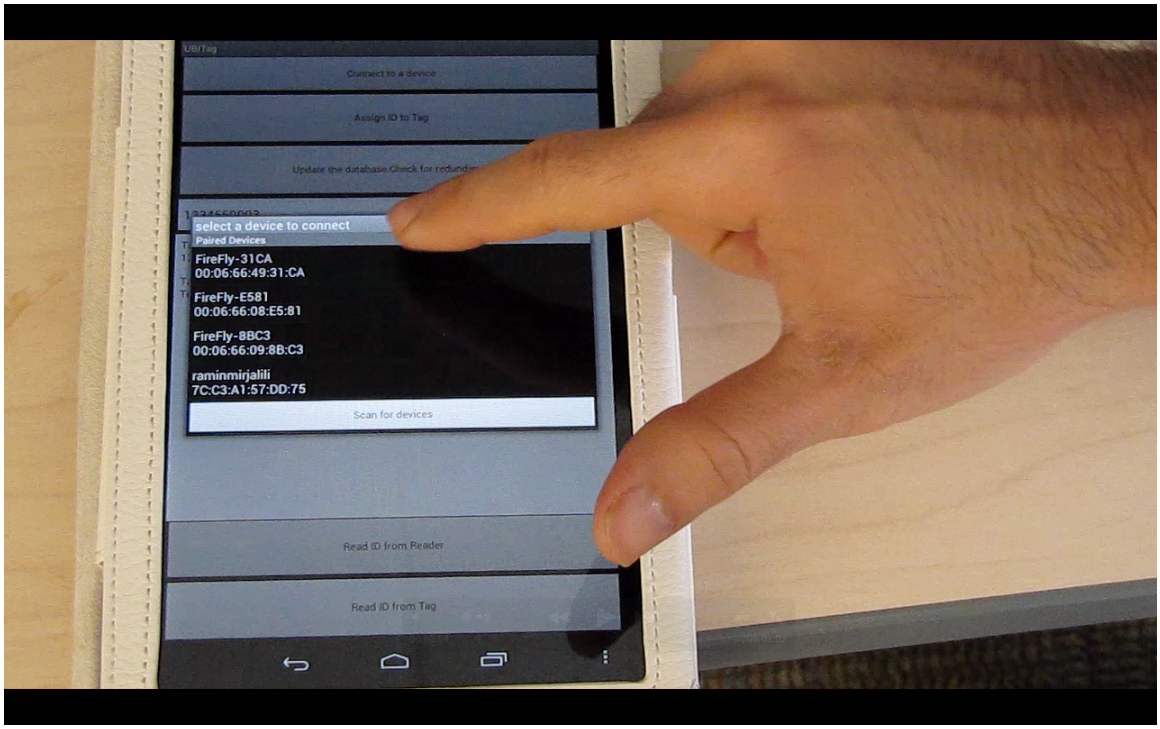

Figure 3.31 Connecting to Reader's Bluetooth

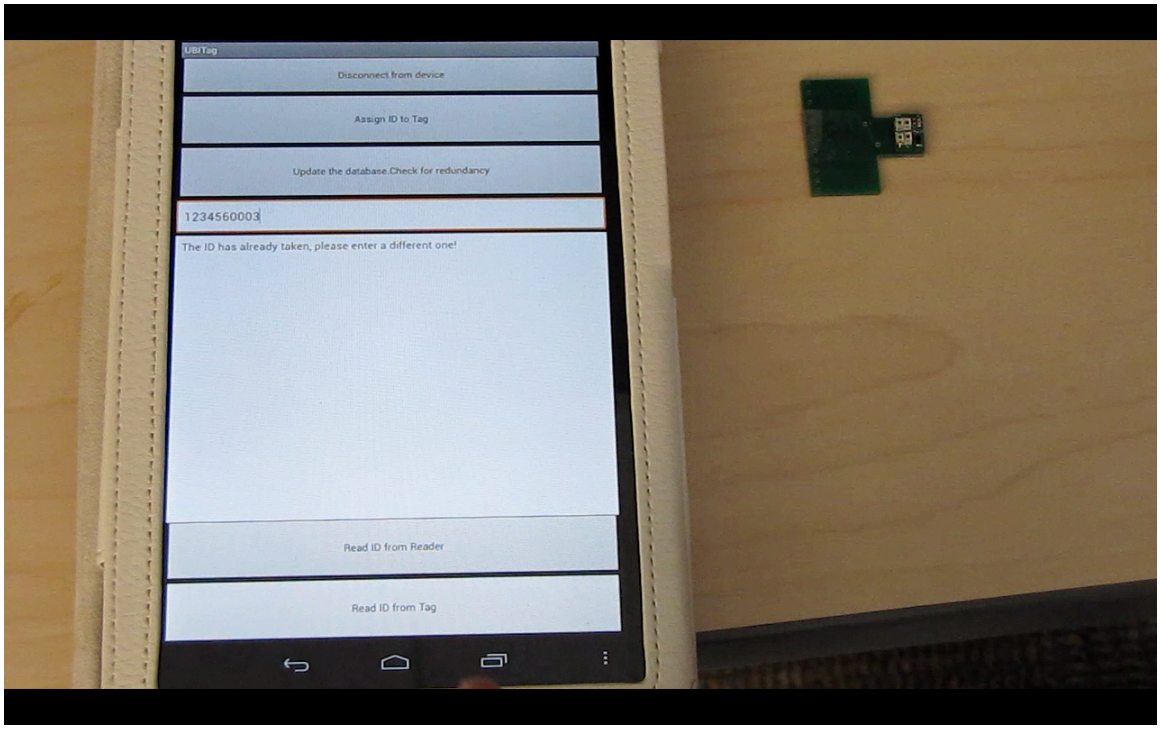

Figure 3.32 Error message to redundant entry.

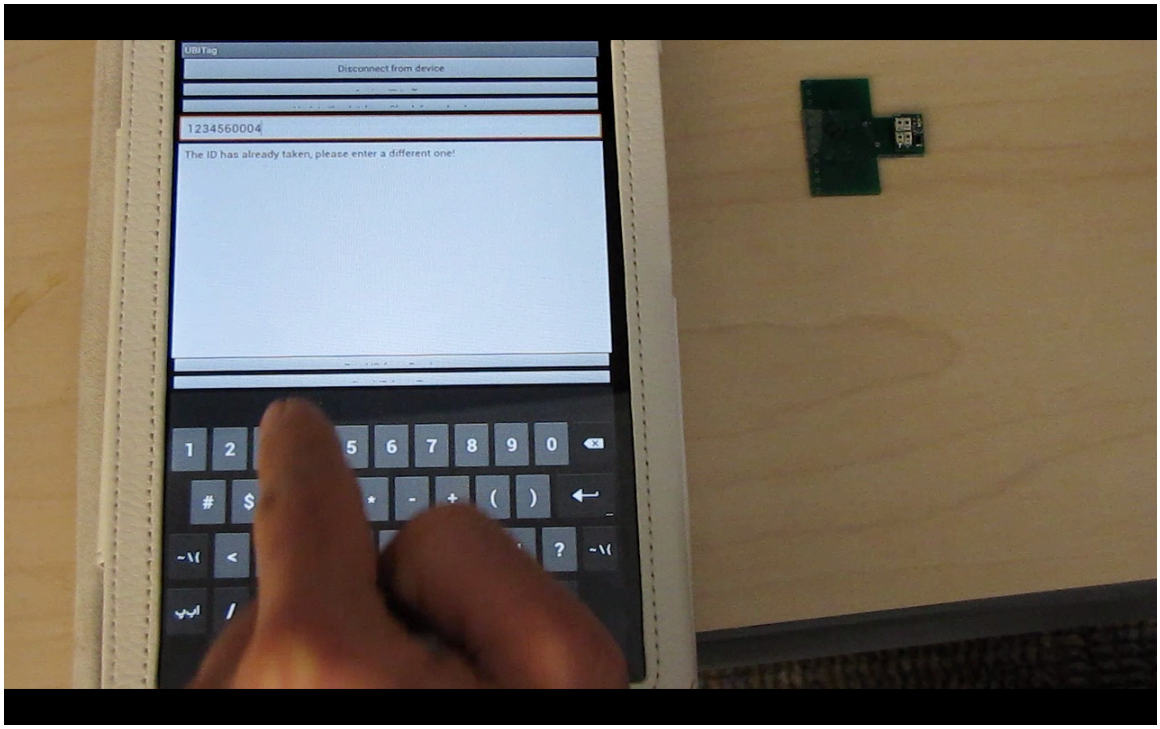

Figure 3.33 Entering a non-redundant ID.

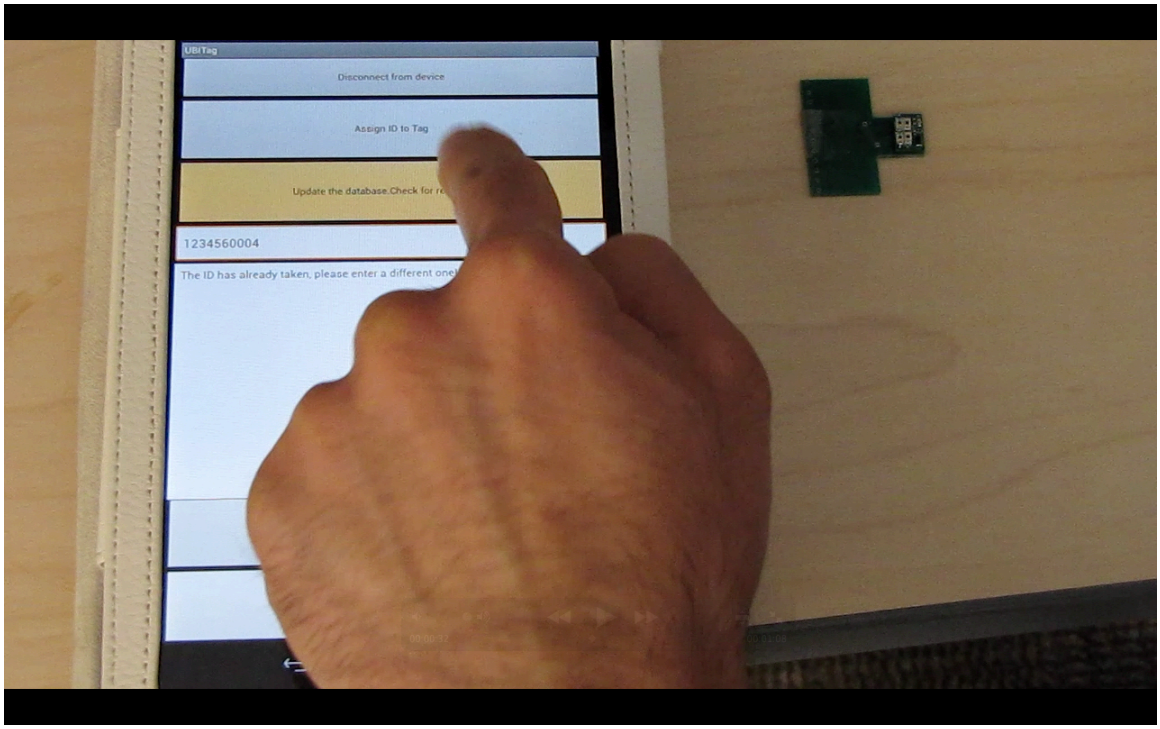

Figure 3.34 Checking database for redundancy.

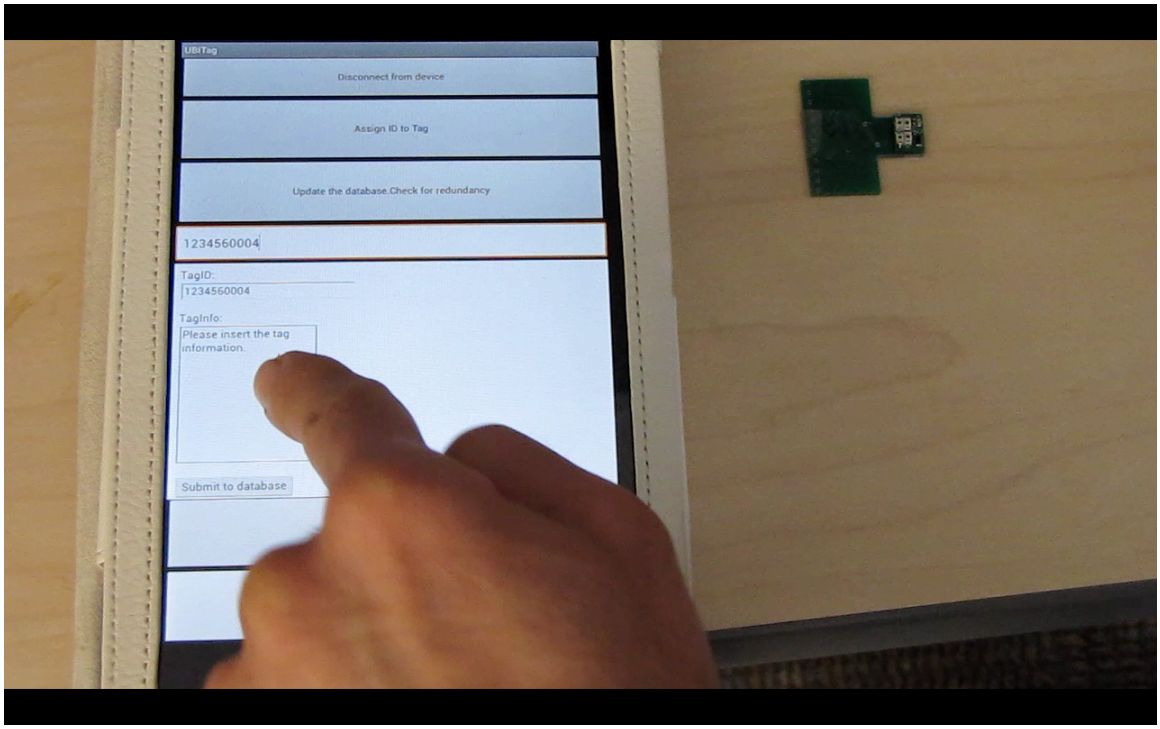

Figure 3.35 PHP form appears on the webview segment.

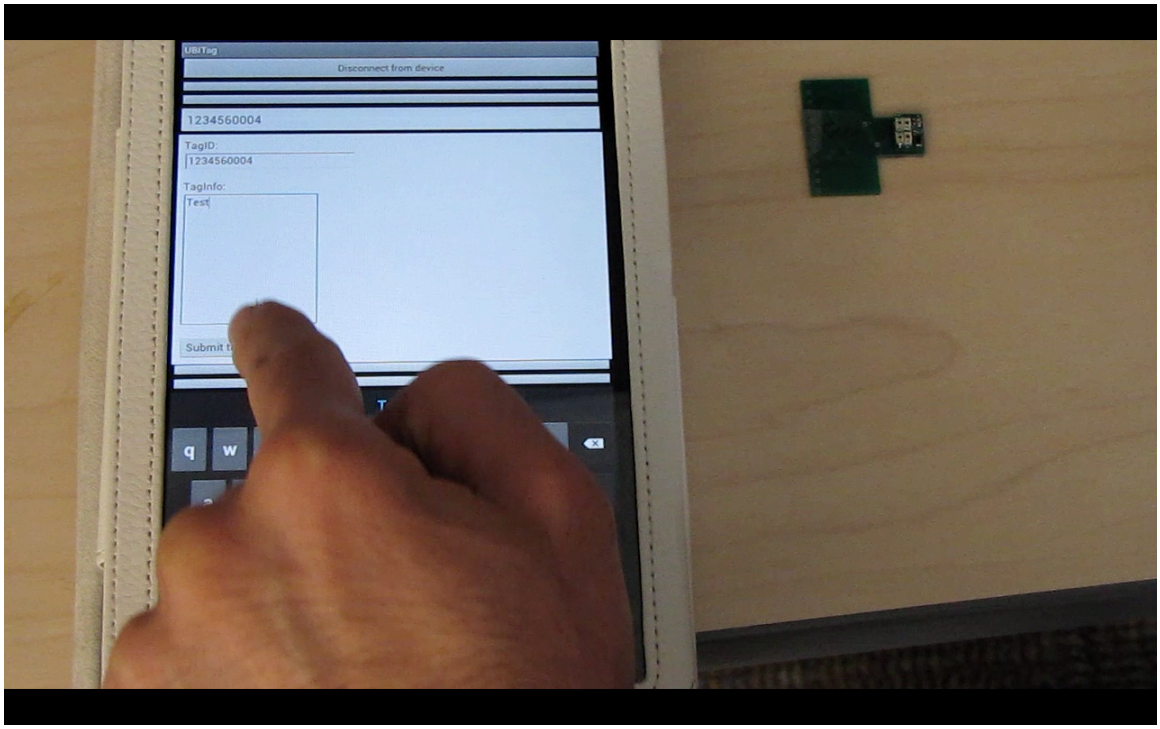

Figure 3.36 Entering tag's description: "Test".

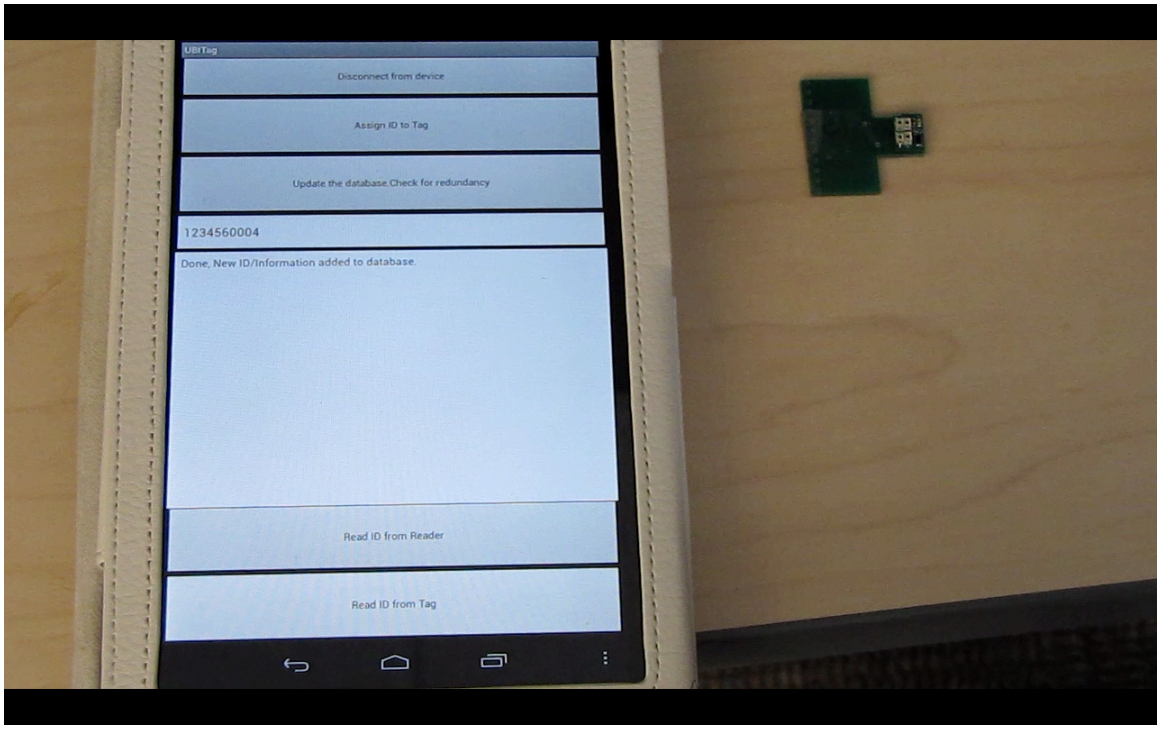

Figure 3.37 Update message is displayed once ID and Info are submitted to database.

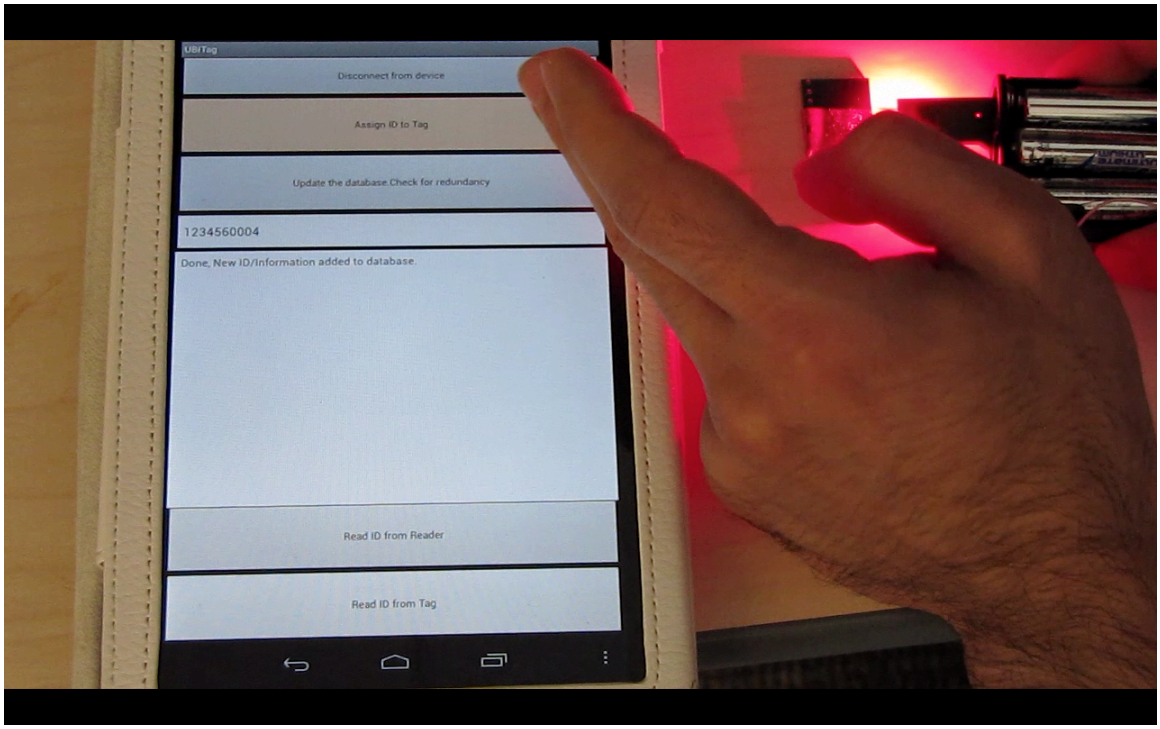

Figure 3.38 New ID assigned optically to Tag, controlled through the app.

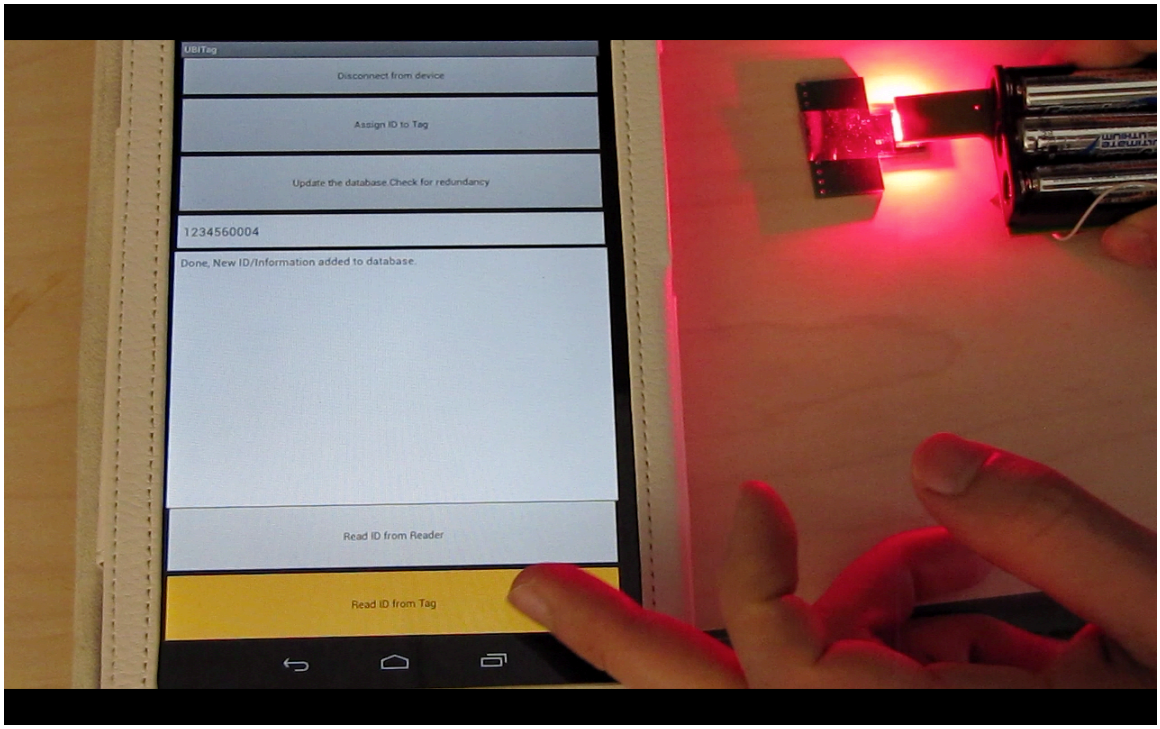

Figure 3.39 Tag ID can be readout optically, controlled through the app.

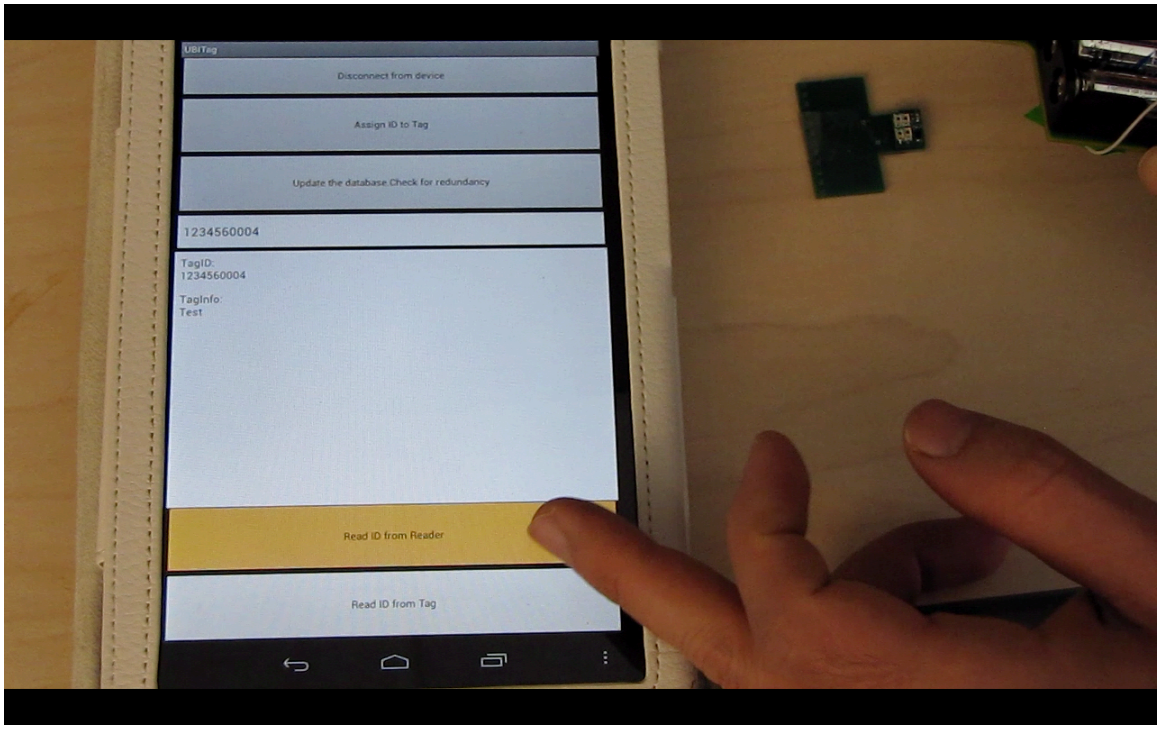

Figure 3.40 Read-out ID is sent from the Reader, and respective information is looked up and displayed through the app.

A compelling point of the infrastructure prototype is the functionality of the tag circuit, despite the spatial issues mentioned earlier, with a total optical input die area of 1.2mm× 1.2mm (4 PIN diodes of 0.6mm×0.6mm). Needless to say, the main challenge for any

autonomous system is supplying sufficient power, and the UBITag is no exception. The tag prototype harvests power via 4 individually packaged, serially connected PIN cells, and optical power comes from LEDs assembled on Reader board. The wide divergence angle of powering LEDs results in a rapid decrease of incident power on the tag harvesting block, with increasing distance from the Reader. Therefore the maximum Tag-Reader distance for sufficient power transfer is limited to millimeters for our prototype, while proper LED-PIN array alignment is required. Because our main objective in prototyping was only to prove the feasibility of universal identification based on a miniature optical Tag, however, we took no further steps toward improving communication distance, as it is a matter of reengineering.

3.4 Encapsulation of miniature components

As another step toward realization of the UBITag system, we developed a packaging process to encapsulate the miniature chip. The UBITag chip is envisioned as a miniature autonomous system, receiving power and communicating data through an optical path. Because the tag chip will eventually include an organic component, the system must be protected from the environment's oxygen and humidity. Therefore the miniature system must be encapsulated in a chemically and physically robust material that is optically transparent. In addition, packaging should not hinder the creation of an optical path between the tag and the Reader. In our process, we encapsulated the UBITag chip in transparent resin spheres with partial reflective coating, which can improve optical performance of the system. The spherical shape adds refractive lensing behavior to the system, enhancing input optical power harvesting and collimating the UBITag's optical response to the Reader's call. Partial reflective coating on the resin drop can increase the possibility of creating an optical path between the Reader and the UBITag chip independent of the Tag's optical surface orientation toward Reader (Figure 3.41). The packaging process can be divided into 2 main sub-processes: Encapsulating

miniature chips in transparent sphere-shaped packages, and depositing the partial reflective coating on the sphere drops.

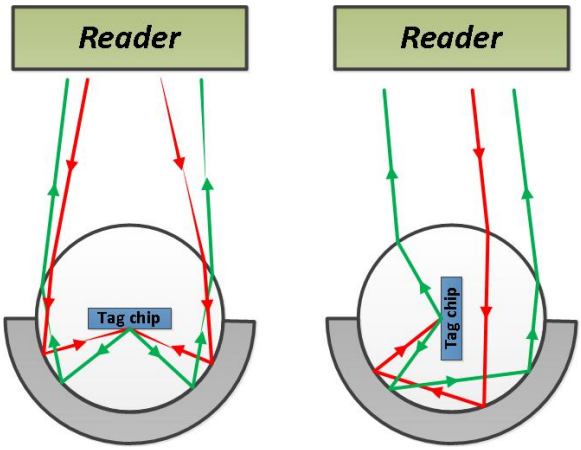

Figure 3.41 Envisioned packaging: spherical shape with partial reflective coating, which helps to create an optical path between tag chip and Reader

3.4.1 Sphere Encapsulation

Miniature silicon chips were used to demonstrate the packaging process. A conventional 4-inch silicon wafer was saw-diced with 1 mm spacing, resulting in ~950 um square chips (Figure 3.42).

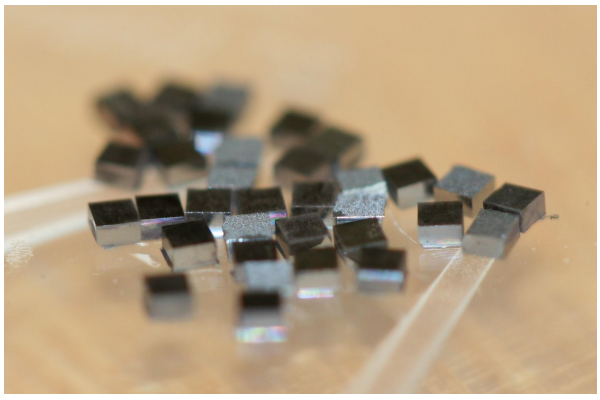

Figure 3.42 Saw-diced silicon dummy chips, 950um square, used for packaging development

A spherical shape can be achieved using a 2-piece mold with hemispheric cavities (Figure 3.43). Aluminum molds with hemispheric cavities with a diameter range of 1.8mm-2.4mm were made through machine milling (Figure 3.44).

Figure 3.43 Two matching mold halves with hemispheric cavities to create miniature-size spheres

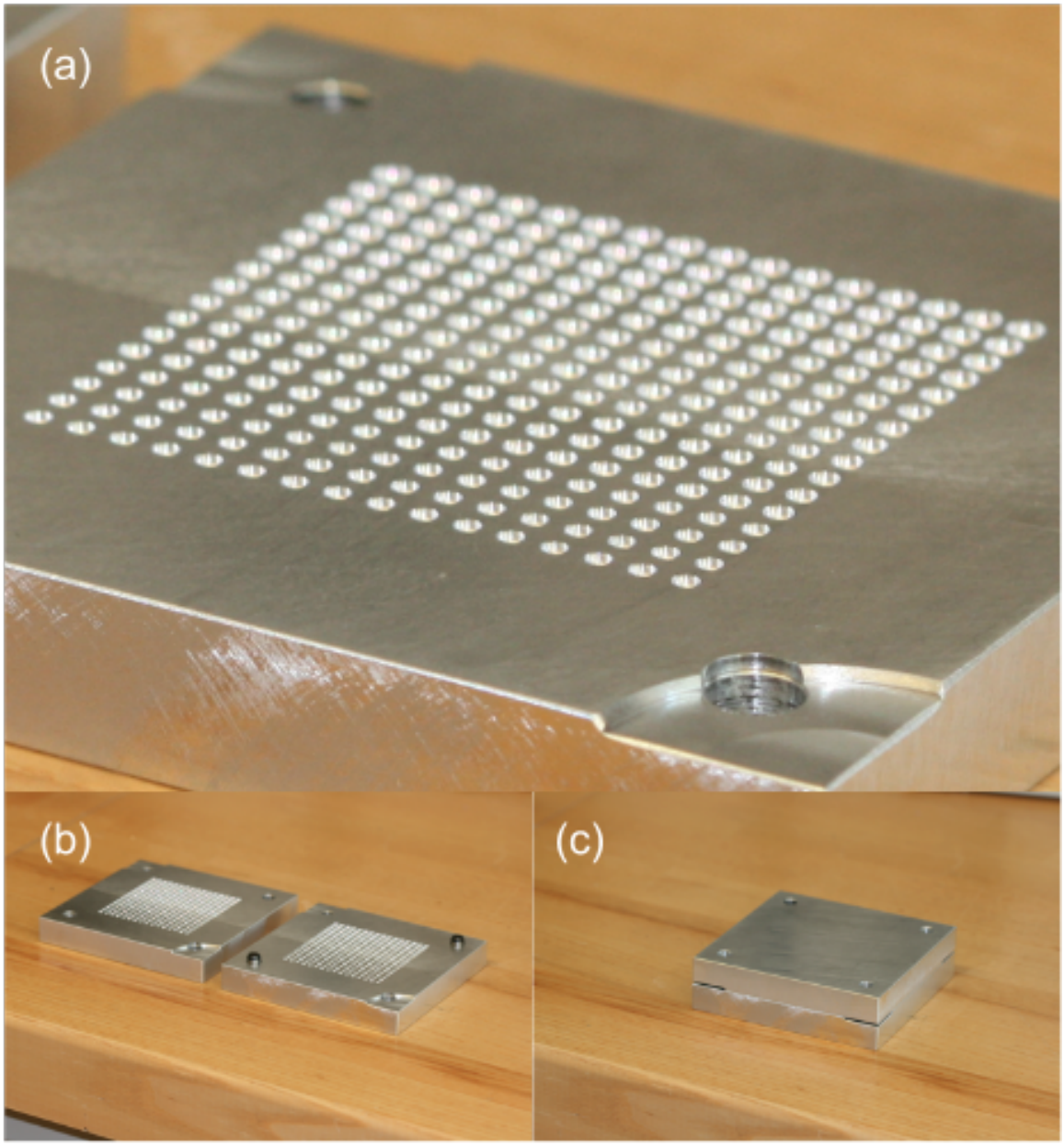

Figure 3.44 a) Cavities of various radii were machine milled on b) two-piece and c) matching mold.

Clear epoxide resin (EPOTEK 302-M) was chosen as the encapsulation material due to several promising encapsulation properties: chemical and physical robustness, optical clarity, and cost effectiveness. To facilitate releasing cured resin drops, a dry PTFE release agent (Miller Stephenson 122AD) was applied from an aerosol container and then cured at 305-315C for 10 minutes to fuse the Teflon layer. Epoxy was prepared by mixing proper portions of a 2-part batch, degassed under vacuum for 5 minutes, and poured over one of the mold

halves (bottom half). Excess epoxy was wiped off using a glass slide, leaving the cavities partially filled (Figure 3.45a). Then the bottom half was put in a convection oven at 65C for 30-45 minutes to gel the epoxy, hence cushioning the silicon chip, now located at the middle of the sphere.

After the first cast/cure step, a fresh epoxy layer was poured over both halves and the extra amount on the bottom half was wiped off (Figure 3.45b). This process prevents air bubbles trapped between the silicon chip's flat surface and the concave surface of the cured epoxy layer of the first cast/cure stage; it also creates a liquid trap for the silicon chips, thereby helping to allocate them to the center of the cavity recess after dropping.

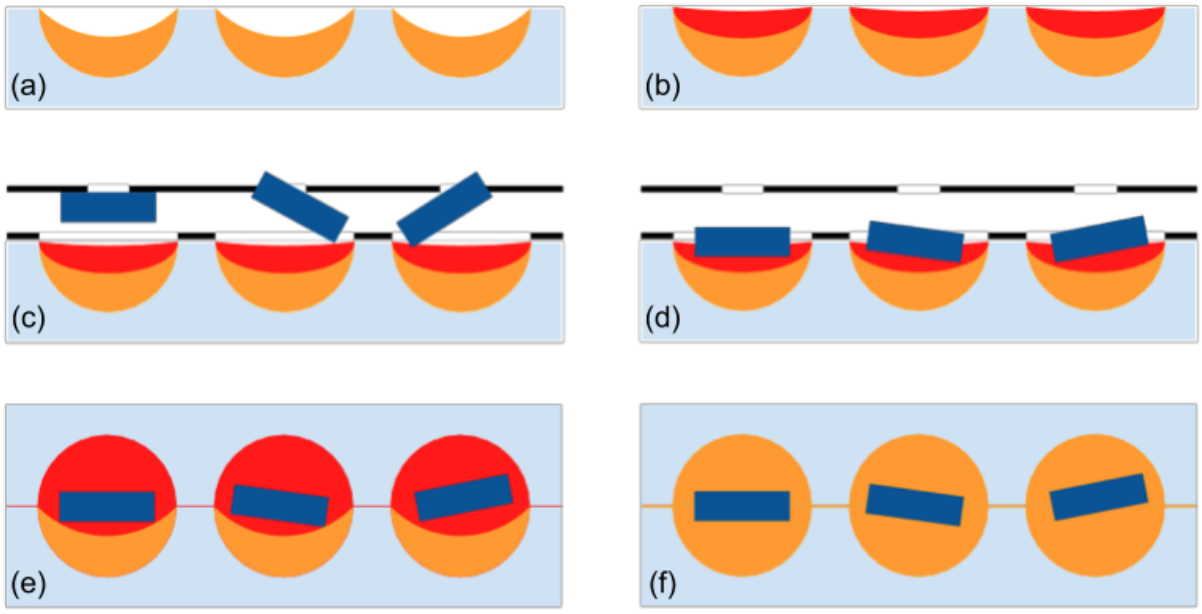

Figure 3.45 a) One of the mold halves is partially filled with epoxy then cured to create cushioning for Si chips. b) Second layer of fresh epoxy on the first cured one helps to prevent air bubbles trapped under Si chips. c) Protective mesh covers mold's surface and vacuum-gripped chips would align on top of cavities. d) Chips would release by breaking vacuum of gripper. For our experiments chips were manually dropped in cavities. e) Second mold half with fresh epoxy casted on would match and seal the bottom half. f) Resin would solidify through thermal curing at 65° C.

Then a protective mesh with matching mold patterns was placed on the bottom half (Figure 3.45c, 2.46) to cover the mold's flat surface and leave cavities open. This would prevent silicon chips from being dropped on the mold's flat surface and hindering the proper sealing of the two halves.

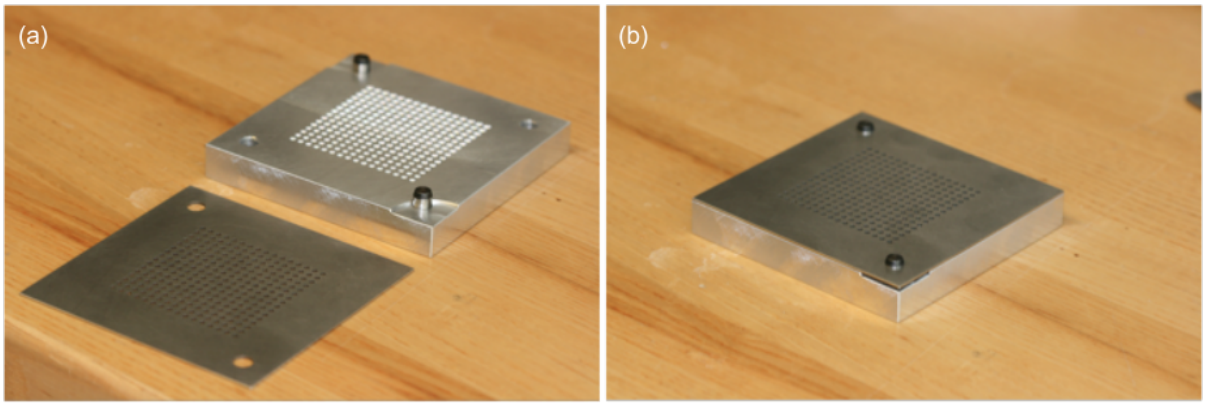

Figure 3.46 Protective mesh covers flat surface of mold half. a) Off the mold, b) On the mold

Afterward, chips were dropped into the epoxy-filled cavities using tweezers. Manual dropping can eventually be replaced by a vacuum-driven gripper with a matching mold pattern, eliminating the need for hand manipulation or precision robotics (Figure 3.45c, d).

After dropping the chips, the protective mesh was removed, and the two halves were sealed together (Figure 3.45e) and cured at 65ºC for ~3hrs in a convection oven (Figure 3.45f). Once cured, mold halves were separated from each other and immersed in acetone for ~10 seconds to peel off the flash layer (a thin layer caused by leakage of epoxy between the two surfaces of the mold), then dried by blowing nitrogen. To make the epoxy more fragile and ease the deflashing, we cooled the mold halves to ~0ºC and removed the flash layer by vigorous deburring using a plastic brush with miniscule damage to the spheres' exposed surfaces.

The results of packaging at various diameters revealed that the chip would allocate better at approximate center of the smaller sphere—yet another reason to aim for a more miniature product (Figure 3.47). Thus, we continued to conduct the mirror layer deposition on the smallest packagings.

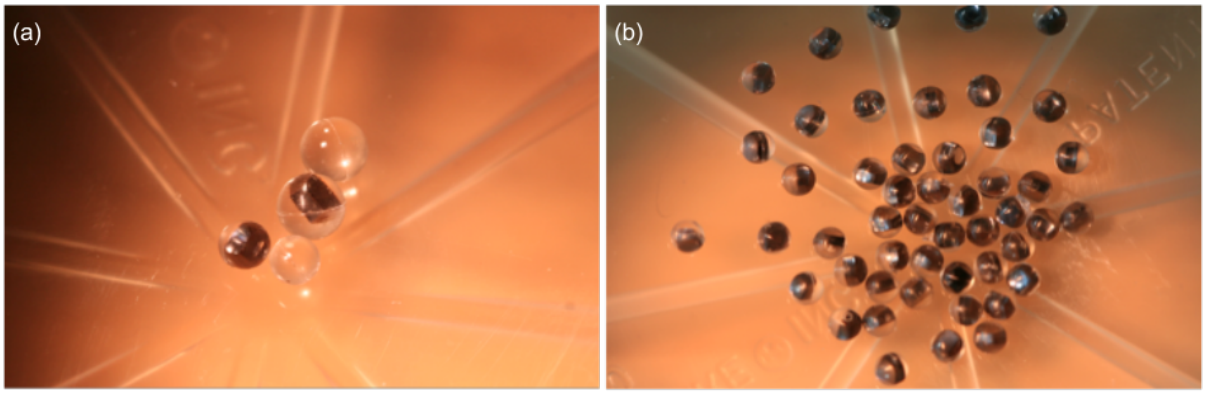

Figure 3.47 a) Chips encapsulated in larger spheres (2.4mm, 2mm diamter) have more deviation from center, b) a less frequent problem for smaller spheres (1.8mm diameter)

3.4.2 Reflective coating deposition

The envisioned packaging would be completed by depositing partial reflective coating. The best reflection through the widest optical spectrum range can be achieved by using silver as the main reflector. Preventing silver from tarnishing requires an oxidation barrier, which can be selected among transparent dielectric materials such as SiO2. An important point to consider for selecting a deposition method is the necessity of a low-temperature process to prevent epoxide and the organic materials of the UBITag from degradation. Silver can be deposited using an E-beam evaporator. Depending on the required thickness and quality of the film, SiO2 can be thermally grown or deposited through chemical or physical vapor deposition (PECVD, ICP-CVD and E-beam evaporation). In thermal oxidation, silicon is oxidized through a high-temperature process. PECVD is also a high-temperature process (~300ºC). ICP-CVD, despite being low-temperature, may not be the most cost-effective method. Furthermore, temporary protection of silver from tarnishing during the transition from the Ebeam evaporator to the SiO2 deposition chamber is inevitable. Considering these issues and looking for a cost-effective method, we deposited SiO2 consequently after the evaporation of the reflector layer using an E-beam evaporator without breaking the vacuum. The main problem with evaporating SiO2 is its poor thermal conductivity, which resulted in

local melting of pallets loaded in E-beam evaporator crucibles. This method affects the consistency of the deposition rate and consequently the quality of the film; therefore we introduced an aluminum layer as the main oxidation barrier on top of the silver and deposited SiO2 as physical protection for the metal layers (Figure 3.48). It should be noted that for improving metal adhesion to the epoxy surface, the mold halves (embedding epoxy drops) were treated with oxygen plasma prior to the mirror layer deposition step.

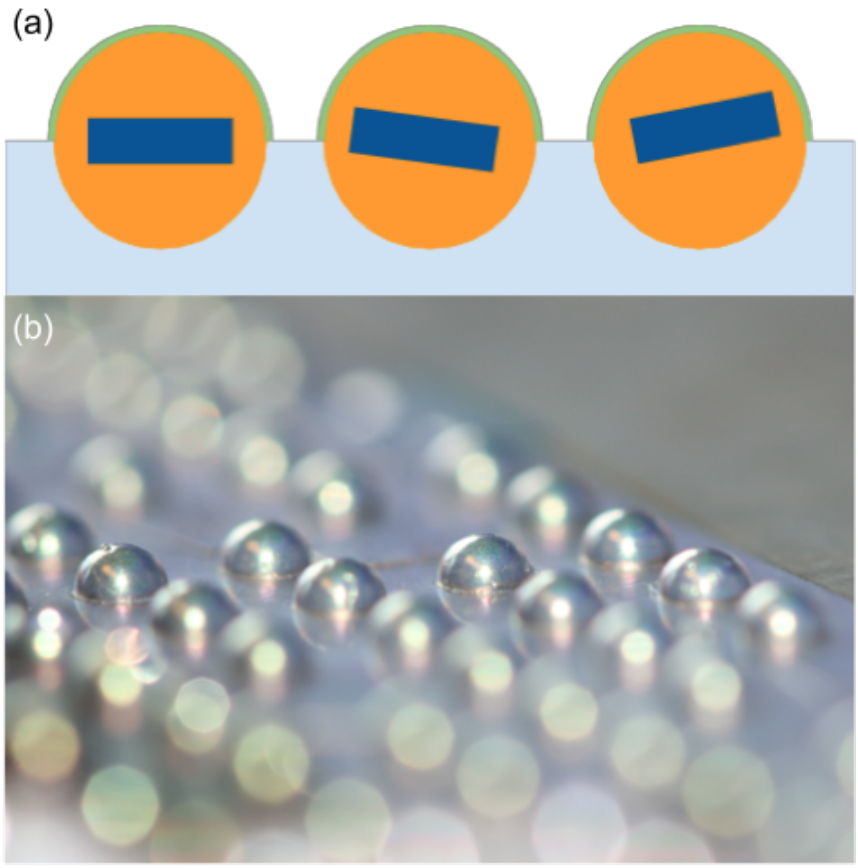

Figure 3.48 a) Mirror layer deposited on epoxy spheres while they are secured on mold, b) sample result of on-mold mirror deposition

3.4.3 Release and Attachment

Once the mirror layers are deposited, the mold halves were removed from the chamber and heated to a point close to the glass temperature of epoxy (~40ºC), and then resin drops were released with minor physical manipulation (Figure 3.49).

Figure 3.49 Epoxy drops of 1.75mm diameter, with mirror layers on them, released from the mold

A minimum obtuseness (a=10º) of the reflective layer line to the incident optical beam is required; because of partial coating on the spherical packaging, arbitrary attachment of a single sphere would only give a 44% chance of optical link creation (Figure 3.50).

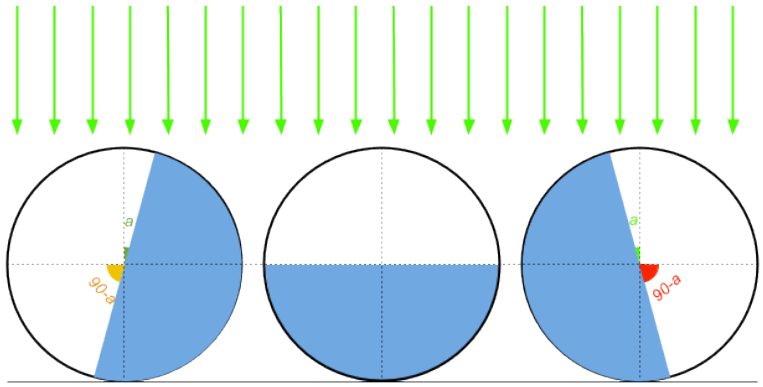

Figure 3.50 A minimum obtuseness, *a*, is required in order to create an optical link to the chip inside. Thus the probability would be *(180-2a)/360*, which would be 44% for *a*=10º.

Theoretically, then, to achieve a certain yield level, attachment of multiple spheres is required. Attaching 3, 4, 5, and 6 spheres respectively gives 83%, 90%, 95%, and 97% chances of optical path creation. Sphere packagings can be immersed in clear liquid adhesive (such as Cyanoacrylate or Polyvinyl Alcohol aqueous solution), and the preferred number of spheres can be attached to a single object through conventional printing, either by a single emulsion drop containing multiple spheres or by a sequence of single-sphere printing (Figure 3.51). The major resulting deficiency is the cost increase due to the need for of multiple tags per object.

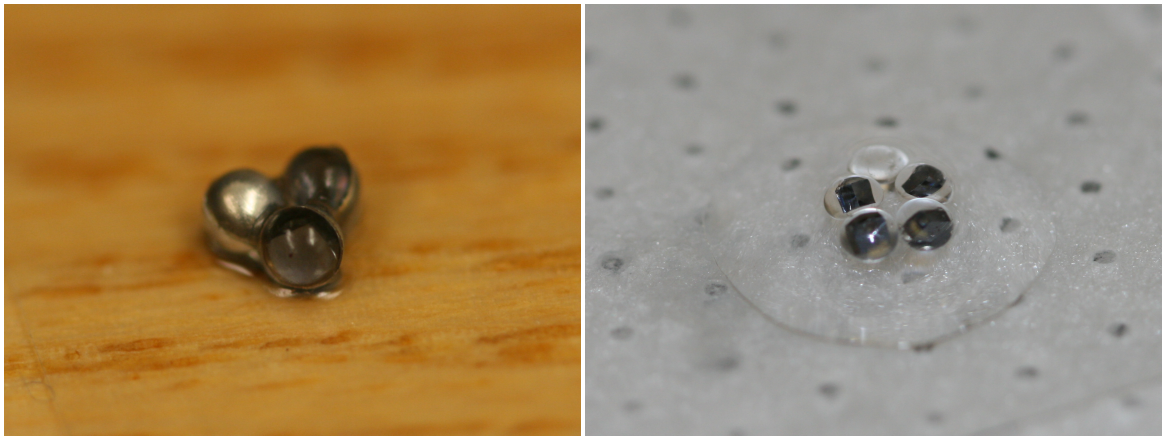

Figure 3.51 Multiple sphere attachment using a clear adhesive drop containing multiple spheres. This process eventually can be accomplished through a procedure analogous to conventional printing.

To eliminate the need for multiple sphere attachment, we improved the packaging in such a way that a single drop can be attached through a practical method, while the clear side of package would face away from the object,t with a yield larger than 96.7%.

We modified the packaging by slightly moving the spheres' center of gravity toward the mirror side, which also makes the packaging a 2-sided object. We achieved this by performing an additional molding step after mirror deposition on the spheres and before their release from molds (Figure 3.52 a, b).

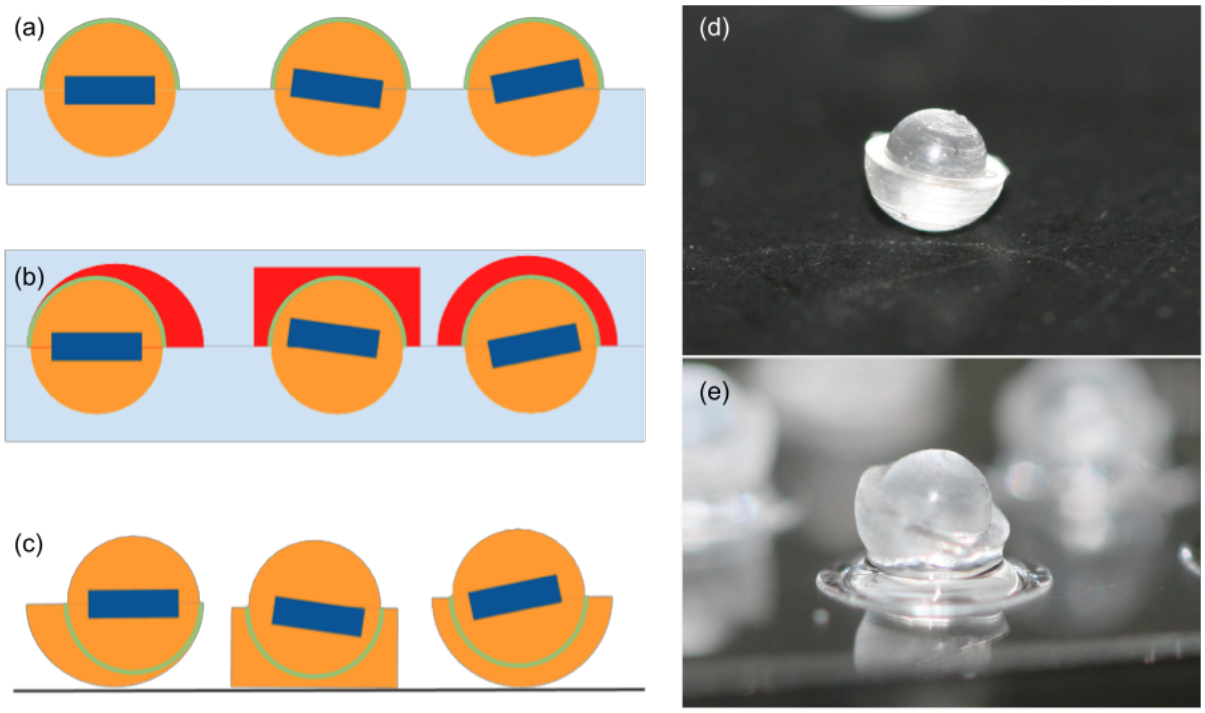

Figure 3.52 a) After depositing mirror layers, b) an extra molding step to make the packaging shape aspheric and two sided; c, d) release of modified packaging. e) Sample attachment of a single modified packaging through the sequence illustrated in Figure 51

After curing and release (Figure 3.52 c, d), a single packaging attachment can be performed by a simple hack into the conventional pick/place machine through the sequence described in Figure 3.53. First a packaging can be picked with random orientation using vacuum gripping; a liquid adhesive spot would then be dropped on the preferred location on the object's surface. Then the packaging would be released from a distinct distance above the glue spot. The essence of distinct release height is to provide the packaging with the required time to align its center of gravity. Performing this method and releasing the packagings from a ~20mm distance above the surface, we successfully attached them, clear side facing up, with a 96.7% yield.

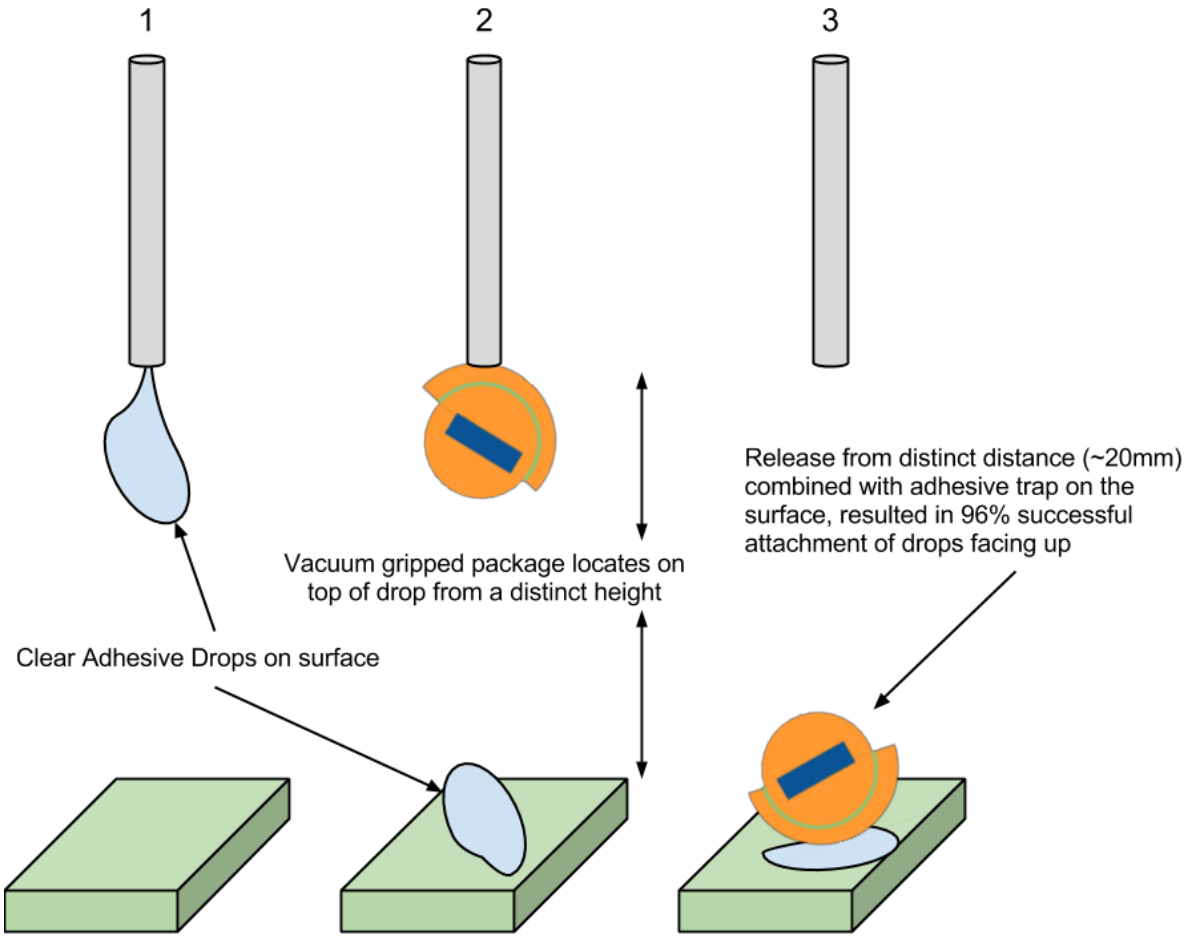

Figure 3.53 Modified packaging attaching method resulted in 96% successful result of single package with clear side facing up. This eliminates the need for multiple packagings for a single object, which linearly reduces the final cost per object.

3.4.4 Reflection measurement

The small size and curved surface of our packaging samples made reflectance measurement of their mirror surface with available equipment impractical. Therefore we performed the quality test for the same layer stack on transparent glass slides. An average reflectance of higher than 96% was measured for the silver layer of the deposited mirror stack by calculating the absolute irradiance ratio of the reflected beam to the original beam launched from a 632.8 nm He-Ne laser using an integration sphere (Ocean Optics 2000+ Spectrometer, FOIS) (Figure 3.54).

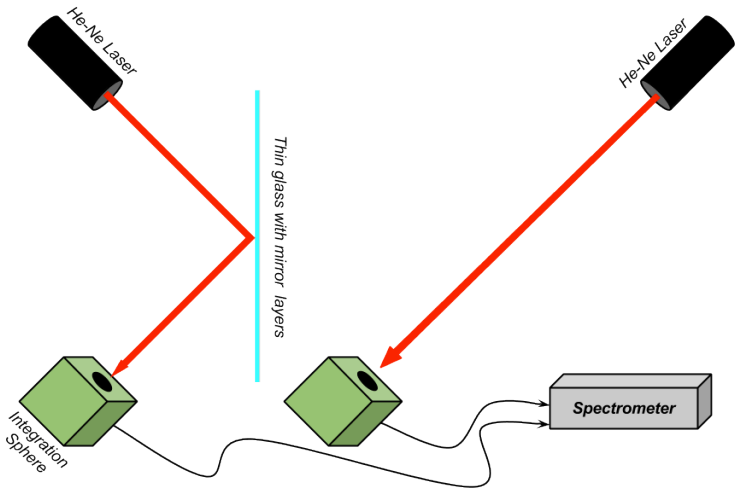

Figure 3.54 Reflection was calculated as the ratio of the absolute irradiance reflected from the mirror stack to the total irradiance of the He-Ne laser.

3.4.5 UBITag Summary

We were able to demonstrate the infrastructure of a universal identification system utilizing optical communication to assign a digital identity to physical objects with information accessible on the cloud. Utilizing miniature-size and low-power components available, a custom tag board was manufactured with dimensions of 9.7mm × 6.9 mm, scavenging optical power via an array of photovoltaic cells with a total area of 1.4 mm^2. The prototyped tag is functional at 2V of supply and a minimum photogenerated current of 400uA. For the Reader, a custom circuit was manufactured with packaged dimensions of 25mm × 45 mm × 85 mm, powered by 3 AAA batteries and fully controlled by an Android App via Bluetooth.

A miniature monolithic tag, the key solution to establish the UBITag system, can be fabricated through a sequence of CMOS and organic material deposition processes, which dramatically reduces the final cost. With a novel encapsulation process and attachment technique, the packaged UBITag can be attached to wide variety of objects. Regarding the infrastructure prototype, the data detection sensitivity and maximum functionality distance can be improved by reengineering of circuit boards. A potential major improvement in the

packaging would be to manufacture the mold plates through processes such as diamond turning instead of machine milling for optical quality surface finish. Additionally, the manual dropping of the chips into the cavity recesses can be better accomplished by processes such as self-assembly or vacuum driven gripper arrays.

Chapter 4 Conclusions and Future Plans

Contact Lens Embedded Display

The first segment of this dissertation presented the challenges to realizing a contact lens-embedded display and the progress being made to overcome them. We reviewed the process of making an active contact lens embedding a single-pixel LED and, in particular, demonstrated that process by embedding a display component, emitting predetermined text patterns, on the contact lens platform. Such single-pixel systems may be deployed for communicating immediate events to the user, but they are of limited use for conveying more extensive information.

One major challenge of constructing a display wearable in the form of a contact lens with multiple pixels is producing resolvable images from components that are placed directly on the cornea. To address this issue, micro-lenses can be integrated to aid the eye in focusing on a ghost image of the display falling in accommodation range. Refractive micro-lenses were found inapplicable for alteration of their focusing behavior after being embedded in tear film. Moreover, refractive lenses only allow limited control and variation of the focal range guided by the lenticular shape of the polymer resist layer. Thus, diffractive-based micro-lenses were proposed as a practical solution. To provide initial proof of the concept's viability and to simplify the fabrication process, amplitude-type diffractive patterns were chosen for experiment development. A detailed description of the design, simulation, and fabrication process of GaN-LEDs with integrated Fresnel Zone Plates was presented and the functionality of the system was successfully tested. Optical testing results of the fabricated system proved that FZPs may be placed in front of a single pixel or a group of pixels for imaging purposes. FZPs are perhaps some of the simplest diffractive patterns that can be integrated in a contact lens, but they demonstrate the promise of contact lenses for integration

of sophisticated diffractive optical elements for correcting and augmenting vision surpassing what might be feasible with conventional refractive optical elements. To achieve higher efficiency, phase-type patterns can be implemented through conventional 2-D fabrication techniques. To eliminate the chromatic aberration resulting from wavelength dependency of diffractive lens focusing behavior, MOD micro-lenses are feasible to fabricate through single-step processes such as Focused-Ion-Beam milling (FIB). In utilizing phase-modulating elements, special care to preserve the phase pattern becomes necessary, which is achievable by bonding a flat transparent protection layer to the side of the wafer with micro-lens structures.

Universal Basic Identification tag System (UBITag)

In the second segment of this project, we tried to come up with a method for integrating the physical objects into cyberspace by assigning a digital identity to them. The approach is to attach to every physical object a tag that can be mass-produced at a very low cost and can be communicated with wirelessly. The read-writable tag holds the unique ID assigned to the object, while a cloud-based service can manage the global assignment of the tag numbers and hold the database for all the codes and object definitions. For the tag to be seamlessly integrated with physical objects of various sizes, it must be extremely small. RFID tags cannot be made very small because the efficiency of the radio link drops dramatically when antenna size shrinks much smaller than the wavelength. Therefore we proceeded with an optical tag that can be made extremely small in principle and does not need a battery. For ease of reference, the name “Universal Basic Identification Tag (UBITag)” was chosen for the envisioned optical system. The so-called UBITag chip comprises a CMOS-integrated circuit, optical harvesting units and optical output units. A standard CMOS infrastructure can be used to fabricate photovoltaic input and integrated circuit units, while efficient CMOS-compatible optical outputs such as OLED pixels can feasibly be post-fabricated on a finished

CMOS structure. By combining the CMOS and OLED processes, the final cost of a mass-produced miniature tag can be reduced to semiconductor fraction of a finished RFID tag.

As first step toward making a UBITag, we tried to develop and fabricate CMOS-compatible OLEDs at an accessible facility; despite lacking access to proper equipment, we developed a single-layer polymer OLED structure. The effect of a potential barrier on turn-on voltage of the devices has been observed by depositing different anode materials; although the devices were not efficient for our application, the output optical spectrum of the organic polymer layer was measured with expected peak wavelength.

To demonstrate the envisioned identification system, we attempted to prototype the complete infrastructure using off-the-shelf components. Thus, custom hardware for the Reader and the autonomous tag were designed and manufactured, embedding microcontroller units, optical transducers, and analog electronics required for optical communication and power harvesting. The prototyped tag circuit harvests the necessary power from the Reader's optical beam by a series of silicon PIN diodes with a total active area of 1.4mm^2 and PCB size of 6mm*9mm. Like the tag, the custom Reader has infrared data detection and outputs to optically interact with tags while providing power via high-power red LEDs. The actions of the custom Reader are controlled through the designated Bluetooth peripheral. To complete the infrastructure prototyping, proper software for every level was developed. First a basic web database to store ID numbers and object definition was created; then a single-action Android application for interacting with the database and controlling the Reader's actions was developed. Next, proper firmware to establish asynchronous serial communication between the tag MCU, Reader MCU and the Android device was implemented. The developed prototype, by utilizing optics for power and data transmission, is capable of end-to-end demonstration of the envisioned identification system. Improving data detection sensitivity and the maximum functionality distance for the prototype is a matter of reengineering for future trials.

In the last section of the UBITag chapter, a novel, cost-effective packaging process for encapsulating miniature autonomous optical components was developed. A spherical transparent resin encapsulating the chip would enhance optical extraction of the structure, and the presence of a partial reflection coating on the resin drop would increase the chance of creating an optical path between the Reader's incident beam and the optical surface of the UBITag. Clear epoxide drops of 1.75mm in diameter, encapsulating mm-size silicon chips, were molded and cured using two-piece aluminum molds made through conventional machine milling. Then a bilayer of silver-aluminum as the main reflector and SiO2 as the protection layer was evaporated on the exposed surface of cured resin. These miniature spherical packages for the UBITag can be immersed in polymer matrices, simply printed on a variety of objects, and activated using the Reader's light beam conveying power and data (digital identity code). Initially, because we could not control a package's clear side orientation toward the Reader after attaching to an object, we required multiple packages to integrate in order to achieve a certain yield. To eliminate this requirement and to make the mirror and clear sides distinguishable, we developed a simple modification and attachment procedure, which tested at a 96% yield. One major future improvement for the packaging process will be to manufacture the mold plates through processes such as diamond turning instead of conventional machine milling to achieve optical quality surface finish. Vigorous optical investigation is required to correlate the UBITag's orientation in the resin drop with the Reader's optical beam, optimizing the size and shape of packaging. Additionally, to move toward a mechanized process, manual dropping of the chips into cavity recesses must be replaced by processes such as self-assembly.

With this successful demonstration of replacing RF with optics for an envisioned identification system, the monolithic optical tag can be mass-produced using existing CMOS infrastructure for fabricating compact storage/processing circuitry and photovoltaic cells to

scavenge optical power. As the main goal is to minimize the mass-production cost of UBITag chips, recent progress toward combining cost-effective OLED technology with CMOS makes such a process a suitable option for the optical output of the UBITag. In addition to identification, basic sensing features can also be implemented in the tag using certain circuit design techniques. For example, on-chip CMOS temperature sensors reported for RFID food monitoring with extremely low power consumption[127] can be duplicated in the UBITag as well. Ultimately, by utilizing the light source and detectors available on conventional mobile devices (such as camera and flashlight), the intermediate Reader circuit can be eliminated.

References

[1] R E Records, *Physiology of the human eye and visual system*. San Francisco: Harper and Row, 1979

[2] K N Leibovic, Ed., *Science of Vision*. New York: Springer-Verlag, 1990.

[3] A Phillips and L Speedwell, Eds., *Contact Lenses*, 5th ed. New York: Elsevier, 2007

[4] J Nichols, "Contact Lenses 2010 Annual Report," 2011

[5] B A Parviz, "For your eye only," *IEEE Spectrum*, no. September 2009, pp. 36-41, 2009

[6] I Lahdesmaki et al., "Possibilities for continuous glucose monitoring by a functional contact lens," *Instrumentation & Measurement Magazine, IEEE*, vol. 13, no. 3, pp. 14–17, 2010

[7] B Richter et al., "OLED-on-CMOS based bidirectional microdisplay for near-to-eye and sensor applications", Semiconductor Conference Dresden (SCD), 2011

[8] F L Pedrotti, L S Pedrotti, L M Pedrotti, *Introduction to Optics*, 3rd ed., p. 426, Pearson Prentice Hall, upper saddle river, NJ, 2007

[9] H. Ho et al., "Contact lens with integrated inorganic semiconductor devices," *IEEE 21st Int. Conf. on Micro Electro Mechanical Systems,* pp. 403-406, 2008

[10] J Pandey et al., “Toward an active contact lens: Integration of a wireless power harvesting IC,” *IEEE Conference in Biomedical Circuits and Systems*, pp. 125–128, 2009

[11] J Pandey et al., “A Fully Integrated RF-Powered Contact Lens With a Single Element Display”, *IEEE Transactions on Biomedical Circuits and Systems*, vol. 4, no. 6, pp. 454–461, 2010

[12] A R Lingley et al., “A single-pixel wireless contact lens display,” *Journal of Micromechanics and Microengineering*, vol. 21, no. 12, p. 125014, Dec. 2011

[13] R Mirjalili, B A Parviz, “Micro light emitting diode with integrated FZP for contact lens embedded display*”, J. Micro/Nanolith. MEMS MOEMS,* vol.11, no. 3, Jul–Sep 2012

[14] J De Smet et al., “Design and Wrinkling Behavior of a Contact Lens With an Integrated Liquid Crystal Light Modulator,” *Journal of Display Technology*, vol. 8, no. 5, pp. 299-305, May 2012.

[15] A Lingley “Design and Fabrication of Functional Contact Lenses with Integrated Light Emitting and Photovoltaic Components” PhD Dissertation, University of Washington 2012

[16] Khizar et al., “Nitride deep-ultraviolet light-emitting diodes with micro- lens array,” *Applied Physics Letters,* vol. 86, no. 17, 2005

[17] Choi et al., “Nitride micro-display with integrated micro-lenses,” *Solid State Physics*,

vol. 2 no. 7 , pp. 2903–2906 ,2005

[18] Choi et al., "GaN micro-light-emitting diode arrays with monolithically integrated sapphire microlenses," *Applied Physics Letters,* vol. 84, no. 13, pp. 2253–2255, 2004

[19] A Holmberg, "Nanofabrication of Zone Plate optics for compact soft x- ray microscopy," *Doctoral Thesis*, Royal Institute of Technology, 2006

[20] Menon et al., "Experimental characterization of focusing by high- numerical-aperture Zone Plates," *Journal of Optical Society of America A* vol.23, no. 3, pp.567–571, 2006

[21] Y Ee et al, "Enhancement of light extraction efficiency of InGaN quantum wells light emitting diodes using SiO2/polystyrene microlens arrays", *Applied Physics Letters,* vol.91, 2007

[22] X Li et al., "Light Extraction Efficiency and Radiation Patterns of III-Nitride Light-Emitting Diodes With Colloidal Microlens Arrays With Various Aspect Ratios", *IEEE Photonics Journal,* vol. 3, no. 3, June 2011

[23] Y Ee et al., "Optimization of Light Extraction Efficiency of III-Nitride LEDs With Self-Assembled Colloidal-Based Microlenses", *IEEE Journal of Selected Topics In Quantum Electronics*, vol. 15, no. 4, 2009

[24] Y Sun et al., "Organic light emitting devices with enhanced outcoupling via microlenses fabricated by imprint lithography", *Journal of Applied Physics* vol.100, 2006

[25] S Moller et al., “Improved light out-coupling in organic light emitting diodes employing ordered microlens arrays” *Journal of Applied Physics*, vol. 91, no. 5, March 2002

[26] H Peng et al., “Coupling Efficiency Enhancement in Organic Light-Emitting Devices Using Microlens Array—Theory and Experiment” *Journal of Display Technology*, vol. 1, no. 2, 2005

[27] A Davis et al., “Optical Design using Fresnel Lenses”, *Optik & Photonik*, no. 4, December 2007

[28] J A Davison et al, “History and development of the apodized diffractive intraocular lens”, *Journal of Cataract and Refractive Surgery*, vol.32, no.5, May 2006

[29] M Born, E Wolf, Principles of Optics; Electromagnetic Theory of Propagation, Interference, and Diffraction of Light, 5th ed. New York, NY, Pergamon Press, 1975

[30] E Hecht , A Zajac, “Optics”, Reading, MA, Addison-Wesley, 1974

[31] J L Soret, “Ueber die durch kreisgitter erzeugten Diffractionspha nomene”, *Ann. Phys. Chem.*, 1875

[32] A G Michette, “Optical Systems for Soft X Rays”, chapter 8, Plenum, New York, 1986.

[33] S J Spector, “Diffractive Optics for Soft X Rays”, *PhD thesis*, State University of New

York at Stony Brook, 1997

[34] A G Stein, "Focusing Optics for Soft and Hard X-rays: Fabrication, Replication and Simulations", *Doctoral Thesis*, State University of New York at Stony Brook, 2002.

[35] Anders Holmberg, "Nanofabrication of Zone Plate Optics for Compact Soft X-Ray Microscopy", *Doctoral Thesis*, Department of Applied Physics, Royal Institute of Technology, Stockholm, Sweden 2006

[36] M Lu, "Nanofabrication of Fresnel Zone Plates for soft X-ray imaging at carbon edge", *Doctoral Thesis*, Department of Physics, Stony Brook University, August 2006

[37] R W Wood, "Phase-reversal zone-plates, and diffraction-telescopes", *Phil. Mag.*, vol.45, pp.511–522, 1898

[38] D A Buralli DA et al., "Optical performance of holographic kinoforms", *Applied Optics*,vol. 28, pp.976–983, 1989

[39] T Sales et al., "Diffractive refractive behavior of kinoform lenses" *App Optics*, vol.36, no.1, pp. 253–257, 1997

[40] D Faklis et al., "Spectral properties of multiorder diffractive lenses", *Applied Optics,* vol. 34, no. 14,1995

[41] G J Swanson, ''Binary Optics Technology: The Theory and Design of Multi-level

Diffractive Optical Elements,'' M.I.T. Lincoln Laboratory Technical Report 854, NTIS Publ. AD-A213-404, 1989

[42] S Lane et al., "Multifocal Intraocular Lenses", *Ophthalmology Clinics of North America,* vol.19, pp.89 – 105, 2006

[43] D Falkis et al., "Polychromatic Diffractive Lens" US5589982, Dec 1996

[44] D A Buralli et al., ''Optical performance of holographic kinoforms", *Applied Optics* vol.28, no.5, pp.976–983, 1989

[45] J W Goodman, "Introduction to Fourier Optics", McGraw-Hill, NewYork, 1968 Chapter 5

[46] Jin Kang et al., "Inductively coupled plasma reactive ion etching of sapphire using C2F6- and NF3-based gas mixtures", *Materials Science in Semiconductor Processing* vol.11, pp.16– 19, 2008

[47] M E Motamedi et al., "Micro-optics integration with focal plane arrays", *Optical Eng.* vol. 36, No. 5, pp.1374-1382, May 1997

[48] K Yamada et al., "Multilevel phase-type diffractive lenses in silica glass induced by filamentation of femtosecond laser pulses", *Optics Letters,* vol. 29, no. 16, 2004

[49] H O Sankur et al., "Micro-optics Development in the Past Decade", *Proc. SPIE* 4179, pp.30-59, 2000

[50] D P Adams et al., “Accurate focused ion beam sculpting of silicon using a variable pixel dwell time approach”, *J. Vac. Sci. Technol. B* , vol.24, no.2, 2006

[51] M K Lee et al., “Gas-Assisted Etching of Sapphire Using Focused Ion Beam”, *Japanese Journal of Applied Physics,* vol. 45, no. 4A, pp. 2447–2450, 2006

[52] P M Nellen et al., “Milling micro-structures using focused ion beams and its application to photonic components”, *Meas. Sci. Technol*., vol.17, pp.943–948, 2006

[53] M K Lee et al., “Single-step fabrication of Fresnel microlens array on sapphire substrate of flip-chip gallium nitride light emitting diode by focused ion beam”, *Applied Physics Letters,* vol.91, 2007

[54] R J M Vullers et al., “Micropower energy harvesting,” *Solid State Electronics*, pp.684-693, April 2009

[55] W L Stutzman, G A Thiele, Antenna Theory and Design, New York: John Wiley & Sons, Inc., 1981

[56] K Fujimoto *et al.*, Small Antennas , New York: Wiley, 1987

[57] G S Smith, “Efficiency of electrically small antennas combined with matching networks,” *IEEE Transaction on Antennas and Propagation*, vol. AP-25, pp. 369–373, May 1977

[58] H A Wheeler, "Fundamental Limitations of Small Antennas," *Proceedings of the IRE*, vol. 35, pp. 1479-1484, 1947

[59] H A Wheeler, "The Radiansphere around a Small Antenna," *Proceedings of the IRE*, vol. 47, pp. 1325-1331, 1959

[60] W A Davis et al., "Fundamental limits on antenna size: a new limit", *Microwaves, Antennas & Propagation, IET,* vol.5, no. 11, Aug 2011

[61] J S McLean, "A Re-Examination of the Fundamental Limits on the Radiation Q of Electrically Small Antennas", *IEEE Transactions on Antennas and Propagation*, vol. 44, no.5, May 1996

[62] S O'Driscoll et al, "A mm sized implantable power receiver with adaptive link compensation", ISSCC 2009

[63] W Biederman et. al, "A Fully-Integrated, Miniaturized (0.125 mm²) 10.5 μW Wireless NeuralSensor", JSSC, vol.48, no.4, April 2013

[64] B Warneke et al, "Smart Dust : Communicating with a Cubic- Millimeter Computer," *Computer Magazine*, pp. 44-51, 2001

[65] B A Warneke et al., "An autonomous 16 mm3 solar-powered node for distributed wireless sensor networks," *Proceedings of IEEE Sensors*, vol. 2, pp. 1510-1515, 2002

[66] S S Clark et al., “Towards Autonomously- Powered CRFIDs,” *Power*, October, 2009.

[67] A P Sample et al., “Photovoltaic Enhanced UHF RFID Tag Antennas for Dual Purpose Energy Harvesting”, *IEEE International Conference on RFID*, pp. 146-153, 2011

[68] R Vyas et al., “Design and Characterization of a Novel Battery-less , Solar Powered Wireless Tag for Enhanced-Range Remote Tracking Applications,” *Solar Cells*, no. October, pp. 169-172, 2009

[69] M Ferri et al., “Integrated micro-solar cell structures for harvesting supplied microsystems in 0.35-µm CMOS technology, *The 8th IEEE conference on Sensors*, pp.542-545, 2009

[70] O Bulteel et al., “High-Efficiency Solar Cell Embedded in SOI Substrate for ULP Autonomous Circuits”, *IEEE International SOI Conference*, pp.1-2, 2009

[71] S Ayazian et al. “A Photovoltaic-Driven and Energy-Autonomous CMOS Implantable Sensor” *, IEEE Transactions on Biomedical Circuits and Systems*, vol. 6, no. 4, August 2012

[72] M Ferri et al., “Integrated stabilized photovoltaic energy harvester”,*16th IEEE International Conference on Electronics, Circuits, and Systems*, 2009

[73] W Andre, S Martel, “Micro-photovoltaic cells designed for magnetotaxis-based controlled bacterial microrobots” *IEICE Electronics Express*, vol.5, no.3, pp.101-105, 2008

[74] C L Bellew et al., “An SOI Process for Fabrication of Solar Cells, Transistors and Electrostatic Actuators”, *The 12th International Conference on Solid State Sensors, Actuators and Microsystems,* Boston, June 8-12, 2003

[75] S Bermejo et al., “c-Si photovoltaic arrays*”, IEEE LEOS Annual Meeting Conference Proceedings*, 2009

[76] Y Choi et al., “Integrate Front Contact Solar Cells Fabricated By CMOS Process Technologies”,*37th IEEE Photovoltaic Specialists Conference (PVSC),* 2011

[77] J Lu et al., “Integration of Solar Cells on Top of CMOS Chips Part I: a-Si Solar Cells”, *IEEE Transactions on Electron Devices*, vol. 58, no. 7, July 2011

[78] J Lu et al., “Integration of Solar Cells on Top of CMOS Chips—Part II: CIGS Solar Cells”, *IEEE Transactions on Electron Devices*, vol. 58, no. 8, August 2011

[79] J Lu et al., “Above-CMOS a-Si and CIGS Solar Cells for Powering Autonomous Microsystems”, *IEEE International Electron Devices Meeting (IEDM),*2010

[80] J Lu, “Solar Cells on CMOS Chips As Energy Harvesters- Integration and CMOS Compatibility” *Doctoral Thesis*, University of Twente,2011, ISBN: 978-90-365-3211-2

[81] I Doms et al., “Integrated Capacitive Power-Management Circuit for Thermal Harvesters with Output Power 10 to 1000μW,” *IEEE ISSCC,* 2009

[82] I K Kokubum, *Encyclopedic Handbook of Integrated Optics* (New York: CRC Press), p259, 2005

[83] R Hunsperger, *Integrated Optics Theory and Technology* (New York: Springer) 2002

[84] D Cristea et al., "Silicon optoelectronic integrated circuits for MOEMS" *Symp. Design, Test, Integration, and Packaging of MEMS/MOEMS, Proc. SPIE,* vol.30, 516–25, 2000

[85] M Pera´lvarez et al*., Applied Physics Letters,* vol.89, 2006

[86] C H Mastrangelo et al., "Electrical and Optical Characteristics of Vacuum- Sealed Polysilicon Microlamps*" IEEE Transactions on Electron Devices*, vol. 39, no. 6, June 1992

[87] M A Fisher, "Flat panel display with array of micromachined incandescent lamps", *Patent* 5956003, 1999

[88] J Tu et al., "Micromachined silicon filament light source for spectrophotometric Microsystems", *Applied Optics*, vol. 42, no. 13, May 2003

[89] F Hochberg et al., "A Thin-Film Integrated Incandescent Display", *IEEE Transaction of Electron Devices*, vol. 20, no.11, 1973

[90] K R Williams et al., "Ic-processedhot-filament vacuum microdevices", *IEEE International Electron Devices Meeting Technical Digest,* pp 387–90, 1992

[91] Y Ma et al., ”CMOS micromachined low power microlamp vacuum sensor”, *Canadian Conf. on Electrical and Computer Engineering* vol. 2, pp 971–5, 2000

[92] C H Mastrangelo et al., “Microfabricated incandescent lamps”, *Applied Optics*, vol. 30, no. 7, March 1991

[93] C H Mastrangelo et al., “Vacuum-Sealed Silicon Micromachined Incandescent Light Source” *International Electron Devices Meeting*, 1989

[94] R Muller et al., “Vacuum-sealedsilicon incandescent light” *Patent* 5285131, 1994

[95] M I Alayo et al., “MEMS-based incandescent microlamps for integrated optics applications”, *Journal of Optics A: Pure and Applied Optics,* vol.10, 2008

[96] A H Gollub et al, “Development of micro-incandescence light sources on silicon substrate”, *Proc. of SPIE* Vol. 7590, 2010

[97] G Rehder et al, “Integration of optical waveguides with micro-incandescent light”, *Journal of Non-Crystalline Solids,* vol.354, pp.2538–2543, 2008

[98] S Reineke et al., “White organic light-emitting diodes with fluorescent tube efficiency”, *NATURE*, vol. 459, pp.234-238, 2009

[99] D Kreye et al., “Full colour RGB OLEDs on CMOS for Active-Matrix OLED

Microdisplays", *Proc. Of SPIE*, Vol. 6333, 2006

[100] R Herold et al., "OLED-on-CMOS Integration for Augmented-Reality Systems" *Photonics and Microsystems International Students and Young Scientists Workshop*, 2008

[101] M Toerker et al., "Integration of Top-Emitting Organic Light Emitting Diodes on CMOS Substrates", *Proc. Of SPIE*, vol. 6999, 2008

[102] M Scholles et al., "LabOnFoil: Laboratory skin patches and SmartCards based on OLED-on-CMOS and MEMS components", *Proc. Of SPIE*, vol. 7207, 2009

[103] B Richter et al., "Bidirectional OLED Microdisplay: Combining Display and Image Sensor Functionality into a Monolithic CMOS Chip", *ISSCC* 2011

[104] A P Ghosh, "Full Color OLED on Silicon Microdisplay", *Proc. Of SPIE*, vol.4464, 2002

[105] G Kelly et al., "A Full Color QVGA Microdisplay using Light Emitting Polymer on CMOS", *13th IEEE International Conference on Electronics, Circuits and Systems*, 2006

[106] I Underwood et al., "P-OLED Microdisplays", *19th Annual Meeting of the IEEE Lasers and Electro-Optics Society*, 2006

[107] I Underwood et al., "Polymer OLED Microdisplay Technology - Pixel Design in Context", *Proc. Of SPIE*, Vol. 6333, 2006

[108] A P Ghosh et al., “Recent advances in small molecule OLED-on-silicon microdisplays”, *Proc. Of SPIE*, Vol. 7415, 2009

[109] E Gurnee, R Fernandez, *US Patent* 3172862, 1965

[110] M Pope et al., *J. Chem. Phys*., vol.38, 1963

[111] C W Tang, *US Patent* 4356429, 1982

[112] C W Tang et al., *Applied Physics Letters,* vol.51, 1987

[113] R Friend, J Burroughes, D Bradley, *WO Patent* 90/13148, 1990

[114] R Friend, J Burroughes, D Bradley, *US Patent* 5247190, 1993

[115] S R Forrest, “The road to high efficiency organic light emitting devices”, *Organic Electronics,* vol. 4, pp.45–48, 2003

[116] J M Legar, “ Electrochemical Doping and the Optical Properties of Light Emitting Polymer Materials and Devices”, *Doctoral Thesis*, University of California Santa Cruz, 2005

[117] M A Baldo et al., “Organic Vapor Phase Deposition”, *Advanced Materials*, vol.10, no.18, 1998

[118] LS Hung et al., “Recent progress of molecular organic electroluminescent materials and devices”, *Materials Science and Engineering,* vol.39, pp.143–222, 2002

[119] D K Chambers et al, “The electronic structure of oriented poly [2-methoxy-5-(2’-ethyl-hexyloxy)-1,4-phenylene- vinylene]”, *Applied Physics A,* vol.80, pp. 483–488, 2005

[120] I D Parker et al, “Carrier tunneling and device characteristics in polymer light emitting diodes”, *Journal of Applied Physics,* vol.75, no.3, 1994

[121] V S Reddy et al., “Characteristics of MEH-PPV thin films on ITO electrode for organic light emitting diodes”, *Proc. of ASID*, 2006

[122] J C Scott et al., “Hole limited recombination in polymer light-emitting diodes”, *Applied Physics Letters*, vol.74, no.11, 1999

[123] J C Scott et al., “Degradation and failure of MEHPPV light emitting diodes”, *Journal of Applied Physics,* vol.79, no. 5, 1996

[124] D Braun et al., “Visible light emission from semiconducting polymer diodes”, *Applied Physics Letters,* vol.58, no. 18, 1991

[125] J Ouyang et al., “High-Performance, Flexible Polymer Light- Emitting Diodes Fabricated by a Continuous Polymer Coating Process”, *Advanced Materials* vol.14, no.12, 2002

[126] I H Campbell et al., *Phys. Rev. Lett.* vol.76, 1996

[127] M K Law et al., "A Sub-uW Embedded CMOS Temperature Sensor for RFID Food Monitoring Application," *IEEE Journal of Solid-State Circuits*, vol. 45, no. 6, pp. 1246-1255, 2010

Appendix A Tag and Reader MCU codes

```
//****Tag MCU code
#include "msp430fr5739.h"

unsigned char *p ;
unsigned char *q ;
unsigned char *r ;
unsigned char j=0;
unsigned char k=0;
unsigned char i=0;
unsigned char t=0;
void main(void)

{
          WDTCTL = WDTPW + WDTHOLD;               // stop watchdog
            CSCTL0_H = 0xA5;
            CSCTL1 &= ~DCORSEL ;            // Set min. DCO setting
              CSCTL1 &= ~DCOFSEL1;
              CSCTL1&= ~DCOFSEL0;
              CSCTL2 = SELA_3;     // set ACLK = XT1; MCLK = DCO
            CSCTL3 = DIVA_5 ;      // set all dividers to 32
            CSCTL4 |= XT1DRIVE_0;
            CSCTL4 |= XT1OFF+XT2OFF;
///  Unused pins should be set DIR =1 to minimize the current draw

           PJDIR |= BIT0 + BIT1 + BIT2 + BIT3 + BIT4 + BIT5 ;
           P1DIR |= BIT0 + BIT1 + BIT2 + BIT3 + BIT4 + BIT5 + BIT6 + BIT7;
           P2DIR |= BIT2 + BIT3 + BIT4 + BIT5 + BIT6 + BIT7;

            // Configure UART pins
            P2SEL1 |= BIT0 + BIT1;
            P2SEL0 &= ~(BIT0 + BIT1);

            // Configure UART 0

            UCA0CTL1 |= UCSWRST;
            UCA0CTLW0 = UCMODE_2;
            UCA0CTL1 = UCSSEL_1;
            UCA0BR0 = 1;                        // 9600 baud
            UCA0MCTLW |= 0x6B11;
                                    // UCBRSx value = 0x53
 UCA0CTL1 &= ~UCSWRST;                  // release from reset
 UCA0CTL1 |=UCDORM ;   //UCDORM =1
 UCA0IE |= UCRXIE;                      // Enable RX interrupt
 k=0;

  __bis_SR_register(LPM3_bits + GIE);      // LPM3 + Enable interrupt

}

#pragma vector=USCI_A0_VECTOR

__interrupt void USCI_A0_ISR(void)

{
```

```
switch (k){
case 0:
        j=0;
        p = (unsigned char *)0xCB02;
        k=UCA0RXBUF;
        UCA0CTL1 &= ~UCDORM ;   //UCDORM =0
        UCA0IFG &=~ UCRXIFG;                    // Clear interrupt
        UCA0IE |= UCRXIE;                       // Enable RX interrupt
break;
case 10:
        if (j<8) {
                *p++=UCA0RXBUF;
                j++;
                UCA0IFG &=~ UCRXIFG;                    // Clear interrupt
                UCA0IE |= UCRXIE;                       // Enable RX Int

                        }

        else {
                UCA0CTL1 |= UCTXADDR;
                UCA0TXBUF = 10;
                k = 0;
                j = 0;
                UCA0CTL1 |= UCDORM ;
                UCA0IFG &=~ UCRXIFG;                    // Clear interrupt
                UCA0IE |= UCRXIE;                       // Enable RX Int

                                                }
break;
case 4:
        for(t = 0; t <= 46; t++);
        r = (unsigned char *)0xCB02;
                UCA0CTL1 |= UCTXADDR; // Send ReadCMD followed by ID array.
                UCA0TXBUF = 4;
                for (i=0; i<8 ; i++) {
for(t = 0; t <= 3; t++);
                if ((UCA0IFG&UCTXIFG)){
                UCA0TXBUF = *r++;
                        }
                }
                k = 0;
                UCA0CTL1 |= UCDORM ;
                UCA0IFG &=~ UCRXIFG;                    // Clear interrupt
                UCA0IE |= UCRXIE;                       // Enable RX interrupt
        break;
default:
k=0;
        break;

}
}
```

//*** Reader MCU Code

```
#include "msp430fr5739.h"

long long ID = 1024;
char byteArray[8];
unsigned int counter;
unsigned int i;
unsigned int j;
unsigned int k;
unsigned int g;
unsigned int t;
unsigned int TagWRTflag;
unsigned int flag;
unsigned int cmd;
unsigned char WRTcmd = 10;
unsigned char Callcmd = 2;
unsigned char RDcmd = 4;
unsigned char Rxdata ;
unsigned char check = 0;
unsigned char *FRAM_write_ptr;
unsigned char *CMD;
unsigned char *p;
unsigned char *r;
unsigned char *n;
unsigned char *newID;
unsigned char *readID;
unsigned char *s;

void main(void)
{
   WDTCTL = WDTPW + WDTHOLD;    //\ stop watchdog
   CSCTL0_H = 0xA5;
            CSCTL1 |= DCORSEL ;            // Set min. DCO setting
              CSCTL1 |=DCOFSEL 1;
              CSCTL1|= DCOFSEL0;
              CSCTL2 = SELA_3 + SELS_3 + SELM_3;  // set ACLK = XT1; MCLK = DCO

            CSCTL4 |= XT1DRIVE_0;
            CSCTL4 &= ~XT1OFF;
P1DIR &= ~BIT3;
P1DIR &= ~BIT4;
P1REN |= BIT3+BIT4 ;
P1OUT &= ~BIT3;
P1OUT &= ~BIT4;

            // Configure UART A0 pins : connects to Tag
  P2SEL1 |= BIT0 + BIT1;
  P2SEL0 &= ~(BIT0 + BIT1);
  // Configure UART A1 pins : connects to App
    P2SEL1 |= BIT5 + BIT6;
    P2SEL0 &= ~(BIT5 + BIT6);
  // Configure UART 0,mode2 :Address bit,Dormant on
    UCA0CTLW0 |= UCSWRST;
    UCA0CTLW0 = UCMODE_2;
    UCA0CTL1 = UCSSEL_1;                // Set ACLK = 32768 as UCBRCLK
    UCA0BR0 = 156;                          // 9600 baud
  UCA0MCTLW |= 0x0041;           // 32768/9600 - INT(32768/9600)=0.41
```

```
                        // UCBRSx value = 0x53 (See UG)
  UCA0BR1 = 0;
  UCA0CTL1 &= ~UCSWRST;                   // release from reset
  UCA0CTL1 |=UCDORM ;   //UCDORM =1
  UCA0IE |= UCRXIE;                       // Enable RX interrupt
  // Configure UART 1, Mode_0 uart
  UCA1CTL1 |= UCSWRST;
  UCA1CTL1 = UCSSEL_1;                    // Set ACLK = 32768 as UCBRCLK
  UCA1BR0 = 156;                          // 9600 baud
  UCA1MCTLW |= 0x0041;          // 32768/9600 - INT(32768/9600)=0.41
                              // UCBRSx value = 0x53 (See UG)
  UCA1BR1 = 0;
  UCA1CTL1 &= ~UCSWRST;                   // release from reset
  UCA1IE |= UCRXIE;                       // enable RX interrupt
cmd=0;
g=0;
__enable_interrupt();

while (1){
        n = (unsigned char *)0xCA02;
        if ( P1IN & BIT3 ){
                for(k = 0; k <= 50000; k++);
                        if ((UCA0IFG&UCTXIFG)){
                        UCA0CTL1 |= UCTXADDR;
                                UCA0TXBUF = RDcmd;
                                                                        }
                        for(k = 0; k <= 50000; k++);
                }
        if ( P1IN & BIT4 ){
                for(k = 0; k <= 50000; k++);
                UCA0CTL1 |= UCTXADDR;         // Send ReadCMD followed by ID array.
                        UCA0TXBUF = WRTcmd;
                                for (i=0; i<8 ; i++) {
                                        for(k = 0; k <= 3000; k++);
                                        if ((UCA0IFG&UCTXIFG)){
                                        UCA0TXBUF = *n++;
                                                }
                                        }
                        for(k = 0; k <= 50000; k++);
                }
        }
        }
#pragma vector=USCI_A0_VECTOR
__interrupt void USCI_A0_ISR(void)
{
switch (cmd){
case 0:
        j=0;
        r= (unsigned char *)0xCC02;
        cmd=UCA0RXBUF;
        UCA0CTL1 &= ~UCDORM ;   //UCDORM =0
        UCA0IFG &=~ UCRXIFG;                    // Clear interrupt
        UCA0IE |= UCRXIE;                       // Enable RX interrupt
break;
case 4:
        if (j<8) {
                *r++=UCA0RXBUF;
                j++;
                UCA0IFG &=~ UCRXIFG;                    // Clear interrupt
                UCA0IE |= UCRXIE;                   // Enable RX interrupt
```

```
                        }

        else {
                cmd = 0;
                j = 0;
                UCA0CTL1 |= UCDORM ;
                UCA0IFG &=~ UCRXIFG;                    // Clear interrupt
                UCA0IE |= UCRXIE;                   // Enable RX interrupt                          }
break;

case 10:
        cmd = 0;
                UCA0CTL1 |= UCDORM ;
                UCA0IFG &=~ UCRXIFG;                    // Clear interrupt
                UCA0IE |= UCRXIE;                // Enable RX interrupt
        break;

default:
        cmd=0;
break;
}
}

#pragma vector=USCI_A1_VECTOR

__interrupt void USCI_A1_ISR(void)

{
switch (g){
case 0:
        t=0;
        newID = (unsigned char *)0xCA02;
        s = (unsigned char *)0xCC02;
        g=UCA1RXBUF;
if (g==4){
        for (counter=0; counter<8 ; counter++) {
                for(k = 0; k <= 300; k++);
                if ((UCA1IFG&UCTXIFG)){
                        UCA1TXBUF = *s++;
                        }
                        }
                        g = 0;
}
        UCA1IFG &=~ UCRXIFG;                    // Clear interrupt
        UCA1IE |= UCRXIE;                   // Enable RX interrupt
break;
case 10:
        if (t<8) {
                UCA1TXBUF=UCA1RXBUF;
                *newID++=UCA1RXBUF;
                t++;
                UCA1IFG &=~ UCRXIFG;                    // Clear interrupt
                UCA1IE |= UCRXIE;                // Enable RX interrupt
                        }
        else {
                g = 0;
                t = 0;
                UCA1IFG &=~ UCRXIFG;                    // Clear interrupt
                UCA1IE |= UCRXIE;                   // Enable RX interrupt
                        }
```

```
break;

}
}
```

Appendix B Database inquiry PHP syntax

```
/* write.php*/
<html>
<body>
<?php

$TagID = $_GET["TagID"];

if (!empty($TagID)) {
if (!is_int($TagID)) {
$db = new PDO("mysql:dbname=UBITagDatabase", "root", "");
 $db->setAttribute(PDO::ATTR_ERRMODE, PDO::ERRMODE_EXCEPTION);
$sql = "SELECT * FROM ubitaginformation WHERE TagID = $TagID";
$res = $db->query($sql);


   /* Check the number of rows that match the SELECT statement */
 if ($res->fetchColumn() > 0) {
print "The ID has already taken, please enter a different one!";
  }


   /* No rows matched -- do something else */
 else { ?>

<form action ='newtag.php' method='post'>
<p>TagID:</br><input type="text" size="25" name="id" value= "<?=$TagID?>" readonly="readonly"></p>
<p>TagInfo:</br><textarea name="info" rows="10' cols="25">
Please insert the tag information.
</textarea></p>
 <input type='submit' name='submit' value='Submit to database'>
</form>
<?}
}
else {
print "please enter a valid integer ID";
}
}


else {
print "please enter something!";
}
?>
</body>
</html>
/* read.php*/
<html>
<body>
<?php


 $db = new PDO("mysql:dbname=UBITagDatabase", "root", "");
 $db->setAttribute(PDO::ATTR_ERRMODE, PDO::ERRMODE_EXCEPTION);
$TagID = (int) $_GET["TagID"];
$sql = "SELECT COUNT(*) FROM ubitaginformation WHERE TagID = $TagID";
if ($res = $db->query($sql)) {
```

```
  /* Check the number of rows that match the SELECT statement */
 if ($res->fetchColumn() > 0) {


      /* Issue the real SELECT statement and work with the results */
       $sql = "SELECT * FROM ubitaginformation WHERE TagID = $TagID";
     foreach ($db->query($sql) as $row) { ?>
      <p> TagID: </br> <?= $row['TagID'] ?>  </p>
            <p> TagInfo:</br> <?= $row['TagInformation']?>  </p>
       <?}
  }


  /* No rows matched -- do something else */
 else {
    print "No match for this ID, $TagID, found in database.";


}
}
?>
</body>
</html>


/*newtag.phph*/
<html>
<body>
<?php
try {
 $db = new PDO("mysql:dbname=UBITagDatabase", "root", "");
 $db->setAttribute(PDO::ATTR_ERRMODE, PDO::ERRMODE_EXCEPTION);


$ID=$_POST['id'];
$Info=$_POST['info'];
$sql = "SELECT COUNT(*) FROM ubitaginformation WHERE TagID = $ID";
$res = $db->query($sql);
 /* Check the number of rows that match the SELECT statement */
 if ($res->fetchColumn() > 0) { ?>
<p>Sorry, This ID is already taken. Please try again.</p>
<?}

else{
$sql = "INSERT INTO ubitaginformation (TagID,TagInformation) VALUES('$ID','$Info')";
$res=$db->exec($sql); ?>
<p>Done, New ID/Information added to database.</p>
<?
}
}catch (PDOException $ex) { ?>

 <p>Sorry, a database error occurred. Please try again later.</p>
 <p>(Error details: <?= $ex->getMessage() ?>)</p>
<?php
}
?>
</body>
</html>
```

Appendix C MSP430FR57xx blocks

MSP430FR5739: Utilized in prototyped Reader circuit

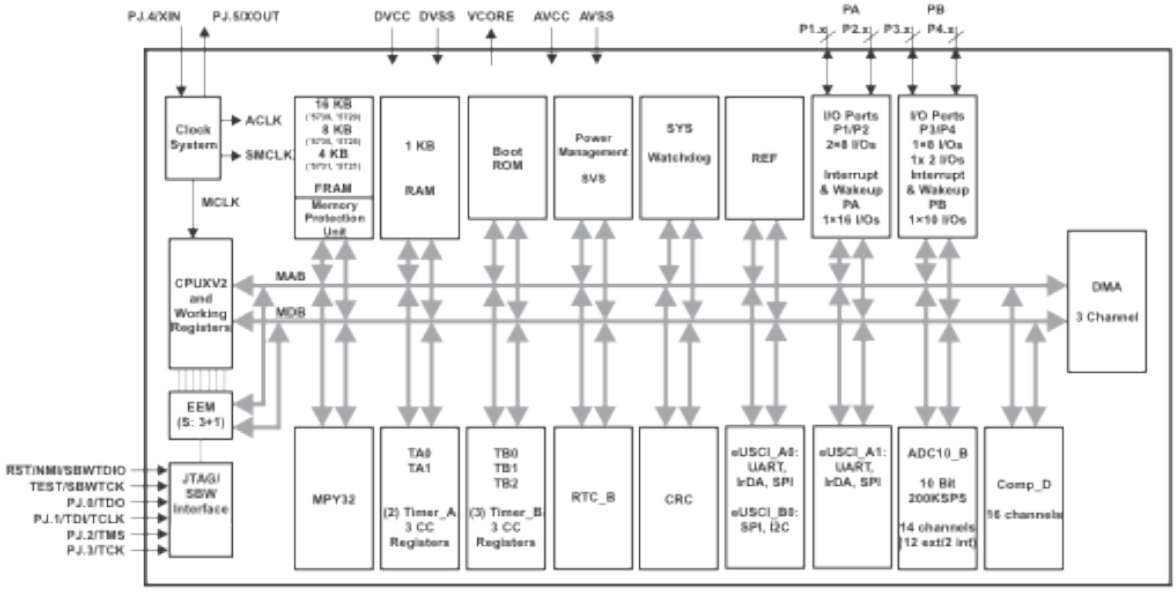

MSP430FR5738: Utilized in prototyped Tag circuit